



1 **Tropospheric aerosols over the western North Atlantic Ocean**
2 **during the winter and summer campaigns of ACTIVATE 2020:**
3 **Life cycle, transport, and distribution**
4

5 Hongyu Liu^{1,2}, Bo Zhang^{1,2}, Richard H. Moore², Luke D. Ziemba², Richard A. Ferrare², Hyundeok
6 Choi^{1,*}, Armin Sorooshian³, David Painemal^{2,4}, Hailong Wang⁵, Michael A. Shook², Amy Jo
7 Scarino^{2,4}, Johnathan W. Hair², Ewan C. Crosbie^{2,4}, Marta A. Fenn^{2,4}, Taylor J. Shingler², Chris
8 A. Hostetler², Gao Chen², Mary M. Kleb², Gan Luo⁶, Fangqun Yu⁶, Jason L. Tackett², Mark A.
9 Vaughan², Yongxiang Hu², Glenn S. Diskin², John B. Nowak², Joshua P. DiGangi², Yonghoon
10 Choi^{2,4}, Christoph A. Keller^{7,8}, and Matthew S. Johnson⁹

11 ¹National Institute of Aerospace, Hampton, VA, USA

12 ²NASA Langley Research Center, Hampton, VA, USA

13 ³University of Arizona, Tucson, AZ, USA

14 ⁴Analytical Mechanics Associates, Hampton, VA, USA

15 ⁵Pacific Northwest National Laboratory, Richland, WA, USA

16 ⁶State University of New York at Albany, Albany, NY, USA

17 ⁷Morgan State University, Baltimore, MD, USA

18 ⁸NASA Goddard Space Flight Center, Greenbelt, MD, USA

19 ⁹NASA Ames Research Center, Moffett Field, CA, USA

20 ^{*}Now at SAIC / NOAA/NWS/NCEP/Environmental Modeling Center, College Park, MD, USA

21

22

23

24

25

Correspondence to: Hongyu Liu (hongyu.liu-1@nasa.gov); Bo Zhang (bo.zhang@nasa.gov)

26 **Abstract.** The Aerosol Cloud meTeorology Interactions oVer the western ATlantic Experiment (ACTIVATE) is a
27 six-year (2019-2024) NASA Earth-Venture Suborbital-3 (EVS-3) mission to robustly characterize aerosol-cloud-
28 meteorology interactions over the western North Atlantic Ocean (WNAO) during winter and summer seasons, with a
29 focus on marine boundary layer clouds. This characterization requires understanding the aerosol life cycle (sources
30 and sinks), composition, transport pathways, and distribution in the WNAO region. We use the GEOS-Chem chemical
31 transport model driven by the MERRA-2 reanalysis to simulate tropospheric aerosols that are evaluated against in situ
32 and remote sensing measurements from Falcon and King Air aircraft, respectively, as well as ground-based and
33 satellite observations over the WNAO during the winter (Feb. 14 – Mar. 12) and summer (Aug. 13 – Sep. 30) field
34 deployments of ACTIVATE 2020. Transport of pollution in the boundary layer behind cold fronts is a major
35 mechanism for the North American continental outflow to the WNAO during Feb.-Mar. 2020. While large-scale
36 frontal lifting is a dominant mechanism in winter, convective lifting significantly increases the vertical extent of major
37 continental outflow aerosols in summer. Turbulent mixing is found to be the dominant process responsible for the
38 vertical transport of sea salt within and ventilation out of the boundary layer in winter. The simulated boundary layer
39 aerosol composition and optical depth (AOD) in the ACTIVATE flight domain are dominated by sea salt, followed
40 by organic aerosol and sulfate. Compared to winter, boundary layer sea salt concentrations increased in summer over
41 the WNAO, especially from the ACTIVATE flight areas to Bermuda, because of enhanced surface winds and
42 emissions. Dust concentrations also significantly increased in summer because of long-range transport from North



43 Africa. Comparisons of model and aircraft submicron non-refractory aerosol species (measured by an HR-ToF-AMS)
44 vertical profiles show that intensive measurements of sulfate, nitrate, ammonium, and organic aerosols in the lower
45 troposphere over the WNAO in winter provide useful constraints on model aerosol wet removal by precipitation
46 scavenging. Comparisons of model aerosol extinction (at 550 nm) with the King Air High Spectral Resolution Lidar-
47 2 (HSRL-2) measurements (at 532 nm) and CALIOP/CALIPSO satellite retrievals (at 532 nm) indicate that the model
48 generally captures the continental outflow of aerosols, the land-ocean aerosol extinction gradient, and the mixing of
49 anthropogenic aerosols with sea salt. Large enhancements of aerosol extinction at ~1.5-6.0 km altitudes from long-
50 range transport of the western U.S. fire smoke were observed by HSRL-2 and CALIOP during Aug.-Sep. 2020. Model
51 simulations with biomass burning (BB) emissions injected up to the mid-troposphere (vs. within the BL) better
52 reproduce these remote-sensing observations, Falcon aircraft organic aerosol vertical profiles, as well as AERONET
53 AOD measurements over eastern U.S. coast and Tudor Hill, Bermuda. High aerosol (mostly coarse-mode sea salt)
54 extinction near the top (~1.5-2.0 km) of the marine BL along with high relative humidity and cloud extinction were
55 typically seen over the WNAO (< 35°N) in the CALIOP aerosol extinction profiles and GEOS-Chem simulations,
56 suggesting strong hygroscopic growth of sea salt particles and sea salt seeding of marine boundary layer clouds.
57 Contributions of different emission types (anthropogenic, BB, biogenic, marine, and dust) to the total AOD over the
58 WNAO in the model are also quantified. Future modeling efforts should focus on improving parameterizations for
59 aerosol wet scavenging and sea salt emissions, implementing realistic BB emission injection height, and applying
60 high-resolution models that better resolve vertical transport.

61

62 1. Introduction

63 Aerosol particles scatter or absorb radiation in the atmosphere, directly affecting radiation budget and balance
64 and thus climate. Aerosols act as cloud condensation nuclei (CCN) or ice nuclei (IN), indirectly affecting radiation
65 via the formation of clouds and precipitation. They also affect tropospheric photolysis and photochemistry by
66 modifying solar radiation, and heterogeneous chemistry by providing surfaces for gas-particle interaction. While the
67 interaction of aerosols with clouds remains the largest uncertainty in the estimates of the Earth's changing energy
68 budget, a full understanding requires knowledge of aerosol transport, sources, sinks, composition, and distribution,
69 which still have large gaps (Boucher et al., 2013). Continental outflow regions represent a mixture of various aerosol
70 sources and types, and are impacted by large-scale and synoptic weather systems (Sorooshian et al., 2020), offering a
71 place for testing the current understanding of tropospheric aerosol processes. Among these regions, the western North
72 Atlantic Ocean (WNAO) presents “a complex atmospheric system with many unknowns” (Sorooshian et al. 2020;
73 Painemal et al. 2021). ACTIVATE is a six-year (2019-2024) NASA Earth Venture Suborbital-3 (EVS-3) mission to
74 investigate aerosol-cloud-meteorology interactions over the WNAO during winter and summer seasons, with a focus
75 on the marine boundary layer (MBL) clouds (Sorooshian et al., 2019; 2023). In this paper, we characterize the aerosol
76 life cycle, transport, composition, and distribution over the WNAO, defined as the oceanic domain bounded by 25–
77 50°N and 60–85°W, and North America's East Coast, during the winter (Feb.-Mar.) and summer (Aug.-Sep.)
78 campaigns of ACTIVATE 2020 using the GEOS-Chem chemical transport model.



79 Climatological circulation patterns largely determine the transport pathways and spatial distribution of trace
80 gases and aerosols over the WNAO (Sorooshian et al. 2020; Corral et al. 2021). The atmospheric circulation over the
81 North Atlantic Ocean basin is characterized by two semipermanent features: the Bermuda or Azores High (subtropical
82 anticyclone) and the Icelandic Low (subpolar low pressure) (Davis et al., 1997; Tucker and Barry, 1984). In summer,
83 the Bermuda High reaches its maximum spatial extent over the WNAO and extends westward, with southwesterly
84 winds over the western part of the domain north of 30°N and easterly trade winds in the subtropics (Painemal et al.,
85 2021). In winter, its expansion is limited by the development of the Icelandic Low north of 45°N. While the prevalent
86 westerly winds in winter/spring favor transport of pollution from North America to the Atlantic Ocean and toward
87 Europe, the trade winds south of the Bermuda High in summer facilitate transport of aerosols from the eastern Atlantic
88 and North Africa to the WNAO (e.g., Chen & Duce, 1983). The large-scale alternation of atmospheric mass between
89 the Bermuda High and the Icelandic Low leads to the so-called North Atlantic Oscillation (NAO; Lamb & Pepler,
90 1987), which plays a key role in modulating the transport of North American pollution to the northwestern Atlantic
91 Ocean and northern Europe (Christoudias et al., 2012). During the positive NAO phase (i.e., stronger Bermuda High
92 and Icelandic Low), anomalously stronger westerlies across the North Atlantic result in more North American
93 pollution over the WNAO and toward Europe, while during the negative NAO phase (i.e., weaker Bermuda High and
94 Icelandic Low), weaker westerlies lead to presence of less North American pollution in those regions.

95 On synoptic scales, the North American outflow of trace gases and aerosols to the WNAO is dominantly driven
96 by mid-latitude cyclones (Cooper et al., 2002; Li et al., 2005; Luan and Jaegle, 2013), which consist of four main
97 airstreams: warm conveyor belt (WCB), cold conveyor belt, dry airstream subsiding behind the cold front, and post
98 cold front boundary layer (BL) airstream (Carlson, 1998). Correspondingly, major transport mechanisms for North
99 American pollution outflow over the WNAO include horizontal advection within the BL behind the cold front, frontal
100 lifting by the WCB (ahead of the cold front), and convective lifting of continental pollution followed by westerly
101 transport in the free troposphere (Creilson et al., 2003; Li et al., 2002). For instance, Fast et al. (2016) identified key
102 processes responsible for the aerosol layers observed over Cape Cod, Massachusetts, and over the North Atlantic
103 Ocean (several hundred kilometers downwind) during the Two-Column Aerosol Project (TCAP) conducted during
104 July 2012. The aerosol layers observed in the free troposphere resulted from mean vertical motions associated with
105 synoptic-scale convergence ahead of a cold front, which lifted aerosols from the BL. Convection has been shown as
106 an effective mechanism for ventilating the U.S. continental BL, particularly in summer over the central and
107 southeastern U.S. (e.g., Li et al., 2005; Jacob et al., 1993; Dickerson et al., 1987). Recent aircraft observations from
108 the North Atlantic Aerosols and Marine Ecosystems Study (NAAMES) during 2015-2017 showed layers of sulfate,
109 black carbon, and organic aerosol enhancements in the free troposphere, suggesting long-range transport of continental
110 anthropogenic pollution and biomass burning (BB) emissions to the remote marine atmosphere (Croft et al., 2021).
111 Over the North Atlantic Ocean, North American pollution generally follows two transport pathways: one reaches
112 Europe in 4-5 days while the other is entrained in the Bermuda High anticyclone (Luan and Jaegle, 2013).

113 Tropospheric aerosols over the WNAO represent a mix of mainly anthropogenic, BB, biogenic, dust, and marine
114 emissions (see a comprehensive review by Sorooshian et al., 2020). The major aerosol types over the WNAO include
115 sulfate-nitrate-ammonium (SNA), black carbon (BC), organic aerosol (OA), dust, and sea salt. SNA aerosols are



116 mainly formed in the atmosphere through oxidation and neutralization of precursor gases sulfur dioxide (SO₂),
117 nitrogen oxides (NO_x), and ammonia (NH₃). They are water-soluble and subject to wet scavenging. Due to air pollution
118 regulatory policies in continental North America, anthropogenic SO₂ and NO_x emissions have been significantly
119 reduced over the past couple of decades (Feng et al., 2020; Streets et al., 2006), resulting in a decreasing trend in fine
120 particulate matter mass concentrations and aerosol optical depth (AOD), as well as tremendous improvements in air
121 quality in the eastern U.S. and eastern Canada (van Donkelaar et al., 2019; Coen et al., 2020; Provençal et al., 2017;
122 Jongeward et al., 2016; Yang et al., 2018; Corral et al., 2021).

123 Sources of light-absorbing BC aerosols are both anthropogenic and natural (e.g., wildfires) in nature. OA is
124 either directly emitted (primary OA or POA) or formed in the atmosphere (secondary OA or SOA). SOA includes an
125 anthropogenic component from oxidation of aromatic hydrocarbons, and a biogenic component from oxidation of
126 biogenic volatile organic compounds such as terpenes. Many studies have characterized the impact of BB sources in
127 Alaska, western/Central Canada, western U.S. on the extended WNAO region, especially during the ICARTT and
128 TCAP field campaigns (Neuman et al., 2006; Berg et al., 2016). It has been shown that BB emission injection heights
129 involve large uncertainties (e.g., Pfister et al., 2006). Smoke plume heights derived from MISR/Terra observations
130 over North America ranged from a few hundred meters up to 5 km above the ground (Val Martin et al., 2010) and a
131 relatively high percentage of total BB emissions is injected above the BL in the North American boreal regions (Zhu
132 et al., 2018). Recently, Mardi et al. (2021) characterized BB aerosol events over the U.S. east coast and Bermuda over
133 the WNAO between 2005-2018 using ground-based and satellite observations in conjunction with MERRA-2
134 reanalysis data. More frequent BB events are found to occur in Jun.-Aug. over the northern part of the East Coast with
135 sources from western North America, while more events are identified in Mar.-May over the southeast U.S. and
136 Bermuda with sources from southern Mexico, Yucatan, Central America, and the southeast U.S. That study along
137 with others (Edwards et al., 2021) point to cloud-BB aerosol interactions over the East Coast and the WNAO. Long-
138 range transported North American wildfire aerosols, e.g., those from the Canadian wildfires in Aug. 2017 with the
139 extreme injection height of ~ 12 km, can be observed in the marine BL of eastern North Atlantic after descending in
140 the dry intrusion behind mid-latitude cyclones (Zheng et al., 2020). The August Complex “Gigafire” took place in
141 mid-August 2020 and the California Creek fire occurred in early September 2020, ranked among the top five in
142 California wildfire history (Zhuang et al., 2021). These fires are expected to have important impacts on trace gases
143 and aerosols, especially carbonaceous aerosols, over the east coast and the WNAO during the summer campaign of
144 ACTIVATE 2020.

145 Dust over the WNAO can be transported from North Africa, North America, and Asia. Dust over the northeast
146 U.S. is mainly transported in the lower and middle troposphere (2-6 km; Zhang et al., 2019) and long-range transport
147 of Asian dust in spring can reach the eastern US (Jaffe et al. 2003; DeBell et al., 2004). North African dust is
148 transported to the eastern US and the WNAO in summer (Jun.-Aug. maximum; Aldhaif et al., 2020) and the
149 trajectories are typically at ~ 1 km altitude (Savoie & Prospero, 1977; Perry et al., 1997). Contribution of North
150 American dust to the outflow to the WNAO is typically small (Corral et al., 2021). Modeling and observational studies
151 have found that an understanding of the dust loading and spatial (especially vertical) distribution over the WNAO is
152 still lacking (Colarco et al., 2003; Peyridieu et al., 2010; Generoso et al., 2008; Kim et al., 2014). Sea spray aerosols



153 are primarily generated by air bubbles bursting at the ocean surface resulting from wind stress and are composed of
154 inorganic sea salt and organic matter (de Leeuw et al., 2011; Quinn and Bates, 2014). Sea salt aerosols (SS) are a
155 major source of CCN, including giant CCN, over the WNAO (Gonzalez et al., 2022), and thus have indirect effects
156 on cloud, precipitation, and climate. As represented in MERRA-2, sea salt along with sulfate contribute most to total
157 AOD over the WNAO (Corral et al., 2021). MERRA-2 sea salt AOD over the WNAO is typically highest in winter
158 months and lowest in summer (Dadashazar et al., 2021; Aldhaif et al., 2021), consistent with sea salt mass
159 concentrations observed at IMPROVE sites along the U.S. East Coast (Corral et al., 2021). While sea salt is typically
160 the largest contributor to aerosol mass and extinction over the remote ocean, signatures of long-range transport of
161 anthropogenic, BB, and dust emissions are often present, as shown by Silva et al. (2020) in a model analysis of sun
162 photometer observations of AOD from two island sites over the North Atlantic.

163 The ACTIVATE mission deployed two aircraft (HU-25 Falcon and King Air) flying in coordination, with the
164 Falcon making in situ measurements in the lower troposphere and the King Air providing remote sensing
165 measurements of aerosols and clouds in the same vertical column from an altitude of 8-10 km while also launching
166 dropsondes. Flight hours totaled ~73 and ~60 for Falcon (~59 and ~67 for King Air) during the winter (Feb. 14 – Mar.
167 12, 2020) and summer (Aug. 13 – Sep. 30, 2020) deployments of ACTIVATE’s first year of flights, respectively.
168 These intensive aircraft in situ and remote sensing observations of aerosols provide an opportunity to test the current
169 understanding of tropospheric aerosol sources and distribution as well as associated processes as represented by state-
170 of-the-art global models. In this paper, we evaluate the GEOS-Chem CTM driven by the MERRA-2 assimilated
171 meteorology (with marine POA emissions) against ACTIVATE aircraft measurements as well as ground and satellite
172 observations for the periods of the winter and summer campaigns of ACTIVATE 2020. We determine the sources,
173 transport, and distribution of tropospheric aerosols over the WNAO. The analysis also serves as a description of
174 aerosol conditions in the region during the two campaigns. We plan to address the following science questions: (1)
175 What are the major outflow pathways and transport mechanisms for the export of North American anthropogenic
176 pollution to the WNAO in winter and summer?; (2) Can a state-of-the-art chemical transport model reproduce the
177 distribution and variability of tropospheric aerosols over the WNAO as observed during ACTIVATE?; (3) What are
178 the sources of tropospheric aerosols as well as the relative contributions of terrestrial versus oceanic sources to the
179 aerosol mass, AOD, and their variability over the WNAO in winter and summer?; and (4) How is the summer
180 compared to the winter with respect to the sources, transport, and distribution of aerosols over the WNAO?

181 This paper is structured as follows. Section 2 introduces the GEOS-Chem model (with bulk aerosol) and model
182 simulations, and section 3 describes the observational data sets used in this study. Section 4 delineates the
183 meteorological setting and transport pathways for pollution over the WNAO. Section 5 presents the model simulated
184 aerosol composition and distribution over the WNAO (section 5.1) and model evaluations with aircraft in situ
185 measurements of CO, sulfate, nitrate, ammonium, and OA concentrations (section 5.2), AERONET AOD
186 measurements (section 5.3), and aerosol extinction profiles from aircraft HSRL-2 lidar and CALIOP/CALIPSO
187 satellite retrievals. Section 6 presents model source attributions of AODs over the WNAO during winter/summer
188 2020, followed by summary and conclusions in section 7.

189



190 2. Model Description

191 We use the GEOS-Chem global chemical transport model (www.geos-chem.org) version v11-01
192 (http://wiki.seas.harvard.edu/geos-chem/index.php/GEOS-Chem_v11-01) to simulate the sources, transport, and
193 distribution of tropospheric aerosols over the WNAO. The model is driven by the MERRA-2 assimilated meteorology
194 (at a horizontal resolution of $2^\circ \times 2.5^\circ$ with 72 levels) from the NASA Global Modeling Assimilation Office. It includes
195 a detailed description of stratospheric and tropospheric chemistry fully coupled through the Unified tropospheric-
196 stratospheric Chemistry eXtension (UCX; Eastham et al., 2014). Gas-phase tropospheric oxidant chemistry was
197 originally described by Bey et al. (2001) and its coupling with the SNA aerosol thermodynamics was developed by
198 Park et al. (2004). SNA thermodynamics are computed with the ISORROPIA thermodynamic module (Fontoukis and
199 Nenes, 2007). BC follows Wang et al. (2014), OA is after Pye et al. (2010) and Pye and Seinfeld (2010), and marine
200 primary OA (MPOA) uses the scheme of Gantt et al. (2015) based on monthly mean MODIS chlorophyll-a
201 concentrations. SOA follows the simplified Volatility Basis Set (VBS) scheme of Pye et al. (2010). Sea salt aerosol
202 emissions use the empirical source function of Jaegle et al. (2011) with a dependency on surface wind speed and sea
203 surface temperature. The model assumes two dry sea salt size bins, one for accumulation mode (radius 0.01-0.5 μm)
204 and the other for coarse mode (radius 0.5-8 μm). Dust emissions in GEOS-Chem were described by Fairlie et al.
205 (2007) and we use here the Dust Entrainment and Deposition (DEAD) scheme (Zender et al., 2003) with the size
206 distributions updated by Zhang et al. (2013). Aerosol optical depth is calculated for each aerosol type using local
207 relative humidity and prescribed optical properties (Martin et al., 2003; Drury et al., 2010; Ridley et al., 2012; Kim et
208 al., 2015). External mixing of aerosols is assumed. The input meteorological archives have 3-hour temporal resolution
209 for 3-D fields and 1-hour resolution for 2-D fields. The model time steps (10 min for transport and 20 min for
210 chemistry) are chosen to optimize both simulation accuracy and computational speed (Philip et al., 2016).

211 The model uses the TPCORE advection algorithm (Lin and Rood, 1996), computes convective transport from
212 the MERRA-2 convective mass fluxes (Wu et al., 2007), and uses the non-local scheme for BL mixing (Lin and
213 McElroy, 2010). The aerosol wet deposition scheme is described by Liu et al. (2001) and includes first-order rainout
214 and washout due to stratiform precipitation and scavenging in the convective updrafts. Scavenging of aerosol by snow
215 and cold/mixed precipitation is described by Wang et al. (2011, 2014). For stratiform precipitation scavenging, we
216 use the MERRA-2's spatiotemporally varying cloud condensed water content (CWC), following the revised scheme
217 of Luo et al. (2019, 2020), in the standard simulations in this study. For comparison, simulations prescribed with a
218 fixed CWC of $1.0 \times 10^{-3} \text{ kg m}^{-3}$ comparable to observed upper limits (Del Genio et al., 1996; Wang et al., 2011) are
219 also presented. On the other hand, MERRA-2 cloud cover and precipitation over the U.S. East Coast and WNAO are
220 biased low relative to satellite observations (Wu et al., 2022; Bosilovich et al., 2015, 2017) and thus introduce
221 uncertainty in the model scavenging processes. Aerosol dry deposition uses the resistance-in-series scheme of Wesely
222 (1989), with deposition to snow/ice surfaces from Fisher et al. (2011). Gravitational settling is as described by Fairlie
223 et al. (2007) for dust and Alexander et al. (2005) for coarse sea salt.

224 Global anthropogenic emissions are based on the EDGAR v4.2 emissions inventory for 2008. We use the 2011
225 EPA National Emissions Inventory (NEI11) emissions as implemented by Travis et al. (2016) over the U.S. with
226 national annual scaling factor updated for 2018 (Yu et al., 2018), CAC emissions inventory over Canada, BRAVO



227 emissions inventory over Mexico, EMEP emissions inventory over Europe, and the MIX emissions inventory (for
228 year 2010) over China (Li et al., 2014). Shipping emissions are from the EMEP inventory (Vestreng et al., 2007).
229 Aircraft emissions are from the AEIC inventory for 2005 (Stettler et al., 2011). The NEI11 emissions inventory
230 contains biofuel emissions. BB emissions are from the Quick Fire Emissions Dataset (QFED v2.5r1; Darnenov and
231 da Silva, 2015), which is based on the location and fire radiative power (FRP) obtained from the Moderate Resolution
232 Imaging Spectroradiometer (MODIS) Level 2 fire products and the MODIS geolocation products. QFED provides
233 daily mean emissions of trace gases and aerosols at $0.1^\circ \times 0.1^\circ$ horizontal resolution. BB emissions are injected within
234 the depth of the PBL in our standard simulations. In a separate set of simulations, they are also injected to the 0-5.5
235 km or 2-10 km altitude range to investigate the sensitivity of model results to BB emission injection heights. The
236 choice of these higher injection heights is based on the following previous studies. A substantial fraction of North
237 American fire emissions is injected to the free troposphere (e.g., val Martin et al., 2010). 35% of the QFED BB
238 emissions are also distributed between 3.5-5.5 km in the NASA GEOS-CF model (Keller et al., 2021; Fischer et al.,
239 2014). An explosive pyrocumulonimbus (pyroCb) cloud from Californian Creek fire on September 9, 2020 was
240 reported with the plume height peaking above 10 km (Carr et al., 2020). Biogenic emissions are calculated online
241 using the MEGAN model (Guenther et al., 2012). Marine DMS emissions are calculated as a product of the
242 climatological monthly mean surface seawater DMS concentration (Lana et al., 2011) and sea-to-air transfer velocity,
243 as implemented by Breider et al. (2017). Lightning NO_x emissions are constrained by the Lightning Imaging Sensor
244 and the Optical Transient Detector (LIS/OTD) climatological observations of lightning flashes, as described by
245 Murray et al. (2012).

246 We perform model simulations for the periods of December 1, 2019 – March 31, 2020 and June 1 – September
247 30, 2020 with the first two months as the spin-up period. Model sensitivity experiments are also conducted to
248 investigate the impacts of using fixed CWC in model scavenging, sensitivity to BB emission injection height, and
249 impacts of various emission types (anthropogenic, BB, biogenic, marine, and dust). The impacts are quantified by the
250 difference in simulation results from the standard model and the sensitivity experiments. **Table 1** lists all model
251 experiments. Hourly, daily, and campaign-average output are saved for analysis.

252

253 **3. Observational Data Sets**

254 **ACTIVATE aircraft data.** During ACTIVATE, the HU-25 Falcon aircraft made in situ measurements of
255 carbon monoxide (CO) mixing ratios and aerosol concentrations during each flight (duration of ~3.5 daytime hours).
256 CO measurements were made with a Picarro G2401 gas concentration analyzer (DiGangi et al., 2021). Submicron
257 non-refractory aerosol composition was measured by the High-Resolution Time-of-Flight Aerosol Mass Spectrometer
258 (HR-ToF-AMS; Aerodyne) (DeCarlo et al., 2008; Hilario et al., 2021), operated in 1 Hz Fast-MS mode and averaged
259 to 30 s time resolution. AMS data were collected downstream of an isokinetic double diffuser inlet (BMI, Inc.) and
260 also sampled downstream of a counterflow virtual impactor (CVI) inlet (BMI, Inc.) when in cloud (Dadashazar et al.,
261 2022; Shingler et al., 2012); only the former is used in this study. AMS measurements are reported at the standard
262 temperature (273.15 K) and pressure (1013.25 hPa). One-minute merged Falcon data are used in this study. We also
263 use the King Air's nadir-viewing High Spectral Resolution Lidar-2 (HSRL-2) retrievals of vertically resolved aerosol



264 extinction coefficient at 532 nm (Ferrare et al., 2023). The HSRL-2 instrument has been used in previous aircraft
265 missions and readers are referred to Burton et al. (2018) for further information about its operational details. The
266 FLEXPART model (Stohl et al., 1998) is used to identify the origin of air masses associated with high HSRL-2 aerosol
267 extinction during an event of the long-range transport of a western U.S. fire plume. ACTIVATE aircraft data and
268 FLEXPART model output are described in detail by Sorooshian et al. (2023) and available at:
269 <https://doi.org/10.5067/SUBORBITAL/ACTIVATE/DATA001>.

270 **CSN, IMPROVE, and NADP.** Surface aerosol composition (SO_4^{2-} , NO_3^- , NH_4^+) data for the eastern U.S. were
271 obtained from the Chemical Speciation Network (CSN) and the Interagency Monitoring of Protected Visual
272 Environments (IMPROVE) network (Solomon et al., 2014; Malm et al., 1994). IMPROVE does not include NH_4^+
273 measurements. Daily observational data for 2020 were obtained from the Federal Land Manager Environmental
274 Database at the Cooperative Institute for Research in the Atmosphere (CIIRA), Colorado State University
275 (<https://views.cira.colostate.edu/fed/>; last access on 31 July 2022). The readers are referred to that website for methods
276 of chemical characterization, uncertainties, detection limits, and data downloading. Aerosol wet deposition
277 composition (SO_4^{2-} , NO_3^- , NH_4^+) data from the ensemble of eastern U.S. sites are from the National Trends Network
278 (NTN) of the U.S. National Atmospheric Deposition Program (NADP, <https://nadp.slh.wisc.edu/>). The NTN measures
279 total weekly wet deposition of SO_4^{2-} , NH_4^+ , and NO_3^- and we use monthly mean data downloaded from
280 <http://views.cira.colostate.edu/fed/>. Since the NTN wet deposition of SO_4^{2-} includes contribution from SO_4^{2-} resulting
281 from oxidation of SO_2 in rainwater, for comparison with NTN measurements we calculate the model sulfur wet
282 deposition fluxes as the sum of the SO_4^{2-} wet deposition flux and 150% (based on the ratio of the molar masses of SO_2
283 and SO_4^{2-}) of the model estimated SO_2 wet deposition (Appel et al., 2011). Similarly, the model estimates of NO_3^-
284 (NH_4^+) wet deposition include 98.4% (106%) of the model estimates of HNO_3 (NH_3) wet deposition. Gartman (2017)
285 described the analysis and quality assurance of the NADP data. The IMPROVE and NADP data sets were previously
286 used by Corral et al. (2020, 2021) to analyze aerosols and wet deposition chemistry over the U.S. East Coast.

287 **AERONET and MODIS.** We use AOD measurements from the Aerosol Robotic NETwork (AERONET,
288 <http://aeronet.gsfc.nasa.gov>; Holben et al., 1998), a ground-based aerosol remote sensing network. Level 2.0 daily
289 data used are based on the Version 3 algorithm and are cloud screened and quality assured (Giles et al., 2019; Smirnov
290 et al., 2000). AERONET AOD data were obtained for three sites during Feb.-Mar. and Aug.-Sep. 2020: NASA LaRC
291 (37.10°N, 76.38°W), NASA GSFC (38.99°N, 76.84°W), Tudor Hill, Bermuda (32.26°N, 64.88°W). For comparison
292 with GEOS-Chem AODs at 550 nm, AERONET AOD values at 440 nm were converted to 550 nm using the
293 AERONET 440-675 nm Angstrom exponent. Estimated uncertainties in AERONET AODs are on the order of ~0.01-
294 0.02 (Eck et al., 1999; Dubovik et al., 2000). Satellite retrieved products of AODs are available from MODIS on Aqua.
295 MODIS has a ~2330 km swath and provides nearly global coverage daily. We use the MODIS/Aqua Level 3 daily
296 (MYD08_D3) AOD product at 550 nm and 1°×1° horizontal resolution (Collection 6.1; scientific data set or SDS
297 named “Aerosol_Optical_Depth_Land_Ocean_Mean”) from the Dark Target (DT) retrieval algorithm (Sayer et al.,
298 2014; Levy et al., 2013; Hubanks et al., 2019). This SDS contains only AOD values for any DT-ocean retrieval having
299 the Quality Assurance Confidence (QAC) >=1 and any DT-land retrievals having QAC=2 (good confidence) or 3



300 (high confidence) (Levy et al., 2013; R.C. Levy, personal communication, 2019). Collection 6.1 data are available
301 from <https://ladsweb.modaps.eosdis.nasa.gov/search/>.

302 **CALIPSO.** The Cloud-Aerosol Lidar with Orthogonal Polarization (CALIOP), on board the Cloud-Aerosol
303 Lidar and Infrared Pathfinder Satellite Observations (CALIPSO) platform, has been providing aerosol vertical profile
304 measurements of the Earth's atmosphere on a global scale since June 2006 (Winker et al., 2010). We use the version
305 4.51 CALIOP Level 2 Aerosol Profile products with a vertical resolution of 60 m and horizontal resolution of 5 km
306 over an altitude range of 30 km to -0.5 km, and only quality screened extinction samples are used in the analysis.
307 Specifically, aerosol layers with Cloud Aerosol Discrimination (CAD) scores less than -100 or greater than -20 are
308 rejected to avoid low-confidence aerosol classifications (Liu et al., 2019). Also, aerosol layers with the extinction
309 Quality Control (QC) flag not equal to 0, 1, 16, and 18 are rejected to remove low-confidence extinction retrievals,
310 while aerosol extinction samples with the extinction uncertainty equal to 99.99 km^{-1} as well as those at lower altitudes
311 below these samples are rejected to remove unreliable extinction values (Yu et al., 2010; Winker et al., 2013; Kim et
312 al., 2018; Tackett et al., 2018).

313 In addition, we apply the same data averaging approach that was used to generate the CALIPSO version 4 Level
314 3 aerosol products (Tackett et al., 2018). The following quality screening and data selection techniques are applied.

315 1) When creating the averaged profiles used in this work, CALIOP Level 2 range bins in "clear air" regions
316 where no aerosol is detected are typically assigned aerosol extinction coefficients of 0 km^{-1} . An exception to this
317 convention is exercised for regions of "clear air" lying below aerosol layers with base heights lower than 250 m.
318 Because we assume the atmosphere is well mixed below 250 m, excluding these bins avoids introducing low biases
319 near the Earth's surface.

320 2) Aerosol layers detected at 80 km horizontal resolution that are not vertically or horizontally adjacent to another
321 aerosol layer detected at finer spatial resolutions (i.e., 5 km or 20 km) are assumed to be noise-induced false positive
322 detections, and hence are discarded.

323 3) Layers classified as aerosols that are detected at 80 km horizontal resolution with base altitudes above 4 km
324 and are in contact with ice clouds are assumed to be misclassified cirrus "fringes" (Liu et al., 2019), and are also
325 discarded.

326 4) Aerosol samples in the surface-attached opaque layer (beneath the maximum surface elevation), for which
327 the extinction is greater than 2 km^{-1} and at least 10 times higher than the extinction of the layer above, are rejected to
328 avoid surface contamination.

329 5) In any 5-km profile in the CALIOP Level 2 data product, range bins identified as aerosol that have embedded
330 cloud fractions greater than 97% are rejected, as are all samples at lower altitudes in the profile. Rejecting these
331 samples reduces the likelihood of cloud contamination.

332 The details of the quality screening to generate the Level 3 aerosol profile product are described in Winker et al.
333 (2013), Tackett et al. (2018), and the CALIPSO Data Users' Guide ([https://www-
334 calipso.larc.nasa.gov/resources/calipso_users_guide/](https://www-calipso.larc.nasa.gov/resources/calipso_users_guide/)). CALIOP aerosol extinction coefficients at 532 nm were
335 horizontally and vertically regridded onto the GEOS-Chem grids by averaging all quality screened extinction values
336 within each grid box. CALIOP data are available at <https://subset.larc.nasa.gov/calipso>.



337

338 **4. Meteorological Settings and Transport Pathways**

339 In this section we describe the mean states of meteorological settings, BL outflow, and vertical transport of
340 pollution during Feb.-Mar. and Aug.-Sep. ACTIVATE 2020, as represented by the MERRA-2 reanalysis and GEOS-
341 Chem model simulation. They will facilitate the interpretation of model results as well as comparisons with
342 observational data in section 5. **Fig. 1** shows the tracks of 22 HU-25 (Falcon) flights during Feb.-Mar. ACTIVATE
343 2020 and 18 flights during Aug.-Sep. ACTIVATE 2020, with flights typically transiting via waypoints of ZIBUT
344 (36.93°N, 72.67°W) and OXANA (34.36°N, 73.75°W) to avoid military restricted air space. The aircraft sampling
345 domain is divided at 36°N into two box regions: the north ("N"; 36-39°N, 69-75°W) and the south ("S"; 32.5-36°N,
346 71-75.5°W) for this analysis.

347 **Meteorological settings.** The winter and summer campaign periods feature contrasting atmospheric circulation
348 patterns and meteorological conditions. **Fig. 2a** and **Fig.2b** show MERRA-2 near surface air temperature, surface
349 level pressure, relative humidity, vertical pressure velocity (ω), total and convective precipitation, and PBL heights
350 (based on the total eddy diffusion coefficient of heat with a threshold value of $2 \text{ m}^2 \text{ s}^{-1}$; McGrath-Spangler and Molod,
351 2014) over the WNAO averaged over Feb.14-Mar.12 and Aug.13-Sep.30, respectively. Also shown in the figures are
352 the model simulated CO concentrations and aerosol extinction coefficients (at 550 nm) at 945 hPa. In winter, the lower
353 troposphere of the WNAO region was dominated by westerly wind and air masses from continental North America in
354 the north and anticyclonic winds in the southeast. The latter was associated with the Bermuda High located to the east
355 of the domain. A strong NW-SE horizontal gradient in surface temperature extended from the SE U.S. coast towards
356 NE/E, consistent with frequent passages of cold fronts driven by the Northern Hemisphere mid-latitude cyclones and
357 the warm Gulf Stream sea surface temperatures in Feb.-Mar (e.g., Seethala et al., 2021). The ACTIVATE flights in
358 the two-box region sampled this continental outflow extensively. Flights to the north often occurred during post-
359 frontal conditions, reflecting one of the mission objectives to sample and study MBL clouds, especially during cold
360 air outbreaks in winter that have been the subject of recent work (Tornow et al., 2022; Seethala et al., 2021; Corral et
361 al., 2022; Li et al., 2022; Chen et al., 2022). In addition to lower temperature, the post-frontal air was characterized
362 by subsiding motion with lower relative humidity and precipitation (dry air) as well as lower BL height. In particular,
363 the S box region experienced stronger uplifting and precipitation (predominantly stratiform) ahead of the cold fronts.
364 It suggests stronger aerosol scavenging associated with the southern cluster of flights. Model BL CO concentrations
365 showed large land-to-sea gradients over the WNAO, resulting from the fact that North American pollution outflow
366 was much stronger in the N box region (westerly winds) than in the S box region, which was often intruded by low-
367 latitude marine air (southwesterly winds), during Feb.-Mar. 2020. The more inhomogeneous distribution of aerosol
368 extinction coefficients (compared to CO) generally reflects the shorter aerosol lifetime, as well as more complex
369 processes and their interactions involved in speciated aerosol emissions, transport, heterogeneous chemistry,
370 photochemistry, and wet scavenging.

371 In summer, while midlatitude cyclones and westerlies move northward, the Bermuda High strengthened and
372 extended westward with southwesterly offshore along the U.S. SE coast (~32-36°N) and easterly trade winds in the
373 subtropics (<30°N; **Fig. 2b**). Compared to the wintertime, the horizontal gradients in surface temperature, RH, vertical



374 pressure velocity, precipitation, and PBL height were much weaker in the N and S box regions. However, convective
375 precipitation was much stronger in summer and accounted for ~50-80% of the total precipitation in the flight domain.
376 Despite a large land-to-sea gradient, model simulated BL CO concentrations were much lower due to CO oxidation
377 by higher OH in summer. In contrast to the wintertime, BL aerosol extinction over the WNAO during summer
378 exhibited large enhancements compared to those over land, suggesting major aerosol sources of marine origin.

379 **Boundary-Layer outflow of pollution.** Transport in the BL behind cold fronts is a major mechanism for the
380 North American pollution outflow to the WNAO. It exerts large impacts on the BL trace gases and aerosol composition
381 as well as their spatiotemporal evolution in the ACTIVATE flight domain. **Fig. 3** shows Hovmöller diagrams of model
382 daily mean air temperature, CO, and sea salt concentrations at 950 hPa along 72.5°W (near the longitude of waypoint
383 ZIBUT) over the WNAO during Feb. 14 - Mar. 13 and Aug. 13 – Sep. 30. During Feb.-Mar. 2020 (left column, **Fig.**
384 **3**), there were about four major periods with cold fronts passing through the study area, as indicated by the wavy
385 pattern of near-surface temperature day-to-day variations. During frontal passages, CO pollution was swept in the BL
386 behind the cold fronts southeastward to the ACTIVATE flight latitudes (32.4-39.8°N). On Feb. 15-16, Feb. 28, Mar.
387 1, and Mar. 7, the BL outflow of CO reached as far as south of 32°N. On the other hand, advection of warm marine
388 air from low-latitudes resulted in low CO concentrations across the flight domain. Enhanced sea salt aerosols were
389 often associated with strong wind and warm air from the south (left bottom panel, **Fig. 3**). A remarkable sea salt event
390 occurred because of strong surface wind speed on March 7 during a cold air outbreak. During Aug.-Sep. 2020 (right
391 column, **Fig. 3**), cold air intrusion deep into the flight domain did not take place until late September since midlatitude
392 cyclones were shifted northward in summer. High CO events within the ACTIVATE flight latitude ranges appeared
393 associated with transport of anthropogenic or wildfire emissions that occurred between 35-45°N. Two strong events
394 of high sea salt concentrations occurred on September 10-12 and 19-22. The former was due to high surface winds
395 associated with a westward moving low-pressure system. The latter resulted from the strong winds during a cold air
396 outbreak that lasted for several days when cold air swept along a NE-to-SW corridor off the east coast over the whole
397 flight domain. It lasted until a new cold front moved into the domain on September 23, resulting in enhanced CO
398 during September 23-25.

399 **Vertical Transport.** Major pathways for vertical transport of trace gases and aerosols over the North American
400 continental outflow region include uplifting ahead of cold fronts, convective transport, and BL turbulent mixing. **Fig.**
401 **4** shows model resolved large-scale vertical fluxes, convective fluxes, and PBL turbulent mixing fluxes of CO (**Fig.**
402 **4a&4b**) and sea salt (**Fig. 4c&4d**) at 1 km and 2 km, respectively, averaged over the periods of Feb. 14 - Mar. 12 and
403 Aug. 13 – Sep. 30, respectively, 2020. During Feb.-Mar. 2020, large-scale vertical transport ahead of cold fronts
404 apparently played a dominant role in lifting CO out of the BL over the U.S. east coast and two flight box regions (**Fig.**
405 **4a**), followed by rapid eastward transport in the free troposphere. Convection was also important in this role, especially
406 in the S box region. It became even more important in summer during Aug.-Sep. 2020 when convective fluxes of CO
407 were comparable to large-scale vertical fluxes (**Fig. 4b**). For sea salt, by contrast, BL turbulent mixing was found to
408 be the dominant process responsible for upward transport of sea salt within and ventilation out of the BL over the
409 flight domain in winter (**Fig. 4c**), while both convection and turbulent mixing were important in uplifting sea salt to
410 the free troposphere in summer (**Fig. 4d**).



411

412 **5. Simulated aerosols over the WNAO and model evaluations**

413 **5.1 Simulated aerosol composition, distribution, and loading over the WNAO**

414 In this section, we describe the horizontal, vertical distributions, and mass loadings of aerosol species over the
415 WNAO during Feb.-Mar. and Aug.-Sep. 2020, as simulated by GEOS-Chem. **Fig. 5** shows the 929 hPa maps of model
416 simulated mass concentrations of sulfate-nitrate-ammonium (SNA), black carbon (BC), primary organic aerosol
417 (POA), secondary organic aerosol (SOA), sea salt, and dust averaged over the period of Feb. 14 - Mar. 12, 2020. Also
418 shown are longitude-altitude cross-sections of each aerosol species averaged over 33-39°N. The distribution patterns
419 of SNA, BC, POA, and SOA resemble those of CO (**Fig. 2a**), reflecting the frequent North American continental
420 outflow of traces gases and aerosols in the BL behind cold fronts to the WNAO. Among aerosol species of North
421 American origin, POA shows the highest mass in the study domain while POA and nitrate exhibit strong gradients
422 with mass concentrations sharply decreasing eastward. As will be discussed in section 5.2, POA in the study domain
423 are attributed to North American anthropogenic, biofuel, and southeast U.S. BB emissions. Sulfate mass concentration
424 shows a weaker gradient because DMS from ocean is also a source of SO₂ and sulfate. Sea salt has the largest aerosol
425 mass over the WNAO, with maximum in the easterly trade wind region and to the east of the north flight domain.
426 Abundances of BC, SOA, and dust across the flight domain are relatively small. Dust to the southeast of Bermuda is
427 a result of long-range transport from Africa. As shown in the vertical cross-section plots, aerosol masses are mostly
428 restricted in the lower troposphere (< 2-3 km).

429 **Fig. 6** shows the same plots as in **Fig. 5**, but for Aug. 13 – Sep. 30, 2020. Sulfate concentrations in the BL
430 increased significantly relative to winter because of stronger production of sulfate from oxidation of SO₂ in summer.
431 The stronger west-to-east gradient in sulfate concentrations was partly due to the lack of cold front passages as
432 midlatitude cyclones shift to higher latitudes in summer. Nitrate concentrations in the BL decreased substantially due
433 to higher temperatures that limit particle-phase ammonium nitrate (a major chemical form of nitrate associations) as
434 well as the competition for ammonium by more sulfate. The simulated high nitrate concentrations in the upper
435 troposphere between 33-39°N are presumably from lightning NO_x emissions. The spatial pattern of BC concentrations
436 over land is consistent with a major source from the western U.S. BB in summer (versus primarily from anthropogenic
437 and biofuel emissions in winter). However, BC remains a small contribution to the outflow of aerosols. POA
438 concentrations are high in the BL albeit lower than in winter, with a peak in the lower free troposphere (at ~2 km
439 altitude) over the WNAO. Its primary sources are North American BB and anthropogenic emissions. Much higher
440 SOA concentrations reflect the larger production from strong oxidation of biogenic VOCs from the southeast US in
441 summer. The vertical extent of the major North American continental outflow aerosols was significantly higher than
442 that in winter, reflecting the impact of summertime convective lifting. BL sea salt concentrations increased in summer
443 over the WNAO, especially from the ACTIVATE flight areas to Bermuda, because of stronger winds (section 4). Dust
444 amounts also significantly increased because of long-range transport of dust emissions from North Africa. It is noted
445 that African dust can be transported to the Gulf of Mexico and then northward to the eastern U.S., as shown by
446 enhanced dust concentrations in the BL between 80-85°W (dust vertical cross-section, **Fig. 6**).



447 As a summary of model simulated aerosols, **Fig. 7** shows model simulated mean concentrations ($\mu\text{g m}^{-3}$ STP) or
448 AODs of each aerosol species (bar graph) and their fractions of the total aerosol mass or AODs (pie charts) for the
449 flight areas (“N” and “S” in **Fig. 1**) over the periods of Feb. 14 – Mar. 12 and Aug. 13 – Sep. 30 ACTIVATE 2020,
450 respectively. Sea salt is a dominant fraction of total aerosol mass in the BL in both winter (53%) and summer (72%),
451 followed by organics with 24% in winter and 13% in summer. Higher sea salt mass concentration is also the main
452 reason for higher total aerosol mass in summer. SNA is about 20% of the total aerosol mass in winter and 11% in
453 summer. Dust accounts for 1% in winter and 3% in summer, with the latter season’s increase reflecting more efficient
454 transport from the eastern Atlantic and North Africa by the subtropical trade winds. Sea salt, SNA, and OA are the
455 main contributors to the mean total AOD in the flight areas, with the following percentage contributions: SS: 41%
456 (winter), 62% (summer); OA: 26% (winter), 16% (summer); and SNA: 31% (winter), 20% (summer). The much larger
457 fraction of AOD (versus aerosol mass) from SNA is ascribed to the strong hygroscopic growth of those fine aerosols,
458 similar to OA.

459

460 **5.2 Model evaluation with aircraft in situ measurements and source analysis**

461 In this section we evaluate model simulations of CO and aerosols with ACTIVATE aircraft in situ measurements.
462 A series of GEOS-Chem experiments with different configurations were performed to investigate the impacts of key
463 aerosol-related processes in the model, including emission sources (anthropogenic and biofuel, BB, and marine), BB
464 emission injection height, and cloud water content (fixed value vs. MERRA-2, **Table 1**). **Fig. 8** and **Fig. 9** compare
465 model simulated vertical profiles of CO, SNA, and OA mixing ratios with Falcon aircraft Picarro and AMS
466 measurements during Feb.-Mar. and Aug.-Sep. 2020, respectively. It is noted that the observed profiles above 3 km
467 are probably biased because Falcon aircraft flew below 3 km most of the time. Also shown in the figures are model
468 results from simulations (**Table 1**) with (1) a fixed value for cloud water content used in aerosol scavenging
469 (“fixedCWC”), (2) BB emissions injected to the 0-5.5 km altitudes (for Aug.-Sep. 2020 only), (3) fossil fuel and
470 biofuel emissions turned off, (4) BB emissions turned off, or (5) marine emissions turned off, respectively. Values
471 (500 m-binned) are medians over all flights.

472 In winter, the aircraft observations showed a decreasing trend of CO, SNA, and OA aerosol concentrations with
473 altitude, with substantially higher concentrations in the BL as part of the strong North American continental outflow
474 of pollution and a sharp vertical gradient at ~ 1.0 km above the sea surface. The sharper gradient in aerosols than in
475 CO concentrations suggests that aerosols were scavenged during uplifting processes. The simulated profile of CO
476 concentrations is in good agreement with the observations. The model captures the observed sulfate concentrations in
477 the BL but underestimates them in the free troposphere, likely due to uncertainty in the model aerosol scavenging
478 scheme, as discussed below. Simulated nitrate concentrations in the BL are too high compared to observations. The
479 model reasonably captures the vertical distribution of ammonium concentrations, but the vertical gradient in the lower
480 troposphere is too strong. The simulated OA concentrations are biased high in the BL and biased low above ~ 4 km.
481 The model attributes CO and SNA aerosols mainly to anthropogenic emissions, as indicated by the large reduction in
482 their concentrations compared to the standard simulation (red lines, **Fig. 8**) when anthropogenic emissions are turned
483 off in the model (green lines, **Fig. 8**). The model suggests that while both anthropogenic and BB emissions are major



484 contributions to OA in the BL, BB is likely responsible for the OA enhancement at ~4.0 km, for which the model
485 predicted it at a lower altitude (~3.5 km). Injecting BB emissions to the altitude range of 0-5.5 km results in OA peak
486 concentrations (at ~3.5 km and ~5.0 km) much higher than observed, suggesting the 0-5.5 km injection height is too
487 high in winter (dark yellow line, **Fig. 8**). The effect of marine emissions on SNA and OA is small in the model.

488 Using the MERRA-2 interactive CWC (versus a fixed value) for the aerosol wet scavenging scheme in the model
489 has a large impact on simulated aerosol profiles over the flight domain. As shown in **Fig. 8** (blue lines), using the
490 MERRA-2 CWC enhances aerosol scavenging and results in lower aerosol concentrations in the troposphere. This is
491 mainly because generally the MERRA-2 CWCs for precipitating stratiform clouds are significantly smaller than the
492 assumed fixed value (1.0×10^{-3} kg m⁻³, **Table 1**), leading to a faster conversion from cloud water to the same amount
493 of precipitation and thus stronger scavenging. SNA aerosols are affected more compared to OA because they are more
494 soluble. The reduction in sulfate concentrations is substantial, especially in the middle and upper troposphere. The
495 model overestimate of sulfate in the MBL compared to aircraft AMS measurements is corrected by this update in wet
496 scavenging, but simulated concentrations above ~4 km are far too low, suggesting ice scavenging is too fast. This low
497 bias seems not as obvious for nitrate or ammonium, presumably due to the SNA thermodynamic equilibrium where
498 lower sulfate favors more nitrate associated with ammonium in the aerosol phase.

499 In summer, aircraft measured CO concentrations showed a relatively weak vertical gradient with much lower
500 concentrations in the BL compared to winter and enhancement layers in the middle and upper troposphere (~3-4 km
501 and ~5.5-6.5 km; **Fig. 9**). The former reflects the shorter CO lifetime in summer and the latter results from the long-
502 range transport of North American continental pollution as well as the western U.S. fire emissions. Observed sulfate
503 concentrations exhibited a strong vertical gradient with much higher levels in the BL compared to winter along with
504 enhancements at 3-4 km. The generally higher sulfate concentrations throughout the troposphere in summer reflect
505 stronger oxidation of SO₂ in both the gas phase and in-cloud (Dadashazar et al., 2022; Tai et al., 2010). The observed
506 nitrate concentrations in the BL have a median value close to that in winter but show much smaller variability. BL
507 ammonium and OA concentrations are substantially higher than in winter. All of nitrate, ammonium, and OA
508 observations show large enhancements between ~3.5 km and ~5 km.

509 The model reasonably reproduces the observed CO concentrations in the BL but fails to capture the observations
510 in much of the free troposphere, especially the magnitude of CO enhancements around ~4 km and ~6 km (red and
511 black lines, CO panel of **Fig. 9**). The reason for the latter is attributed to the model's inability to retain the western
512 U.S. BB CO plumes when reaching the eastern U.S. and the ACTIVATE flight areas. Nevertheless, clear reductions
513 of CO in the model simulations without BB or anthropogenic sources suggest both are important sources to CO in
514 summer over the WNAO.

515 For SNA and OA aerosols, the standard model simulation tends to underestimate the observed concentrations in
516 the BL in contrast to the wintertime (red and black lines, aerosol panels of **Fig. 9**). The model also underestimates
517 observations in most of the free troposphere, except for nitrate. The observed nitrate and OA layer enhancements
518 between 3-5 km are reasonably simulated, with the OA peak at slightly lower altitude (~3.5 km) and of much lower
519 concentration in the model. On the other hand, the model barely captures the sulfate and ammonium enhancements
520 observed in this layer. All these underestimated enhancements are largely improved or corrected by extending the BB



521 emission injection height from within the BL to 0-5.5 km (dark yellow lines, **Fig. 9**), suggesting that releasing the BB
522 emissions within the BL significantly limits the long-range transport of fire emissions in the free troposphere. The
523 model simulates too high nitrate concentrations in the mid-upper troposphere (>5 km). This is presumably due to the
524 large reduction in sulfate resulting from the use of MERRA-2 CWC in the aerosol scavenging scheme (red and blue
525 lines, sulfate panel of **Fig. 9**). Less sulfate shifts the SNA balance to favor nitrate in the model as more nitrate is
526 retained in the aerosol phase to neutralize ammonium in the SNA system. The model sensitivity experiments suggest
527 that SNA aerosols are predominantly from continental anthropogenic emissions in summer like winter. However, in
528 summer the BB emissions are also important sources of SNA between ~3-6 km. BB is the dominant source of OA
529 (mostly primary) in the free troposphere, whereas BB, anthropogenic, and marine emissions all contribute to OA in
530 the marine BL (with SOA accounting for less than one-third below 1 km). The large model underestimate of OA in
531 the BL is likely due to weak entrainment from the free troposphere, low production of SOA, and/or strong scavenging
532 associated with convective precipitation. The effect of marine emissions on sulfate appears more significant in the BL
533 and lower free troposphere compared to winter, reflecting the stronger oxidation of marine DMS and convective lifting
534 of DMS or its oxidation products (SO₂, sulfate) in summer.

535

536 **5.3 Model evaluation with AERONET AOD measurements**

537 Comparisons of model results with surface aerosol concentration observations from the IMPROVE and CSN
538 networks, aerosol deposition flux measurements from the NTN network of NADP, and satellite AOD measurements
539 from MODIS/Aqua are included in the **Supplement (section S1)**. In this section we evaluate model simulated AOD
540 with ground-based measurements from AERONET, with a focus on the eastern U.S. coastal region.

541 Continuous measurements of AOD from AERONET are used to evaluate the model performance in reproducing
542 the observed AOD magnitude and temporal variability as well as long-range transport of aerosol plumes. **Fig. 10**
543 shows model simulated daily AOD (at 550 nm) versus daily AOD measurements from two AERONET sites (NASA
544 LaRC, NASA GSFC) in the eastern U.S. and one site (Tudor Hill) located at Bermuda over the Atlantic Ocean during
545 Feb.-Mar. and Aug.-Sep., respectively, 2020. Model results are from the simulations (**Table 1**) “standard”,
546 “fixedCWC” (for winter only), “BB0-5.5km” (for summer only), “noanthbP”, “nobb”, and “nomari”, respectively.
547 Also shown in the figure are scatterplots of model AODs from the “standard” simulation versus AERONET AODs at
548 the three sites for winter and summer, respectively. In winter, AERONET AODs at LaRC and GSFC show large day-
549 to-day variability with an increasing trend towards early spring. Those at Tudor Hill exhibit smaller day-to-day
550 variability but much larger variability on a weekly timescale. The standard model simulation (black lines) reproduces
551 the observations at the sites reasonably well. Using a fixed value for CWC in the wet scavenging scheme (green lines)
552 significantly degrades the model performance. Comparisons between the standard and sensitivity simulations suggest
553 that AODs at LaRC and GSFC are mainly attributed to anthropogenic emissions. Contributions from BB emissions
554 are significant and may become comparable to anthropogenic contributions in some days. AODs at Tudor Hill are
555 mostly ascribed to marine (sea salt) emissions but are also affected by anthropogenic emissions, presumably from
556 North America. In summer, AERONET AODs at LaRC and GSFC indicate even larger day-to-day variations with
557 larger maximum AODs (~0.3-0.4) compared to winter (~0.2-0.3). The minimum AODs tend to decrease with time.



558 At Tudor Hill, AERONET AODs indicate high values (~0.2-0.3) in early and late Aug. (data not available for most
559 of Sep. at the time of this study). AERONET AODs at all three sites clearly identify two extremely large AOD events
560 close to Aug. 26 and Sep. 23; the western U.S. fire smoke associated with these events were also observed by aircraft
561 during ACTIVATE (section 5.4; Mardi et al., 2021; Corral et al., 2022). The standard model (black lines) reproduces
562 the decreasing trend of minimum AODs at LaRC and GSFC, but largely underestimates the magnitude of AODs at
563 LaRC with better performance at GSFC. The simulation “BB0-5.5km” (orange lines) where BB emissions are injected
564 between 0-5.5 km significantly improves the model’s capability of capturing the large AOD events, especially at
565 GSFC. Comparison between the standard and sensitivity model simulations suggest that while AODs are often
566 attributed to anthropogenic (and BB to a lesser extent) sources, BB emissions are mainly responsible for the large
567 AOD events on or around Aug. 26 and Sep. 23. For the Aug. 26 event, the large reduction in model AODs when BB
568 emissions are turned off indicates that the transport of the western U.S. fire smoke plumes to Tudor Hill is successfully
569 captured by the model. The model attributes the observed large AODs in early Aug. to long-range transport of dust
570 from northern Africa. However, most of the time AODs at Tudor Hill are mainly due to marine (sea salt) emissions.
571 The above analysis suggests that GEOS-Chem simulated AODs and their variability in the WNAO region are
572 reasonable.

573

574 **5.4 Model evaluation with aerosol extinction profiles from aircraft HSRL-2 lidar and CALIOP/CALIPSO** 575 **satellite retrievals**

576 The NASA LaRC HSRL-2 lidar instrument on the King Air aircraft measured aerosol extinction profiles in the
577 same vertical column as the Falcon in situ measurements in the BL in a coordinated manner, during 17 out of 17 and
578 17 out of 18 joint flights of the 2020 winter and summer campaigns, respectively. On the other hand, the CALIOP
579 instrument on CALIPSO satellite provides remote sensing measurements of aerosol extinction over the WNAO from
580 space, including three overpasses for which the two ACTIVATE aircraft performed under-flights during the 2020
581 summer campaign. In this section, we evaluate model simulated aerosol extinction profiles with HSRL-2 lidar and
582 CALIOP/CALIPSO satellite retrievals, characterize aerosol extinction vertical distribution, and examine potential
583 sources and processes responsible for aerosol extinction enhancements. Case studies of land-ocean horizontal gradient
584 of aerosol extinction, SNA and sea salt aerosol mixing, and long-range transport of the western U.S. fire smoke to the
585 ACTIVATE study domain in summer 2020, as observed by HSRL-2 and CALIOP, are also given.

586 **HSRL-2. Fig. 11** compares model simulated aerosol extinction profiles (550 nm, red lines) with aircraft HSRL-
587 2 lidar measurements (532 nm, black lines) averaged over 17 HSRL-2 flights during the 2020 winter and summer
588 campaigns, respectively. Also shown in the figure are results from model simulations with different injection heights
589 for BB emissions (**Table 1**). Hourly 3-D model output was sampled at the time and location of each HSRL-2
590 measurements from 17 (winter) and 17 (summer) flights, respectively. In winter, HSRL-2 observed high aerosol
591 extinction near the surface in the marine BL, which reflects North American BL outflow of aerosols to the WNAO
592 (section 4), and rapid decreases of aerosol extinction with increasing altitude. A layer of aerosol extinction
593 enhancement was observed at ~2.5 km altitude. The model largely overestimates extinction in the BL and
594 underestimates it in the free troposphere, resulting in a much sharper gradient between the BL and above (red line).



595 Note that on the other hand the model significantly underestimates monthly mean AOD relative to MODIS/Aqua
596 measurements in winter (**Fig. S3**). This discrepancy between HSRL-2 and MODIS measurements likely reflects the
597 sampling differences; for instance, many of the HSRL-2 flights occurred during cloudy conditions when MODIS
598 would not be able to measure AOD while HSRL-2 may still be able to measure aerosol extinction between gaps in
599 clouds. Increasing the injection height of BB emissions in the model improves the simulation of the vertical gradient
600 because of directly putting part of the emissions in the free troposphere. However, the model is not able to reproduce
601 the layer of aerosol extinction enhancement at ~ 2.5 km, suggesting vertical lifting is probably too weak in the model
602 in the wintertime. As shown below, this aerosol enhancement layer is also observed by CALIOP. In summer, the
603 standard model (red line) simulates the BL aerosol extinction reasonably well but fails to capture the large extinction
604 around 5 km as observed by HSRL-2. Increasing the injection height of BB emissions in the model to 0-5.5 km (green
605 line) or 2-10 km (blue line) results in much higher aerosol extinction at ~ 5 km, which is still lower than the mean
606 observed value by a factor of >2 . However, the latter is weighted towards the extremely high aerosol extinction at ~ 5
607 km observed by HSRL-2 on Sep. 15 and 22, 2020, which will be discussed later in **Fig. 17**.

608 **CALIOP. Fig. 12a** (left column) compares model simulated aerosol extinction (550 nm) vertical profiles with
609 CALIOP measurements (532 nm) averaged over the period of Feb. 14 – Mar. 12, 2020, and for four subdomains of
610 the WNAO, respectively: North (39° - 45° N, 72° - 62° W), Central (32° - 39° N, 78° - 68° W), and South (25° - 32° N, 82° -
611 72° W), as defined by Corral et al. (2020), and Bermuda (28° - 35° N, 69° - 59° W). For the North WNAO region, three
612 CALIOP data granules (2020-02-14T06-27-07ZN, 2020-03-03T06-21-54ZN, and 2020-03-04T17-37-24ZD) are
613 excluded due to cloud contamination. Examining aerosol extinction vertical profiles in the North and South WNAO
614 subdomains allows us to put the CALIOP observations in the Central WNAO, where all ACTIVATE 2020 research
615 flights occurred, in a context of latitudinal contrast. Model output averaged over 1-2 h LT and 13-14 h LT was sampled
616 at the date and location of nighttime and daytime CALIOP measurements, respectively. The right column shows the
617 model speciated aerosol extinction profiles corresponding to the sampled total aerosol extinction profile on the left
618 column. CALIOP observations show aerosols are mainly confined in the BL over the WNAO. In the Central WNAO,
619 the observed aerosol extinction reach a peak of ~ 0.05 km $^{-1}$ at ~ 0.5 - 1.0 km altitude, and exhibit layers of enhancements
620 in the free troposphere (e.g., ~ 2.5 km and ~ 4 - 6 km; note BL top < 1.6 km, **Fig. 2a**). The peak at ~ 2.5 km is consistent
621 with the HSRL-2 aerosol extinction enhancement at this altitude, as mentioned above (**Fig. 11**). The model captures
622 the decreasing trend of aerosol extinction with altitude but underestimates in the free troposphere where aerosol wet
623 scavenging is too fast in the standard model (section 5.2 and **Fig. 8**; this is also the case in the North WNAO
624 subdomain). Simulated speciated aerosol extinction values suggest sea salt contributes most to BL aerosol extinction
625 while SNA and OC contributions are comparable. In the North WNAO subdomain, CALIOP observed a similar
626 vertical gradient and the model suggests BL aerosol extinction are due to SNA aerosols more than OC and sea salt. In
627 the South WNAO subdomain, CALIOP observed the highest aerosol extinction of ~ 0.1 km $^{-1}$ (about 0.5 km above the
628 ocean surface) among the four subdomains. The model underestimates this peak by a factor of ~ 1.8 , simulates a weaker
629 vertical gradient, and attributes BL aerosol extinction mostly to sea salt. It suggests that the model sea salt emissions
630 are biased low and/or sea salt is removed too fast in the model. This is in line with results from comparisons with



631 MODIS AOD (**section S1, Fig. S3**). In the proximity of Bermuda, vertical aerosol extinction is more concentrated
632 towards the surface due to the dominant contribution from sea salt.

633 While summertime aerosols are mostly confined to the BL (top < 1 km), a larger fraction of the total AOD is
634 contributed by aerosols in the free troposphere compared to winter (Corral et al., 2020; **Fig. 12b**). This is evidenced
635 by layers of aerosol extinction enhancements, especially between ~3-8 km in the North WNAO subdomain. The
636 CALIOP aerosol extinction values between ~3-6 km in the Central WNAO are not as high as those from King Air
637 HSRL-2 measurements (right panel, **Fig. 11**), presumably because of the spatiotemporal mismatch between the
638 CALIPSO satellite overpass and King Air HSRL-2 sampling. The CALIOP-observed aerosol extinction peak (~0.08
639 km⁻¹) at ~0.5 km altitude in the Central WNAO is ~60% higher than in winter, consistent with the model result of
640 more sea salt in summer (**Fig. 12ab**; also see section 5.1). The standard model simulation with BB emissions injected
641 within the BL failed to capture the smoke aerosol extinction enhancements between ~3-8 km in the North WNAO;
642 using the 0-5.5 km injection heights clearly improves the simulation of smoke aerosol extinction, although the altitude
643 of the simulated smoke plume is somewhat lower than the observed plume height (bottom panels, **Fig. 12b**). Smoke
644 aerosol extinction is mainly contributed by organic aerosols, as suggested by the model. In contrast to winter, sea salt
645 aerosols make dominant contributions to the BL total aerosol extinction not only in the Central and South WNAO and
646 Bermuda but also in the North WNAO subdomain, which reflects the southwesterly transport of low-latitude marine
647 air along the WNAO as part of the Bermuda High in summer. SNA and OC contributions are also important in all
648 four subdomains while dust contributions are significant at lower latitudes, especially Bermuda.

649 **Land-Ocean aerosol extinction gradient.** We present a case where a large horizontal gradient of aerosol
650 extinction from the eastern U.S. coast going eastwards was observed by HSRL-2. **Fig. 13a** shows model simulated
651 hourly total aerosol extinction at ~1 km altitude over the WNAO during the King Air morning flight (14-17 UTC) on
652 March 12, 2020. Gray lines indicate the complete flight track with overlaid red lines denoting the flight tracks for
653 each hour. On the morning of March 12, King Air conducted a statistical survey flight as well as an ASTER/Terra
654 under-flight. It flew eastwards from LaRC and turned northeastward near the ZIBUT waypoint, followed by flying
655 back via ZIBUT after conducting an ASTER under-flight along ~69.7°W. The entire flight took about 3 hours (14:00-
656 17:00 UTC). **Fig. 13b** compares the time-height cross-section of aerosol extinction observed by the King Air HSRL-
657 2 lidar with those of model total and speciated aerosol extinction during the flight. **Fig. 14a** shows latitude-height
658 cross-section of aerosol extinction measured by CALIOP (532 nm) compared to that of model aerosol extinction (550
659 nm) over the WNAO at 7:08 UTC (3:08 am LT, about 7 hours before the King Air flight), Mar. 12, 2020. **Fig. 14b**
660 shows the corresponding curtain plots for model speciated aerosol extinction, as well as accumulated sea salt (SSA),
661 coarse-mode sea salt (SSc), RH, cloud fraction, and effective cloud extinction.

662 HSRL-2 observed very high aerosol extinction in the BL over land and off the coast with a decreasing trend
663 toward the marine region. The model captures this trend (**Fig. 13a**) but generally overestimates BL aerosol extinction
664 (**Fig. S5**). Despite HSRL-2 being unable to obtain meaningful retrievals in the BL for a large portion of the flight track
665 because of the interference of low-level clouds, the observed general pattern of BL aerosol extinction over land and
666 ocean is very similar to the model result (**Fig. 13b**). A thin layer of aerosol at 2-3 km seen by HSRL-2 is missing in
667 the standard model simulation. This is likely due to the low injection heights (within BL) of southeast U.S. BB



668 emissions in the model. GEOS-Chem speciated aerosol extinction suggest that SNA and OC are the main contributions
669 over land and off the coast with a similar magnitude of extinction (**Fig. 13b**). Over the ocean (~14:30-16:30 UTC),
670 SNA, OC, and SS all contribute to the thin aerosol layer close to sea surface with a slightly higher contribution from
671 SNA. The CALIPSO descending swath scanned the WNAO region about seven hours earlier and intersected almost
672 perpendicularly the flight track (**Fig. 14a**). However, the CALIOP retrieved only low aerosol extinction between 32-
673 40°N (note ~37°N is the King Air flight latitude at 14:00 UTC). This is because the CALIOP laser signal was largely
674 attenuated by the presence of optically thick clouds at these latitudes (**Fig. 14b**). Indeed, the corresponding model
675 results show high aerosol extinction in the BL along the CALIPSO orbit track. Model simulated speciated aerosol
676 extinction suggest SNA and OC contribute comparably to aerosol extinction at ~37°N while sea salt becomes more
677 important towards lower latitudes (**Fig. 14b**).

678 **SNA and sea salt mixing.** We present a case where SNA and sea salt aerosols are mixed as suggested by our
679 model analysis of HSRL-2 and CALIOP observations. **Fig. 15ab** presents plots similar to **Fig. 14ab** but for the King
680 Air flight on March 6, 2020, when the King Air conducted a statistical survey flight to the OXANA waypoint and
681 then to a southwest point (32.8°N, 75.2°W), and encountered a high aerosol layer in the marine BL (**Fig. 15a**). The
682 aircraft returned along the same flight track. HSRL-2 observed enhanced aerosol extinction in the lower troposphere
683 despite missing retrievals for most of the flight period (~18:00-22:00 UTC) due to attenuation by widespread marine
684 stratus clouds (GOES visible image, not shown). The model attributes the observed enhanced aerosol extinction in the
685 BL at ~20:00 UTC to sea salt mixed with SNA aerosols (**Fig. 15b**). The detachment of the SNA aerosol extinction
686 layer from the sea surface suggests its major source is U.S. continental anthropogenic emissions. GEOS-Chem also
687 simulates high aerosol extinction over the south WNAO region centered near the returning point of the flight.
688 CALIPSO overpassed the same region at the ascending node on the next day, Mar. 7 (**Fig. 16a**). CALIOP
689 measurements (532 nm) over the WNAO at 17:53 UTC that day show enhanced aerosol extinction in the lower
690 troposphere (< ~2.5 km) south of 39°N. The model reproduces this enhancement (**Fig. 16a**) and attributes it mainly to
691 coarse-mode sea salt (<32°N) and SNA (>32°N) (**Fig. 16b**). The latter is thus consistent with the model analysis of
692 HSRL-2 measurements on Mar. 6 (**Fig. 15b**). It is interesting to note that at < 35°N, especially lower latitudes, the
693 model simulates very high sea salt (mostly coarse-mode) aerosol extinction near the top of the marine BL where RH
694 and cloud extinction are high. This feature is typically seen over the WNAO in both CALIOP aerosol extinction
695 profiles and GEOS-Chem simulations. It suggests strong hygroscopic growth of sea salt particles and sea salt seeding
696 of marine BL clouds.

697 **Transport of the western U.S. fire smoke.** The above evaluation of model simulations with HSRL-2 and
698 CALIOP composite aerosol extinction observations in summer 2020 has suggested that using 0-5.5 km BB emission
699 injection heights significantly improves model performance in simulating the transport of the western U.S. fire smoke
700 plumes to the WNAO (**Fig. 11, Fig. 12b**). We present here model simulations of HSRL-2 aerosol extinction
701 measurements with large enhancements in the free troposphere from several individual flights to further demonstrate
702 the importance of BB emission injection heights with respect to the overall model performance. **Fig. 17** compares
703 time-height cross-sections of HSRL-2 lidar aerosol extinction (532 nm, left column) with those of model aerosol
704 extinction (550 nm, middle and right columns) for the flights of Aug. 26, Aug. 28, Sep. 15, and Sep. 22, respectively,



705 2020. Model results from the standard simulation (BB emissions injected into the BL) and the “BB0-5.5km”
706 simulation (BB emissions injected into 0-5.5 km) as listed in **Table 1** are shown. In the case of Aug. 26, the aerosol
707 plume at ~1.5-2 km altitude was missing in the standard simulation but captured by BB0-5.5km. In the case of Aug.
708 28, both simulations perform similarly and reproduce the aerosol extinction enhancements in the free troposphere.
709 Plumes with very high aerosol extinction were observed by HSRL-2 between 4-6 km on Sep. 15, and Sep. 22. While
710 the standard model failed to simulate these smoke plumes on both days, the BB0-5.5km simulation successfully
711 captures the transported smoke plumes albeit with much lower aerosol extinction.

712 We conduct a case study of long-range transport of the western U.S. fire smoke to the WNAO on Sep. 23, 2020,
713 which was captured by both CALIOP and under-flying ACTIVATE aircraft. **Fig. 18** shows time-height cross-section
714 of HSRL-2 aerosol extinction (532 nm) compared to that of model total (and speciated) aerosol extinction (550 nm)
715 for the King Air flight in the afternoon (~17-20 UTC) of that day. Also shown are the GOES-16 visible image (18:21
716 UTC; NASA Langley SATCORPS group) superimposed with King Air (red) and Falcon (yellow) flight tracks. HSRL-
717 2 observed a layer of very high aerosol extinction between 1.5-4.0 km during 17:00-18:00 UTC and another layer of
718 enhanced aerosol extinction between 1.5–3 km during ~18:30-20:00 UTC. The model simulated total aerosol
719 extinction shows a similar layer of aerosols (higher extinction between 17:00-18:30 UTC) during the entire flight, but
720 it is consistently thinner (between ~1.7-3.5 km) and located at a slightly lower altitude. Using the 0-5.5 km BB
721 emission injection heights does not correct this model bias (not shown). The model simulated speciated aerosol
722 extinction suggest that the dominant contribution to the high aerosol extinction layer is from OC with a small
723 contribution from SNA aerosols. The clear isolation above the marine BL indicates that the aerosols are very likely
724 from long-range transport in the free troposphere. Model results show a sea salt extinction component in the marine
725 BL between ~18:00-19:00 UTC as the aircraft was at the farthest location from the coast. Unfortunately, the HSRL-2
726 retrievals are not available for that time window due to cloud interference but do show some BL aerosols before and
727 after the data gap around 18:00 UTC.

728 In situ measurements from Falcon flying under King Air also show high CO (~200 ppbv) and aerosols (mostly
729 organics) between ~2-4 km during the flight on Sep. 23, 2020 (**Fig. S6**). Although the model failed to reproduce the
730 high CO concentrations in this layer (also see section 5.2), it simulates relatively weak CO enhancements due to BB
731 near the bottom (~2-3 km) of the observed layer. Similarly, the model puts the BB aerosol plume at an altitude about
732 1 km lower than that observed. Injecting BB emissions to higher altitudes has little effect on the simulated plume
733 altitude in this case. As observed, the simulated BB plume is mainly composed of organic aerosols.

734 Back trajectories were calculated to determine the origin of the aforementioned smoke plume. **Fig. 19ab** shows
735 the FLEXPART simulated upwind residence times for the air masses arriving at the location (latitude 36.87°N,
736 longitude 72.57°W, altitude ~3.5 km) at 17:13 UTC, Sep. 23, 2020. A major part of the air masses originated from the
737 BL of the western U.S. about 3-4 days upwind, where large fire events occurred during early and mid-September as
738 depicted by the QFED BB CO emission inventory (**Fig. 19c**). The trajectories in conjunction with surface weather
739 maps (**Fig. 19d**; https://www.wpc.ncep.noaa.gov/dailywxmap/index_20200920.html) suggest that the air masses
740 subsided to within the BL behind an eastward-moving cold front over mid-western states (~110°W-105°W) during



741 Sep. 19-20 before being lifted to the free troposphere during Sep. 20-21, followed by fast transport between 3.5-5 km
742 altitudes to the ACTIVATE domain.

743 While both ACTIVATE aircraft captured the smoke plume from the western U.S. fires, the satellite
744 measurements from CALIPSO can put it in a context of latitudinal extent. **Fig. 20** (left column) shows the curtain of
745 aerosol extinction measured by CALIOP over the WNAO at 17:45 UTC (1:45 pm LT), Sep. 23, 2020, in comparison
746 with model results from both the standard and BB0-5.5km simulations. Also shown (right column) is the comparison
747 corresponding to the CALIPSO nighttime overpass at 07:08 UTC (03:08 am LT) when the noise in the data is smaller
748 compared to daytime data. During daytime, CALIOP observed high aerosol extinction in the lower troposphere at 27-
749 33°N and 41-45°N, between 2.5-4.0 km altitudes at 35-37°N, and around 4.5 km altitude at 27-31°N. The altitude 2.5-
750 4.0 km of the aerosol plume at 35-37°N, where the CALIPSO under-flight occurred, is close to the plume altitude
751 ~1.5-4.0 km observed by HSRL-2 during 16:94-17:48 UTC (**Fig. 18b**). The standard model reasonably reproduces
752 the general pattern of aerosol extinction as a function of latitude and altitude, but underestimates it in the lower
753 troposphere around 43°N and misses aerosols observed at 4.5 km between 27-31°N. For the latter, the BB0-5.5km
754 simulation increases aerosol extinction but the simulated plume altitude is still ~ 1 km lower. The CALIOP nighttime
755 observations made about 10 hours earlier in close proximity show a more coherent pattern of the latitude-altitude
756 distribution, i.e., enhanced aerosol extinction in the BL between 25-43°N and distinct aerosol plumes in the free
757 troposphere (2.5-5.5 km, 35-43°N; 4-5 km, 27-33°N), with missing retrievals between 43-49°N. The model simulates
758 coherent aerosol plumes in the free troposphere at a wider latitude range (35-49°N), especially with the BB0-5.5km
759 simulation. BB0-5.5km suggests that the CALIOP observed plume at 4.5 km between 27-33°N is a southward
760 extension of the smoke plume at higher latitudes. The simulated aerosol plume is nevertheless at least 0.5 km lower
761 in altitude than that observed by CALIOP.

762 The weaker vertical transport of trace gases and aerosols in the model is likely a result of two model uncertainties:
763 remapping of meteorological data from the native cubed-sphere grid of the parent GEOS-5 GCM to an equally
764 rectilinear (latitude-longitude) grid, and degradation of the spatial and temporal resolutions of the input meteorological
765 data (Yu et al., 2018). Yu et al. (2018) showed that the remapping and the use of 3-hourly averaged wind archives
766 may lead to 5-20% error in the vertical transport of a surface-emitted tracer ²²²Rn in offline GEOS-Chem simulations
767 compared to online GEOS-5 simulations. It was attributed partly to the loss of organized vertical motions. Degrading
768 the spatial resolution of the meteorological data for input to GEOS-Chem (e.g., 2° × 2.5° used in this study) further
769 weakened vertical transport because organized vertical motions are averaged out at a coarser resolution. Such
770 inefficient vertical transport in coarse-resolution GEOS-Chem was also noted previously in the simulations of Asian
771 Tropopause Aerosol Layer (Fairlie et al., 2020) and upper-tropospheric ²²²Rn (Zhang et al., 2021), as constrained by
772 observations. Restoring the lost vertical transport by implementing the modified Relaxed Arakawa-Schubert
773 convection scheme in GEOS-Chem would alleviate this issue (He et al., 2019). On the other hand, the spatial resolution
774 for global models may be too coarse to resolve mean vertical motion that can be better resolved by regional models,
775 as illustrated by Fast et al. (2016) when simulating the observed aerosol layers transported from North America over
776 the Atlantic Ocean.

777



778 **6. Source attributions of AODs over the WNAO during ACTIVATE**

779 In this section, we quantify the contributions of different emission types to the AODs over the eastern U.S. and
780 WNAO during ACTIVATE in the model. **Fig. 21** shows the absolute and percentage changes in the average AODs
781 for the periods of the 2020 winter (Feb.14-Mar.12) and summer (Aug.13-Sep.30) campaigns, respectively, when
782 anthropogenic (including biofuel), BB, biogenic, marine, and dust emissions are separately turned off in the model.
783 In winter, anthropogenic emissions make dominant contributions (70-90%) over land between 36-48°N, 30-60% in
784 the N box region, 20-40% in the S box region, with a decreasing contribution trend from NW to SE. At Bermuda,
785 about 20% of AOD is due to anthropogenic emissions. BB emissions make the largest contributions (up to 40-50%)
786 in southeastern U.S. coast and contribute about 10-30% of AODs in the N+S box regions. Marine emissions (mainly
787 sea salt) contribute 30-60% over most of the N+S box regions, with an increasing contribution trend from NW to SE,
788 which is opposite of the trend of anthropogenic emission contributions. Biogenic and dust emissions make only small
789 contributions to AODs throughout the domain. In summer, anthropogenic emission contributions are reduced over
790 both land and WNAO compared to winter, with 20-30% contribution in the N+S box regions. By contrast, BB emission
791 contributions increase substantially over land and WNAO relative to winter, reflecting the influences of the western
792 U.S. fire smoke as well as BB emissions from the southeast U.S. during summer. Interestingly, there is an apparent
793 pathway for transport of smoke plumes towards Bermuda (left second row, **Fig. 21b**) as also demonstrated in recent
794 work (Aldhaif et al., 2021; Mardi et al., 2021); this is consistent with the smoke AOD events observed by AERONET
795 at Tudor Hill, Bermuda (section 5.3). At Bermuda, BB emissions contribute more to AOD than anthropogenic
796 emissions in summer (~20% vs. ~15%). Biogenic emission contributions (10-20%) are mostly confined in the
797 southeast U.S. Marine emission contributions to AOD in the N+S box regions and around Bermuda are significantly
798 higher compared to winter (left fourth row, **Fig. 21b**), despite higher marine emission contributions south of 30°N in
799 winter. African dust contributions to AOD (>10%) are seen mainly to the south of Bermuda but extend as far as Florida
800 and the Gulf of Mexico.

801

802 **7. Summary and conclusions**

803 We have simulated tropospheric aerosols over the western North Atlantic Ocean (WNAO) during the winter
804 (Feb. 14 - Mar. 12) and summer (Aug. 13 - Sep. 30) campaigns of the NASA Earth-Venture Suborbital-3 ACTIVATE
805 2020 mission (Sorooshian et al., 2019, 2023) using the GEOS-Chem global chemical transport model driven by the
806 MERRA-2 assimilated meteorology (at 2°×2.5° horizontal resolution). Model results are evaluated with measurements
807 from two aircraft, the low-flying HU-25 Falcon and high-flying King Air, as well as ground-based and satellite
808 observations. Our objective is to characterize and improve understanding of the aerosol life cycle, transport, and
809 distribution over the WNAO during the two campaigns. Major work and results are summarized below.

810 1) Contrasting atmospheric circulation patterns and meteorological conditions were prevalent during Feb.-Mar.
811 and Aug.-Sep. ACTIVATE 2020. In winter, the flights took place in a recurring location for the passages of cold fronts
812 driven by the Northern Hemisphere mid-latitude cyclones and sampled the North American continental outflow
813 extensively. Flights to the north often occurred during post-frontal conditions to sample and study MBL clouds,
814 especially during cold air outbreaks. The southern flight region experienced stronger uplifting and precipitation



815 scavenging. In summer, the strengthened Bermuda High extended westward with southwesterly winds offshore along
816 the U.S. SE coast (~32-36°N) and easterly in the subtropics (<30°N). Compared to winter, the horizontal gradients in
817 surface temperature, RH, vertical pressure velocity, precipitation, and PBL height were much weaker, and convective
818 precipitation was much stronger in the flight domain.

819 2) Transport in the BL behind cold fronts is a major mechanism for the North American pollution outflow to the
820 WNAO. The winter campaign encountered about four major periods with cold fronts passing through the study area,
821 during which continental pollution (e.g., CO) was swept in the BL southeastward to the ACTIVATE flight latitudes
822 (32.4-39.8°N). In summer, intrusion of cold air deep into the flight domain did not occur until late September since
823 midlatitude cyclones were shifted northward.

824 3) Major pathways for vertical transport of trace gases and aerosols over the North American continental outflow
825 region include uplifting ahead of cold fronts, convective transport, and BL turbulent mixing. In winter, large-scale
826 vertical transport ahead of cold fronts was the dominant process responsible for lifting CO out of the BL over the U.S.
827 East Coast and the flight domain, followed by rapid eastward transport in the free troposphere. Convection was also
828 important, especially in the southern flight area, but became even more important in summer. By contrast, BL turbulent
829 mixing was found to be the dominant process responsible for the upward transport of sea salt within and ventilation
830 out of the BL over the flight domain in winter, while both convection and turbulent mixing were important in uplifting
831 sea salt to the free troposphere in summer.

832 4) We characterized the model simulated aerosol species with respect to their distributions, mass loadings, and
833 optical depths (AODs) over the WNAO. In winter, the horizontal distributions of SNA, BC, POA, and SOA
834 concentrations in the BL largely reflected the frequent transport of continental pollution behind cold fronts. Sea salt
835 had the largest mass among aerosols over the WNAO, with maximum in the easterly trade wind region and to the east
836 of the northern flight domain. BC, SOA, and dust abundances across the flight domain were relatively small. In
837 summer, BL sulfate concentrations were significantly higher, resulting from stronger production from oxidation of
838 SO₂. BL nitrate concentrations decreased substantially due to the volatility of ammonium nitrate at higher temperature
839 and more sulfate competing with nitrate for ammonium. Substantially higher SOA concentrations reflect the large
840 production from strong oxidation of VOCs. The vertical extent of the major North American continental outflow
841 aerosols was significantly higher because of the impact of convective lifting. BL sea salt abundance increased in
842 summer over the WNAO, especially from the ACTIVATE flight areas to Bermuda, because of stronger winds. Dust
843 amounts also significantly increased due to long-range transport of dust emissions from North Africa. In both seasons,
844 sea salt, OA, and SNA were the main contributors to the mean total AOD in the flight areas. The strong hygroscopic
845 growth of fine aerosols results in a much larger fraction of AOD (versus aerosol mass) from SNA (or OA).

846 5) We evaluated model simulated vertical profiles of CO, SNA, and OA concentrations with Falcon aircraft
847 AMS measurements and performed sensitivity experiments to quantify their sources. In winter, outflow of pollution
848 from continental sources dominated the lower troposphere, causing a sharp vertical gradient in CO, SNA, and OA
849 concentrations at ~1.0 km altitude; in summer, impacts of convection and BB sources increased and those gradients
850 were weaker. Extending the BB emission injection height from within the BL to 0-5.5 km largely improved or
851 corrected the model low biases in simulated aerosol enhancements in the free troposphere during the summer



852 campaign. SNA aerosols are predominantly from continental anthropogenic emissions, but summertime BB
853 contributions are also important between ~3-6 km. OA in the free troposphere are mainly from BB whereas those in
854 the marine BL have sources from BB, anthropogenic, and marine emissions.

855 6) Intensive aerosol profile measurements from ACTIVATE 2020 provide useful constraints on model aerosol
856 scavenging due to stratiform precipitation. Uncertainty in CWC used in GEOS-Chem has a large impact on the
857 simulated tropospheric aerosols over the ACTIVATE study domain. Using the MERRA-2's spatiotemporally varying
858 CWC (versus a fixed value) improves model simulations of BL aerosol (especially sulfate) concentrations and
859 AERONET AODs in the domain in winter. However, this approach leads to too fast scavenging in the free troposphere.
860 The model also had some difficulties in reproducing the surface aerosol concentration and deposition flux
861 measurements in the eastern U.S. coastal region as well as AOD retrievals from MODIS/Aqua satellite measurements
862 over the WNAO. Fully implementing the revised wet scavenging scheme of Luo et al. (2020) in the model could
863 improve the model performance.

864 7) We evaluated model simulated aerosol extinction (at 550 nm) profiles with King Air HSRL-2 lidar and
865 CALIOP/CALIPSO satellite retrievals (at 532 nm) during the two campaigns. In winter, HSRL-2 observed high
866 aerosol extinction in the marine BL associated with the North American continental outflow. A layer of aerosol
867 extinction enhancements was observed at ~2.5 km altitude. The model simulates a much sharper gradient compared
868 to HSRL-2 between the BL and free troposphere, suggesting the vertical lifting is probably too weak in the model. In
869 summer, HSRL-2 observed much higher aerosol extinction in the BL and large extinction enhancements around 5.0
870 km altitude. The standard model fails to capture the latter but can be improved by using higher BB emission injection
871 heights.

872 8) In winter, the CALIOP aerosol extinction over the central WNAO reached a peak at ~0.5-1.0 km altitude and
873 showed layers of enhancements in the free troposphere (e.g., the peak at ~2.5 km altitude also observed by HSRL-2).
874 The model captures the vertical trend of aerosol extinction but underestimates extinction in the free troposphere largely
875 due to too fast scavenging. SNA aerosols contribute the most in the BL over the North WNAO while sea salt
876 predominates over the southern WNAO. For the latter, the model substantially underestimates aerosol extinction in
877 the lower BL, suggesting too low sea salt emissions or too fast removal. In summer, free tropospheric aerosols
878 contribute a larger fraction of AOD relative to winter (Corral et al., 2020). The significantly higher extinction peak
879 observed in the BL over the central WNAO compared to winter is consistent with simulated higher sea salt in summer.
880 Injecting BB emissions between 0-5.5 km altitudes apparently improves the simulation of smoke aerosol extinction,
881 especially in the northern WNAO subdomain. A feature typically seen over the WNAO (< 35°N) as suggested by
882 CALIOP aerosol extinction profiles and GEOS-Chem simulations is very high sea salt (mostly coarse-mode) aerosol
883 extinction near the top of the marine BL where RH and cloud extinction are high. The latter suggests strong
884 hygroscopic growth of sea salt particles and sea salt seeding of marine stratus clouds.

885 9) We conducted a case study of long-range transport of the western U.S. fire smoke to the WNAO on Sep. 23,
886 2020, which was captured by both CALIOP and the under-flying ACTIVATE aircraft. The CALIPSO measurements
887 allowed us to put this smoke transport event in a context of latitudinal extent. Model simulations of HSRL-2 aerosol
888 extinction measurements with large enhancements in the free troposphere from several individual flights (Aug. 26,



889 Aug. 28, Sep. 15, and Sep. 22, 2020) demonstrate that injecting BB emissions into 0-5.5 km altitudes often improves
890 the model performance. Case studies also show that the model reasonably captures the continental outflow of aerosols,
891 land-ocean aerosol extinction gradient, and mixing of anthropogenic aerosols with sea salt.

892 10) We quantified the contributions of different emission types (anthropogenic, BB, biogenic, marine, dust) to
893 the AOD over the eastern U.S. and WNAO in the model. In winter, anthropogenic emission contributions dominate
894 near the coast and decrease southeastward. BB emissions contribute most to AOD in southeastern U.S. coast and
895 account for ~10-30% of AOD in the flight area, while marine emissions contribute 30-60% over most of the flight
896 area southeastward. In summer, anthropogenic emission contributions to AOD are reduced but BB emission
897 contributions increase substantially. An apparent pathway for transport of smoke plumes towards Bermuda is
898 identified (Aldhaif et al., 2021; Mardi et al., 2021) and is consistent with the smoke AOD events observed by
899 AERONET at Tudor Hill, Bermuda. BB emissions contribute more to AOD at Bermuda than anthropogenic emissions
900 in summer (~20% vs. ~15%). Biogenic emission contributions (10-20%) are mostly confined in the southeast U.S.
901 Marine emission contributions to AOD in the flight area and around Bermuda are significantly higher relative to
902 winter. African dust contributions to AOD (>10%) are seen mainly to the south of Bermuda but extend as far as Florida
903 and the Gulf of Mexico.

904 The above results on aerosol lifecycle, transport, and distribution have important implications for studies of
905 aerosol-cloud-meteorology interaction during ACTIVATE 2020. For instance, transport of continental aerosols over
906 the WNAO may modulate cloud microphysics and precipitation. Recently, Painemal et al. (2023) analyzed wintertime
907 BL cloud synoptic variability over the WNAO and linked the occurrence of a maximum in cloud droplet number
908 concentration with continental aerosols during cold air outbreaks. Correctly representing aerosol distribution and
909 variability is thus critical in simulating aerosol indirect effects on clouds. Biomass burning aerosols can affect the
910 whole troposphere and interact with clouds directly or indirectly, as suggested by a case study of smoke transport from
911 the western U.S. during ACTIVATE on Aug. 26, 2020 (Mardi et al., 2021). Mardi et al. also associated BB days with
912 higher cloud drop number concentrations and lower drop effective radius. Our work implies that using reasonable BB
913 emission injection heights in global models, among other factors, plays an essential role in representing smoke-cloud
914 interactions. The high coarse-mode sea salt aerosol extinction along with high RH and cloud extinction near the top
915 of the marine BL over the WNAO (< 35°N), as identified in this work, suggests a potential ideal region for studying
916 giant CCN – cloud interactions (Gonzalez et al., 2022).

917 This study highlights the following areas for recommended future work to improve the modeling and
918 understanding of tropospheric aerosol life cycle, transport, and distribution over the WNAO. An evaluation of the
919 MERRA-2 CWC, including its partition between liquid and ice water in the vertical column, with available aircraft
920 and satellite observations is required for a better representation of aerosol scavenging in GEOS-Chem. The liquid-ice
921 partitioning affects the scavenging efficiencies of aerosols due to both warm and ice clouds. Accurate BB emission
922 injection heights derived from daily or hourly observations from space (e.g., from the TEMPO geostationary satellite)
923 are expected to significantly enhance the model's capability to simulate smoke aerosols and their vertical distribution
924 over North America and the WNAO. Furthermore, efforts to improve parameterizations of sea salt emissions for use



925 in global models should be encouraged. Inefficient vertical transport in coarse-resolution models may also be
926 improved by using high-resolution and/or regional models.

927

928 *Data availability.* Observational data for model evaluation are introduced in Section 3. All data from the Falcon and
929 King Air are publicly archived on NASA Atmospheric Science Data Center (ASDC)'s Distributed Active Archive
930 Center (DAAC) and accessible at <https://doi.org/10.5067/SUBORBITAL/ACTIVATE/DATA001>. GEOS-Chem code
931 v11-01 used in this work is available at <https://zenodo.org/records/10982278> (Liu and Zhang, 2024).

932

933 *Supplement.* The supplement related to this article is available online at: <https://doi.org/XX.XXX/XXX-supplement>
934 (TBD).

935

936 *Competing interests.* At least one of the (co-)authors is a member of the editorial board of Atmospheric Chemistry
937 and Physics.

938

939 *Author contributions.* Conceptualization: HL, BZ, RM, and AS. Model simulation: HL and BZ. Analysis and initial
940 draft preparation: HL and BZ with contributions from HC. Data collection: RM, LZ, RF, AS, MS, AJS, JH, EC, MF,
941 TS, CH, GD, JN, JD, and YC. CALIOP data analysis: HC, JT, and MV. Manuscript review, comments, and editing:
942 all authors. Model modification and improvement: HL, BZ, GL, FY, CK, and MJ.

943

944 *Acknowledgements.* The work was funded by ACTIVATE, a NASA Earth Venture Suborbital-3 (EVS-3) investigation
945 funded by NASA's Earth Science Division and managed through the Earth System Science Pathfinder Program Office.
946 HL and BZ acknowledge the partial support of the NASA EVS-2 NAAMES mission for model development. The
947 GEOS-Chem model is managed by the Atmospheric Chemistry Modeling Group at Harvard University with support
948 from NASA ACPMAP and MAP programs. The GEOS-Chem support team at Harvard University and Washington
949 University at Saint Louis (WashU) is acknowledged for their effort. GEOS-Chem input files were obtained from the
950 GEOS-Chem Data Portal enabled by WashU with assistance from Andrew Schuh of Colorado State University. HL
951 would like to thank Brett Gantt (EPA) for assisting with producing the MODIS/Aqua chlorophyll-*a* data, Lee Murray
952 (University of Rochester) for providing the lightning NO_x emission file for use with GEOS-Chem, and Robert Levy
953 (NASA) for helpful discussions on the use of MODIS aerosol data. NASA Center for Climate Simulation (NCCS)
954 provided supercomputing resources. PIs and staff for the three AERONET sites are acknowledged for their effort. The
955 Pacific Northwest National Laboratory (PNNL) is operated for DOE by Battelle Memorial Institute under contract
956 DE-AC05-76RLO1830.

957

958 *Financial support.* This research was supported by NASA grant 80NSSC19K0389 in support of the ACTIVATE
959 mission.

960

961



962 **References**

963

- 964 Aldhaif, A. M., Lopez, D. H., Dadashazar, H., and Sorooshian, A.: Sources, frequency, and chemical nature of dust
965 events impacting the United States East Coast, *Atmospheric Environment*, 231, 117456,
966 <https://doi.org/10.1016/j.atmosenv.2020.117456>, 2020.
- 967 Aldhaif, A. M., Lopez, D. H., Dadashazar, H., Painemal, D., Peters, A. J., and Sorooshian, A.: An aerosol climatology
968 and implications for clouds at a remote marine site: Case study over Bermuda. *J. Geophys. Res.-Atmos.*, 126,
969 e2020JD034038. <https://doi.org/10.1029/2020JD034038>, 2021.
- 970 Alexander, B., Park, R. J., Jacob, D. J., Li, Q. B., Yantosca, R. M., Savarino, J., Lee, C. C. W., and Thiemens, M.
971 H., Sulfate formation in sea-salt aerosols: Constraints from oxygen isotopes, *J. Geophys. Res.*, 110, D10307, 2005.
- 972 Appel, K. W., Foley, K. M., Bash, J. O., Pinder, R. W., Dennis, R. L., Allen, D. J., and Pickering, K.: A multi-
973 resolution assessment of the Community Multiscale Air Quality (CMAQ) model v4.7 wet deposition estimates for
974 2002–2006, *Geosci. Model Dev.*, 4, 357–371, <https://doi.org/10.5194/gmd-4-357-2011>, 2011.
- 975 Berg, L. K., et al.: The Two-Column Aerosol Project: Phase I—Overview and impact of elevated aerosol layers on
976 aerosol optical depth, *J. Geophys. Res. Atmos.*, 121, 336–361, doi:10.1002/2015JD023848, 2016.
- 977 Bosilovich MG, and Coauthors: MERRA-2: Initial Evaluation of the Climate. NASA/TM2015104606, Vol. 43, 139
978 pp. <https://gmao.gsfc.nasa.gov/pubs/docs/Bosilovich803.pdf>, 2015.
- 979 Bosilovich, M., Robertson, F., Takacs, L., Molod, A., and Mocko, D.: Atmospheric water balance and variability in
980 the MERRA-2 reanalysis. *J. Climate*, 30, 1177–1196, doi: 10.1175/JCLI-D-16-0338.1, 2017.
- 981 Boucher, O., D. Randall, P. Artaxo, C. Bretherton, G. Feingold, P. Forster, V.-M. Kerminen, Y. Kondo, H. Liao, U.
982 Lohmann, P. Rasch, S.K. Satheesh, S. Sherwood, B. Stevens and X.Y. Zhang: Clouds and Aerosols. In: *Climate*
983 *Change 2013: The Physical Science Basis. Contribution of Working Group I to the Fifth Assessment Report of the*
984 *Intergovernmental Panel on Climate Change [Stocker, T.F., D. Qin, G.-K. Plattner, M. Tignor, S.K. Allen, J.*
985 *Boschung, A. Nauels, Y. Xia, V. Bex and P.M. Midgley (eds.)]. Cambridge University Press, Cambridge, United*
986 *Kingdom and New York, NY, USA, 2013.*
- 987 Breider, T.J., L.J. Mickley, D.J. Jacob, C. Ge, J. Wang, M.P. Sulprizio, B. Croft, D.A. Ridley, J.R. McConnell, S.
988 Sharma, L. Husain, V.A. Dutkiewicz, K. Eleftheriadis, H. Skov, and P.K. Hopke, Multi-decadal trends in aerosol
989 radiative forcing over the Arctic: contribution of changes in anthropogenic aerosol to Arctic warming since 1980, *J.*
990 *Geophys. Res.*, 122(6), 3573–3594, doi:10.1002/2016JD025321, 2017.
- 991 Burton, S. P., Hostetler, C. A., Cook, A. L., Hair, J. W., Seaman, S. T., Scola, S., et al.: Calibration of a high spectral
992 resolution Lidar using a Michelson Interferometer, with data examples from Oracles. *Applied Optics*, 57(21),
993 6061–6075. <https://doi.org/10.1364/Ao.57.006061>, 2018.
- 994 Carlson, T. N.: *Mid-Latitude Weather Systems*. Am. Meteorol. Soc., Boston, MA, 1998.
- 995 Carr, J.L., D.L. Wu, J. Daniels, M.D. Friberg, W. Bresky, and H. Madani: GEO–GEO Stereo-Tracking of Atmospheric
996 Motion Vectors (AMVs) from the Geostationary Ring, *Remote Sens.*, 12, 3779; doi:10.3390/rs12223779, 2020.



- 997 Chen, J., Wang, H., Li, X., Painemal, D., Sorooshian, A., Lee Thornhill, K., Robinson, C., and Shingler, T.: Impact
998 of Meteorological Factors on the Mesoscale Morphology of Cloud Streets during a Cold Air Outbreak over the
999 Western North Atlantic, *Journal of the Atmospheric Sciences*, 10.1175/jas-d-22-0034.1, 2022.
- 1000 Chen, L. Q., and Duce, R. A.: The sources of sulfate, vanadium and mineral matter in aerosol-particles over Bermuda.
1001 *Atmospheric Environment*, 17(10), 2055–2064, 1983.
- 1002 Christoudias, T., Pozzer, A., and Lelieveld, J.: Influence of the North Atlantic Oscillation on air pollution transport.
1003 *Atmospheric Chemistry and Physics*, 12(2), 869–877. <https://doi.org/10.5194/acp-12-869-2012>, 2012.
- 1004 Coen, C., M., Andrews, E., Alastuey, A., Arsov, T. P., Backman, J., Brem, B. T., Bukowiecki, N., Couret, C.,
1005 Eleftheriadis, K., Flentje, H., Fiebig, M., Gysel-Beer, M., Hand, J. L., Hoffer, A., Hooda, R., Hueglin, C., Joubert,
1006 W., Keywood, M., Kim, J. E., Kim, S.-W., Labuschagne, C., Lin, N.-H., Lin, Y., Lund Myhre, C., Luoma, K.,
1007 Lyamani, H., Marinoni, A., Mayol-Bracero, O. L., Mihalopoulos, N., Pandolfi, M., Prats, N., Prenni, A. J., Putaud,
1008 J.-P., Ries, L., Reisen, F., Sellegri, K., Sharma, S., Sheridan, P., Sherman, J. P., Sun, J., Titos, G., Torres, E., Tuch,
1009 T., Weller, R., Wiedensohler, A., Zieger, P., and Laj, P.: Multidecadal trend analysis of in situ aerosol radiative
1010 properties around the world, *Atmos. Chem. Phys.*, 20, 8867–8908, <https://doi.org/10.5194/acp-20-8867-2020>,
1011 2020.
- 1012 Cooper, O. R., Moody, J. L., Parrish, D. D., Trainer, M., Holloway, J. S., Hubler, G., et al.: Trace gas composition of
1013 midlatitude cyclones over the Western North Atlantic Ocean: A seasonal comparison of O₃ and CO. *Journal of*
1014 *Geophysical Research*, 107(D7-8), 4057. <https://doi.org/10.1029/2001JD000902>, 2002.
- 1015 Colarco, P. R., et al.: Saharan dust transport to the Caribbean during PRIDE: 2. Transport, vertical profiles, and
1016 deposition in simulations of in situ and remote sensing observations, *J. Geophys. Res.*, 108(D19), 8590,
1017 doi:10.1029/2002JD002659, 2003.
- 1018 Corral, A. F., Choi, Y., Crosbie, E., Dadashazar, H., DiGangi, J. P., Diskin, G. S., Fenn, M., Harper, D. B., Kirschler,
1019 S., Liu, H., Moore, R. H., Nowak, J. B., Scarino, A. J., Seaman, S., Shingler, T., Shook, M. A., Thornhill, K. L.,
1020 Voigt, C., Zhang, B., Ziemba, L. D., and Sorooshian, A.: Cold Air Outbreaks Promote New Particle Formation
1021 Off the U.S. East Coast, *Geophysical Research Letters*, 49, e2021GL096073,
1022 <https://doi.org/10.1029/2021GL096073>, 2022.
- 1023 Corral, A. F., Dadashazar, H., Stahl, C., Edwards, E.-L., Zuidema, P., and Sorooshian, A.: Source Apportionment of
1024 Aerosol at a Coastal Site and Relationships with Precipitation Chemistry: A Case Study over the Southeast United
1025 States, *Atmosphere*, 11, 1212, <https://doi.org/10.3390/atmos11111212>, 2020.
- 1026 Corral, A. F., Braun, R. A., Cairns, B., Goroooh, V. A., Liu, H., Ma, L., et al.: An overview of atmospheric features
1027 over the Western North Atlantic Ocean and North American East Coast – Part 1: Analysis of aerosols, gases, and
1028 wet deposition chemistry. *Journal of Geophysical Research: Atmospheres*, 126, e2020JD032592.
1029 <https://doi.org/10.1029/2020JD032592>, 2021.
- 1030 Creilson, J. K., Fishman, J., and Wozniak, A. E.: Intercontinental transport of tropospheric ozone: A Study of its
1031 seasonal variability across the North Atlantic utilizing tropospheric ozone residuals and its relationship to the North
1032 Atlantic Oscillation. *Atmospheric Chemistry and Physics*, 3, 2053–2066, 2003.



- 1033 Croft, B., Martin, R. V., Moore, R. H., Ziemba, L. D., Crosbie, E. C., Liu, H., Russell, L. M., Saliba, G., Wisthaler,
1034 A., Müller, M., Schiller, A., Galí, M., Chang, R. Y.-W., McDuffie, E. E., Bilsback, K. R., and Pierce, J. R.: Factors
1035 controlling marine aerosol size distributions and their climate effects over the northwest Atlantic Ocean region,
1036 *Atmos. Chem. Phys.*, 21, 1889–1916, <https://doi.org/10.5194/acp-21-1889-2021>, 2021.
- 1037 Dadashazar, H., Painemal, D., Alipanah, M., Brunke, M., Chellappan, S., Corral, A. F., Crosbie, E., Kirschler, S., Liu,
1038 H., Moore, R. H., Robinson, C., Scarino, A. J., Shook, M., Sinclair, K., Thornhill, K. L., Voigt, C., Wang, H.,
1039 Winstead, E., Zeng, X., Ziemba, L., Zuidema, P., and Sorooshian, A.: Cloud drop number concentrations over the
1040 western North Atlantic Ocean: seasonal cycle, aerosol interrelationships, and other influential factors, *Atmos.*
1041 *Chem. Phys.*, 21, 10499–10526, <https://doi.org/10.5194/acp-21-10499-2021>, 2021.
- 1042 Dadashazar, H., Corral, A. F., Crosbie, E., Dmitrovic, S., Kirschler, S., McCauley, K., Moore, R., Robinson, C.,
1043 Schlosser, J. S., Shook, M., Thornhill, K. L., Voigt, C., Winstead, E., Ziemba, L., and Sorooshian, A.: Organic
1044 enrichment in droplet residual particles relative to out of cloud over the northwestern Atlantic: analysis of airborne
1045 ACTIVATE data, *Atmos. Chem. Phys.*, 22, 13897–13913, <https://doi.org/10.5194/acp-22-13897-2022>, 2022.
- 1046 Darmenov, A. and da Silva, A.: The Quick Fire Emissions Dataset (QFED): Documentation of versions 2.1, 2.2 and
1047 2.4, NASA Technical Report Series on Global Modeling and Data Assimilation NASA TM-2015-104606, Volume
1048 38, <http://gmao.gsfc.nasa.gov/pubs/docs/Darmenov796.pdf>, 2015.
- 1049 Davis, R. E., Hayden, B. P., Gay, D. A., Phillips, W. L., and Jones, G. V.: The North Atlantic Subtropical Anticyclone.
1050 *Journal of Climate*, 10(4), 728–744. [https://doi.org/10.1175/1520-0442\(1997\)010<0728:tnasa>2.0.co;2](https://doi.org/10.1175/1520-0442(1997)010<0728:tnasa>2.0.co;2), 1997.
- 1051 de Leeuw, G., Andreas, E. L., Anguelova, M. D., Fairall, C. W., Lewis, E. R., O'Dowd, C., et al.: Production Flux of
1052 Sea Spray Aerosol. *Reviews of Geophysics*, 49(2), RG2001. <https://doi.org/10.1029/2010rg000349>, 2011.
- 1053 DeBell, L. J., Vozzella, M., Talbot, R. W., and Dibb, J. E.: Asian dust storm events of spring 2001 and associated
1054 pollutants observed in New England by the Atmospheric Investigation, Regional Modeling, Analysis and
1055 Prediction (AIRMAP) monitoring network, *J. Geophys. Res.*, 109, D01304, doi:10.1029/2003JD003733, 2004.
- 1056 DeCarlo, P. F., Dunlea, E. J., Kimmel, J. R., Aiken, A. C., Sueper, D., Crouse, J., Wennberg, P. O., Emmons, L.,
1057 Shinozuka, Y., Clarke, A., Zhou, J., Tomlinson, J., Collins, D. R., Knapp, D., Weinheimer, A. J., Montzka, D. D.,
1058 Campos, T., and Jimenez, J. L.: Fast airborne aerosol size and chemistry measurements above Mexico City and
1059 Central Mexico during the MILAGRO campaign, *Atmos. Chem. Phys.*, 8, 4027–4048, [10.5194/acp-8-4027-2008](https://doi.org/10.5194/acp-8-4027-2008),
1060 2008.
- 1061 Del Genio, A. D., Yao, M. S., Kovari, W., and Lo, K. K.W.: A prognostic cloud water parameterization for global
1062 climate models, *J. Climate.*, 9, 270–304, 1996.
- 1063 Dickerson, R. R., et al.: Thunderstorms - An important mechanism in the transport of air pollutants, *Science*, 235,
1064 460–464, 1987.
- 1065 DiGangi, J. P., Y. Choi, J. B. Nowak, H. S. Halliday, G. S. Diskin, S. Feng, . . . K. J. Davis (2021), Seasonal Variability
1066 in Local Carbon Dioxide Combustion Sources over the Central and Eastern US using Airborne In-Situ
1067 Enhancement Ratios, *Earth and Space Science Open Archive ESSOAr*.
- 1068 DiGangi, J. P., Choi, Y., Nowak, J. B., Halliday, H. S., Diskin, G. S., Feng, S., et al.: Seasonal variability in local
1069 carbon dioxide biomass burning sources over central and eastern US using airborne in situ enhancement ratios.



- 1070 Journal of Geophysical Research: Atmospheres, 126, e2020JD034525. <https://doi.org/10.1029/2020JD034525>,
- 1071 2021.
- 1072 Drury, E., D. J. Jacob, R. J. D. Spurr, J. Wang, Y. Shinozuka, B. E. Anderson, A. D. Clarke, J. Dibb, C. McNaughton,
- 1073 and R. Weber: Synthesis of satellite (MODIS), aircraft (ICARTT), and surface (IMPROVE, EPA-AQS,
- 1074 AERONET) aerosol observations over eastern North America to improve MODIS aerosol retrievals and constrain
- 1075 surface aerosol concentrations and sources, *J. Geophys. Res.*, 115, D14204, doi:10.1029/2009JD012629, 2010.
- 1076 Dubovik, O., Smirnov, A., Holben, B. N., King, M. D., Kaufman, Y. J., Eck, T. F., and Slutsker, I.: Accuracy
- 1077 assessments of aerosol optical properties retrieved from Aerosol Robotic Network (AERONET) Sun and sky
- 1078 radiance measurements, *J. Geophys. Res.*, 105(D8), 9791–9806, doi:10.1029/2000JD900040, 2000.
- 1079 Eastham, S. D., Weisenstein, D. K., and Barrett, S. R. H.: Development and evaluation of the unified tropospheric-
- 1080 stratospheric chemistry extension (UCX) for the global chemistry-transport model GEOS-Chem, *Atmos. Env.*, 89,
- 1081 2014.
- 1082 Edwards, E.-L., Corral, A.F., Dadashazar, H., Barkley, A.E., Gaston, C.J., Zuidema, P., and Sorooshian, A.: Impact
- 1083 of various air mass types on cloud condensation nuclei concentrations along coastal southeast Florida, *Atmospheric*
- 1084 *Environment*, <https://doi.org/10.1016/j.atmosenv.2021.118371>, 2021.
- 1085 Fairlie, T. D., Jacob, D. J., and Park, R. J.: The impact of transpacific transport of mineral dust in the United
- 1086 States, *Atmos. Environ.*, 1251-1266, 2007.
- 1087 Fairlie, T. D., Liu, H., Vernier, J.-P., Campuzano-Jost, P., Jimenez, J. L., Jo, D. S., et al.: Estimates of regional source
- 1088 contributions to the Asian Tropopause Aerosol Layer using a chemical transport model. *Journal of Geophysical*
- 1089 *Research: Atmospheres*, 125, e2019JD031506. <https://doi.org/10.1029/2019JD031506>, 2020.
- 1090 Fast, J. D., et al.: Model representations of aerosol layers transported from North America over the Atlantic Ocean
- 1091 during the Two-Column Aerosol Project. *J. Geophys. Res. Atmos.*, 121, 9814–9848,
- 1092 <https://doi.org/10.1002/2016JD025248>, 2016.
- 1093 Feng, J., Chan, E., and Vet, R.: Air quality in the eastern United States and Eastern Canada for 1990–2015: 25 years
- 1094 of change in response to emission reductions of SO₂ and NO_x in the region, *Atmos. Chem. Phys.*, 20, 3107–3134,
- 1095 <https://doi.org/10.5194/acp-20-3107-2020>, 2020.
- 1096 Fischer, E. V., Jacob, D. J., Yantosca, R. M., Sulprizio, M. P., Millet, D. B., Mao, J., Paulot, F., Singh, H. B., Roiger,
- 1097 A., Ries, L., Talbot, R. W., Dzepina, K., and Pandey Deolal, S.: Atmospheric peroxyacetyl nitrate (PAN): a global
- 1098 budget and source attribution, *Atmos. Chem. Phys.*, 14, 2679–2698, <https://doi.org/10.5194/acp-14-2679-2014>,
- 1099 2014.
- 1100 Fisher, J.A., D.J. Jacob, Q. Wang, R. Bahreini, C.C. Carouge, M.J. Cubison, J.E. Dibb, T. Diehl, J.L. Jimenez, E.M.
- 1101 Leibensperger, M.B.J. Meinders, H.O.T. Pye, P.K. Quinn, S. Sharma, A. van Donkelaar, and R.M. Yantosca:
- 1102 Sources, distribution, and acidity of sulfate-ammonium aerosol in the Arctic in winter-spring, *Atmos. Environ.*, 45,
- 1103 7301-7318, 2011.
- 1104 Fountoukis, C. and Nenes, A.: ISORROPIA II: a computationally efficient thermodynamic equilibrium model for K+–
- 1105 Ca²⁺–Mg²⁺–NH₄⁺–Na⁺–SO₄²⁻–NO₃⁻–Cl⁻–H₂O aerosols, *Atmos. Chem. Phys.*, 7, 4639–4659,
- 1106 <https://doi.org/10.5194/acp-7-4639-2007>, 2007.



- 1107 Ferrare, R., Hair, J., Hostetler, C., Shingler, T., Burton, S. P., Fenn, M., Clayton, M., Scarino, A. J., Harper, D.,
1108 Seaman, S., Cook, A., Crosbie, E., Winstead, E., Ziemba, L., Thornhill, L., Robinson, C., Moore, R., Vaughan,
1109 M., Sorooshian, A., Schlosser, J. S., Liu, H., Zhang, B., Diskin, G., DiGangi, J., Nowak, J., Choi, Y., Zuidema, P.,
1110 and Chellappan, S.: Airborne HSRL-2 measurements of elevated aerosol depolarization associated with non-
1111 spherical sea salt. *Front. Remote Sens.* 4:1143944. doi: 10.3389/frsen.2023.1143944, 2023.
- 1112 Gantt, B., Johnson, M. S., Crippa, M., Prévôt, A. S. H., and Meskhidze, N.: Implementing marine organic aerosols
1113 into the GEOS-Chem model, *Geosci. Model Dev.*, 8, 619–629, <https://doi.org/10.5194/gmd-8-619-2015>, 2015.
- 1114 Gartman, N.: Quality Assurance Report National Atmospheric Deposition Program 2016,
1115 https://nadp.slh.wisc.edu/wp-content/uploads/2021/04/cal_qar_2016.pdf, 2017.
- 1116 Generoso, S., Bey, I., Labonne, M., and Breon, F. M.: Aerosol vertical distribution in dust outflow over the Atlantic:
1117 Comparisons between GEOS-Chem and Cloud-Aerosol Lidar and Infrared Pathfinder Satellite Observation
1118 (CALIPSO). *Journal of Geophysical Research*, 113(D24), D24209. <https://doi.org/10.1029/2008JD010154>, 2008.
- 1119 Giles, D. M., Sinyuk, A., Sorokin, M. G., Schafer, J. S., Smirnov, A., Slutsker, I., Eck, T. F., Holben, B. N., Lewis, J.
1120 R., Campbell, J. R., Welton, E. J., Korkin, S. V., and Lyapustin, A. I.: Advancements in the Aerosol Robotic
1121 Network (AERONET) Version 3 database – automated near-real-time quality control algorithm with improved
1122 cloud screening for Sun photometer aerosol optical depth (AOD) measurements, *Atmos. Meas. Tech.*, 12, 169-
1123 209, <https://doi.org/10.5194/amt-12-169-2019>, 2019.
- 1124 Gonzalez, M. E., Corral, A. F., Crosbie, E., Dadashazar, H., Diskin, G. S., Edwards, E.-L., Kirschler, S., Moore, R.
1125 H., Robinson, C. E., Schlosser, J. S., Shook, M., Stahl, C., Thornhill, K. L., Voigt, C., Winstead, E., Ziemba, L.
1126 D., and Sorooshian, A.: Relationships between supermicrometer particle concentrations and cloud water sea salt
1127 and dust concentrations: analysis of MONARC and ACTIVATE data, *Environmental Science: Atmospheres*,
1128 10.1039/D2EA00049K, 2022.
- 1129 Guenther, A. B., Jiang, X., Heald, C. L., Sakulyanontvittaya, T., Duhl, T., Emmons, L. K., and Wang, X.: The Model
1130 of Emissions of Gases and Aerosols from Nature version 2.1 (MEGAN2.1): an extended and updated framework
1131 for modeling biogenic emissions, *Geosci. Model Dev.*, 5, 1471-1492, <https://doi.org/10.5194/gmd-5-1471-2012>,
1132 2012.
- 1133 He, T.-L., Jones, D., Molod, A., Kouatchou, J., Zhang, B., Liu, H., Yu, K., and Yantosca, R.: Sensitivity analysis and
1134 optimization of the RAS system in GEOS-Chem, 9th International GEOS-Chem Meeting, 6–9 May 2019,
1135 Cambridge, MA, USA, 2019.
- 1136 Hilario, M. R. A., Crosbie, E., Shook, M., Reid, J. S., Cambaliza, M. O. L., Simpas, J. B. B., Ziemba, L., DiGangi, J.
1137 P., Diskin, G. S., Nguyen, P., Turk, F. J., Winstead, E., Robinson, C. E., Wang, J., Zhang, J., Wang, Y., Yoon, S.,
1138 Flynn, J., Alvarez, S. L., Behrangi, A., and Sorooshian, A.: Measurement report: Long-range transport patterns
1139 into the tropical northwest Pacific during the CAMP²Ex aircraft campaign: chemical composition, size
1140 distributions, and the impact of convection, *Atmos. Chem. Phys.*, 21, 3777–3802, <https://doi.org/10.5194/acp-21-3777-2021>, 2021.



- 1142 Holben, B. N., Eck, T. F., Slutsker, I., Tanre, D., Buis, J. P., Setzer, A., et al.: AERONET—A federated instrument
1143 network and data archive for aerosol characterization. *Remote Sensing of Environment*, 66(1), 1–16.
1144 [https://doi.org/10.1016/s0034-4257\(98\)00031-5](https://doi.org/10.1016/s0034-4257(98)00031-5), 1998.
- 1145 Hubanks, P., S. Platnick, M. King, and B. Ridgway: MODIS Algorithm Theoretical Basis Document No. ATBD-
1146 MOD-30 for Level-3 Global Gridded Atmosphere Products (08_D3, 08_E3, 08_M3) and Users Guide (Collection
1147 6.0 & 6.1, Version 4.4, 20 Feb 2019), [https://atmosphere-
imager.gsfc.nasa.gov/sites/default/files/ModAtmo/L3_ATBD_C6_C61_2019_02_20.pdf](https://atmosphere-
1148 imager.gsfc.nasa.gov/sites/default/files/ModAtmo/L3_ATBD_C6_C61_2019_02_20.pdf), 2019.
- 1149 Jacob, D. J., J. A. Logan, G. M. Gardner, R. M. Yevich, C. M. Spivakovsky, and S. C. Wofsy: Factors regulating
1150 ozone over the United States and its export to the global atmosphere, *J. Geophys. Res.*, 98, 14,817–14,826, 1993.
- 1151 Jaeglé, L., Quinn, P. K., Bates, T. S., Alexander, B., and Lin, J.-T.: Global distribution of sea salt aerosols: new
1152 constraints from in situ and remote sensing observations, *Atmos. Chem. Phys.*, 11, 3137–3157,
1153 <https://doi.org/10.5194/acp-11-3137-2011>, 2011.
- 1154 Jaffe, D., Snow, J., and Cooper, O.: The 2001 Asian dust events: Transport and impact on surface aerosol
1155 concentrations in the US. *Eos, Transactions American Geophysical Union*, 84(46), 501–507.
1156 <https://doi.org/10.1029/2003eo460001>, 2003.
- 1157 Jongeward, A.R., Z. Li, H. He, and X. Xiong: Natural and Anthropogenic Aerosol Trends from Satellite and Surface
1158 Observations and Model Simulations over the North Atlantic Ocean from 2002 to 2012. *J. Atmos. Sci.*, 73, 4469–
1159 4485, <https://doi.org/10.1175/JAS-D-15-0308.1>, 2016.
- 1160 Keller, C. A., Knowland, K. E., Duncan, B. N., Liu, J., Anderson, D. C., Das, S., et al.: Description of the NASA
1161 GEOS composition forecast modeling system GEOS-CF v1.0. *Journal of Advances in Modeling Earth Systems*,
1162 13, e2020MS002413. <https://doi.org/10.1029/2020MS002413>, 2021.
- 1163 Kim, D., Chin, M., Yu, H. B., Diehl, T., Tan, Q., Kahn, R. A., et al.: Sources, sinks, and transatlantic transport of
1164 North African dust aerosol: A multimodel analysis and comparison with remote sensing data. *Journal of
1165 Geophysical Research-Atmospheres*, 119, 6259–6277. <https://doi.org/10.1002/2013JD021099>, 2014.
- 1166 Kim, P.S., et al.: Sources, seasonality, and trends of southeast US aerosol: an integrated analysis of surface, aircraft,
1167 and satellite observations with the GEOS-Chem chemical transport model, *Atmos. Chem. Phys.*, 15, 10411–10433,
1168 2015 www.atmos-chem-phys.net/15/10411/2015/ doi:10.5194/acp-15-10411-2015, 2015.
- 1169 Kim, M.-H., Omar, A. H., Tackett, J. L., Vaughan, M. A., Winker, D. M., Trepte, C. R., Hu, Y., Liu, Z., Poole, L. R.,
1170 Pitts, M. C., Kar, J., and Magill, B. E.: The CALIPSO version 4 automated aerosol classification and lidar ratio
1171 selection algorithm, *Atmos. Meas. Tech.*, 11, 6107–6135, <https://doi.org/10.5194/amt-11-6107-2018>, 2018.
- 1172 Lamb, P. J., and Pepler, R. A.: North Atlantic Oscillation: Concept and an application. *Bulletin of the American
1173 Meteorological Society*, 68(10), 1218–1225. [https://doi.org/10.1175/1520-0477\(1987\)068<1218:naocaa>2.0.co;2](https://doi.org/10.1175/1520-0477(1987)068<1218:naocaa>2.0.co;2),
1174 1987.
- 1175 Lana, A., et al.: An updated climatology of surface dimethylsulfide concentrations and emission fluxes in the global
1176 ocean, *Global Biogeochem. Cycles*, 25, GB1004, doi:10.1029/2010GB003850, 2011.



- 1177 Levy, R. C., S. Mattoo, L. A. Munchak, L. A. Remer, A. M. Sayer, F. Patadia, and N. C. Hsu: The Collection 6
1178 MODIS aerosol products over land and ocean, *Atmos. Meas. Tech.*, 6, 2989–3034, doi:10.5194/amt-6-2989-2013,
1179 2013.
- 1180 Li, Q. B., et al.: Transatlantic transport of pollution and its effects on surface ozone in Europe and North America, *J.*
1181 *Geophys. Res.*, 107(D13), 4166, doi:10.1029/2001JD001422, 2002.
- 1182 Li, Q. B., Jacob, D. J., Park, R., Wang, Y. X., Heald, C. L., Hudman, R., et al.: North American pollution outflow and
1183 the trapping of convectively lifted pollution by upper-level anticyclone. *Journal of Geophysical Research*,
1184 110(D10), D10301. <https://doi.org/10.1029/2004jd005039>, 2005.
- 1185 Li, M., Zhang, Q., Streets, D. G., He, K. B., Cheng, Y. F., Emmons, L. K., et al.: Mapping Asian anthropogenic
1186 emissions of non-methane volatile organic compounds to multiple chemical mechanisms. *Atmospheric Chemistry*
1187 *and Physics*, 14, 5617–5638. <https://doi.org/10.5194/acp-14-5617-2014>, 2014.
- 1188 Li, X.-Y., Wang, H., Chen, J., Endo, S., George, G., Cairns, B., Chellappan, S., Zeng, X., Kirschler, S., Voigt, C.,
1189 Sorooshian, A., Crosbie, E., Chen, G., Ferrare, R. A., Gustafson, W. I., Hair, J. W., Kleb, M. M., Liu, H., Moore,
1190 R., Painemal, D., Robinson, C., Scarino, A. J., Shook, M., Shingler, T. J., Thornhill, K. L., Tornow, F., Xiao, H.,
1191 Ziemba, L. D., and Zuidema, P.: Large-Eddy Simulations of Marine Boundary Layer Clouds Associated with Cold-
1192 Air Outbreaks during the ACTIVATE Campaign. Part I: Case Setup and Sensitivities to Large-Scale Forcings,
1193 *Journal of the Atmospheric Sciences*, 79, 73-100, 10.1175/jas-d-21-0123.1, 2022.
- 1194 Lin, J.-T., and M. McElroy: Impacts of boundary layer mixing on pollutant vertical profiles in the lower troposphere:
1195 Implications to satellite remote sensing, *Atmospheric Environment*, 44(14), 1726-1739,
1196 doi:10.1016/j.atmosenv.2010.02.009, 2010.
- 1197 Lin, S.-J., and Rood, R. B.: Multidimensional flux form semi-Lagrangian transport schemes, *Mon. Wea. Rev.*, 124,
1198 2046-2070, 1996.
- 1199 Liu, H., D. J. Jacob, I. Bey, and R. M. Yantosca: Constraints from ²¹⁰Pb and ⁷Be on wet deposition and transport in a
1200 global three-dimensional chemical tracer model driven by assimilated meteorological fields, *J. Geophys. Res. Vol.*
1201 106(D11), 12,109-12,128, 2001.
- 1202 Liu, Z., J. Kar, S. Zeng, J. Tackett, M. Vaughan, M. Avery, J. Pelon, B. Getzewich, K.-P. Lee, B. Magill, A. Omar, P.
1203 Luckner, C. Trepte, and D. Winker: Discriminating Between Clouds and Aerosols in the CALIOP Version 4.1 Data
1204 Products, *Atmos. Meas. Tech.*, 12, 703–734, <https://doi.org/10.5194/amt-12-703-2019>, 2019.
- 1205 Liu, H., and Zhang, B.: GEOS-Chem v11-01 for simulating tropospheric aerosols over the western North Atlantic
1206 Ocean. Zenodo. <https://doi.org/10.5281/zenodo.10982278>, 2024.
- 1207 Luan, Y. and Jaeglé, L.: Composite study of aerosol export events from East Asia and North America, *Atmos. Chem.*
1208 *Phys.*, 13, 1221-1242, <https://doi.org/10.5194/acp-13-1221-2013>, 2013.
- 1209 Luo, G., Yu, F., and Schwab, J.: Revised treatment of wet scavenging processes dramatically improves GEOS-Chem
1210 12.0.0 simulations of surface nitric acid, nitrate, and ammonium over the United States, *Geosci. Model Dev.*, 12,
1211 3439–3447, <https://doi.org/10.5194/gmd-12-3439-2019>, 2019.



- 1212 Luo, G., Yu, F., and Moch, J. M.: Further improvement of wet process treatments in GEOS-Chem v12.6.0: impact on
1213 global distributions of aerosols and aerosol precursors, *Geosci. Model Dev.*, 13, 2879–2903,
1214 <https://doi.org/10.5194/gmd-13-2879-2020>, 2020.
- 1215 Malm, W. C., Sisler, J. F., Huffman, D., Eldred, R. A., and Cahill, T. A.: Spatial and seasonal trends in particle
1216 concentration and optical extinction in the United States. *Journal of Geophysical Research-Atmospheres*, 99(D1),
1217 1347–1370. <https://doi.org/10.1029/93JD02916>, 1994.
- 1218 Mardi, A. H., Dadashazar, H., Painemal, D., Shingler, T., Seaman, S. T., Fenn, M. A., et al.: Biomass burning over
1219 the United States East Coast and western North Atlantic Ocean: Implications for clouds and air quality. *Journal of*
1220 *Geophysical Research: Atmospheres*, 126, e2021JD034916. <https://doi.org/10.1029/2021JD034916>, 2021.
- 1221 Martin, R. V., D. J. Jacob, R. M. Yantosca, M. Chin, and P. Ginoux: Global and regional decreases in tropospheric
1222 oxidants from photochemical effects of aerosols, *J. Geophys. Res.*, 108(D3), 4097, doi:10.1029/2002JD002622,
1223 2003.
- 1224 McGrath-Spangler, E. L. and Molod, A.: Comparison of GEOS-5 AGCM planetary boundary layer depths computed
1225 with various definitions, *Atmos. Chem. Phys.*, 14, 6717–6727, <https://doi.org/10.5194/acp-14-6717-2014>, 2014.
- 1226 Murray, L. T., Jacob, D. J., Logan, J. A., Hudman, R. C., and Koshak, W. J.: Optimized regional and interannual
1227 variability of lightning in a global chemical transport model constrained by LIS/OTD satellite data, *J. Geophys.*
1228 *Res.*, 117, D20307, doi:10.1029/2012JD017934, 2012.
- 1229 Neuman, J. A., Parrish, D. D., Trainer, M., Ryerson, T. B., Holloway, J. S., Nowak, J. B., et al.: Reactive nitrogen
1230 transport and photochemistry in urban plumes over the North Atlantic Ocean. *Journal of Geophysical Research*,
1231 111, D23S54. <https://doi.org/10.1029/2005JD007010>, 2006.
- 1232 Painemal, D., Chellappan, S., Smith, W. L. Jr., Spangenberg, D., Park, J. M., Ackerman, A., et al.: Wintertime synoptic
1233 patterns of midlatitude boundary layer clouds over the western North Atlantic: Climatology and insights from in
1234 situ ACTIVATE observations. *Journal of Geophysical Research: Atmospheres*, 128, e2022JD037725.
1235 <https://doi.org/10.1029/2022JD037725>, 2023.
- 1236 Painemal, D., Corral, A. F., Sorooshian, A., Brunke, M. A., Chellappan, S., Gorrooh, V. A., et al.: An overview of
1237 atmospheric features over the Western North Atlantic Ocean and North American East Coast—Part 2: Circulation,
1238 boundary layer, and clouds. *Journal of Geophysical Research: Atmospheres*, 126, e2020JD033423.
1239 <https://doi.org/10.1029/2020JD033423>, 2021.
- 1240 Park, R. J., D. J. Jacob, B. D. Field, R. M. Yantosca, and M. Chin: Natural and transboundary pollution influences on
1241 sulfate-nitrate-ammonium aerosols in the United States: Implications for policy, *J. Geophys. Res.*, 109, D15204,
1242 doi:10.1029/2003JD004473, 2004.
- 1243 Perry, K. D., Cahill, T. A., Eldred, R. A., Dutcher, D. D., and Gill, T. E.: Long-range transport of North African dust
1244 to the eastern United States, *J. Geophys. Res.*, 102(D10), 11225– 11238, doi:10.1029/97JD00260, 1997.
- 1245 Peyridieu, S., Chédin, A., Tanré, D., Capelle, V., Pierangelo, C., Lamquin, N., and Armante, R.: Saharan dust infrared
1246 optical depth and altitude retrieved from AIRS: a focus over North Atlantic – comparison to MODIS and
1247 CALIPSO, *Atmos. Chem. Phys.*, 10, 1953–1967, <https://doi.org/10.5194/acp-10-1953-2010>, 2010.



- 1248 Pfister, G. G., et al.: Ozone production from the 2004 North American boreal fires, *J. Geophys. Res.*, 111, D24S07,
1249 doi:10.1029/2006JD007695, 2006.
- 1250 Philip, S., Martin, R. V., and Keller, C. A.: Sensitivity of chemistry-transport model simulations to the duration of
1251 chemical and transport operators: a case study with GEOS-Chem v10-01, *Geosci. Model Dev.*, 9, 1683–1695,
1252 <https://doi.org/10.5194/gmd-9-1683-2016>, 2016.
- 1253 Philip, S., Marin, R. V., Pierce, J. R., Jimenez, J. L., Zhang, Q., Canagaratna, M. R., Spracklen, D. V., Nowlan, C. R.,
1254 Lamsal, L. N., Cooper, M. J., and Krotkov, N. A.: Spatially and seasonally resolved estimate of the ratio of organic
1255 mass to organic carbon, *Atmos. Environ.*, 87, 34-40, <http://dx.doi.org/10.1016/j.atmosenv.2013.11.065>, 2014.
- 1256 Provençal, S., P. Kishcha, A.M. da Silva, E. Elhacham, and P. Alpert: AOD distributions and trends of major aerosol
1257 species over a selection of the world's most populated cities based on the 1st version of NASA's MERRA Aerosol
1258 Reanalysis, *Urban Climate*, 20, 168-191, <https://doi.org/10.1016/j.uclim.2017.04.001>, 2017.
- 1259 Pye, H. O. T., Chan, A. W. H., Barkley, M. P., and Seinfeld, J. H.: Global modeling of organic aerosol: the importance
1260 of reactive nitrogen (NO_x and NO₃), *Atmos. Chem. Phys.*, 10, 11261-11276, [https://doi.org/10.5194/acp-10-](https://doi.org/10.5194/acp-10-11261-2010)
1261 [11261-2010](https://doi.org/10.5194/acp-10-11261-2010), 2010.
- 1262 Pye, H. O. T. and Seinfeld, J. H.: A global perspective on aerosol from low-volatility organic compounds, *Atmos.*
1263 *Chem. Phys.*, 10, 4377–4401, doi:10.5194/acp-10-4377-2010, 2010.
- 1264 Quinn, P. K. and Bates, T.: Ocean-Derived Aerosol and Its Climate impacts, in: *Treatise on Geochemistry*, Elsevier,
1265 Oxford, 317–330, <https://doi.org/10.1016/b978-0-08-095975-7.00416-2>, 2014.
- 1266 Ridley, D. A., Heald, C. L., and Ford, B.: North African dust export and deposition: A satellite and model perspective,
1267 *J. Geophys. Res.*, 117, D02202, doi:10.1029/2011JD016794, 2012.
- 1268 Savoie, D. L., and Prospero, J. M.: Aerosol concentration statistics for northern tropical Atlantic. *Journal of*
1269 *Geophysical Research*, 82(37), 5954–5964, 1997.
- 1270 Sayer, A.M., L. A. Munchak, N. C. Hsu, R. C. Levy, C. Bettenhausen, and M.-J. Jeong: MODIS Collection 6 aerosol
1271 products: Comparison between Aqua's e-Deep Blue, Dark Target, and “merged” data sets, and usage
1272 recommendations, *J. Geophys. Res. Atmos.*, 119, 13,965–13,989, doi:10.1002/2014JD022453, 2014.
- 1273 Seethala, C., Zuidema, P., Edson, J., Brunke, M., Chen, G., Li, X.-Y., Painemal, D., Robinson, C., Shingler, T., Shook,
1274 M., Sorooshian, A., Thornhill, L., Tornow, F., Wang, H., Zeng, X., and Ziemba, L.: On Assessing ERA5 and
1275 MERRA2 Representations of Cold-Air Outbreaks Across the Gulf Stream, *Geophysical Research Letters*, 48,
1276 e2021GL094364, <https://doi.org/10.1029/2021GL094364>, 2021.
- 1277 Shah, V., L. Jaeglé, J.L. Jimenez, J.C. Schroder, P. Campuzano-Jost, T.L. Campos, J.M. Reeves, M. Stell, S.S. Brown,
1278 B.H. Lee, F.D. Lopez-Hilfiker, and J.A. Thornton: Widespread pollution from secondary sources of organic
1279 aerosols during winter in the northeastern United States. *Geophys. Res. Lett.*, 46, 2976-2983, 2019. DOI:
1280 [10.1029/2018GL081530](https://doi.org/10.1029/2018GL081530), 2019.
- 1281 Shingler, T., Dey, S., Sorooshian, A., Brechtel, F. J., Wang, Z., Metcalf, A., Coggon, M., Mulmenstadt, J., Russell, L.
1282 M., Jonsson, H. H., and Seinfeld, J. H.: Characterisation and airborne deployment of a new counterflow virtual
1283 impactor inlet, *Atmos Meas Tech*, 5, 1259-1269, [10.5194/amt-5-1259-2012](https://doi.org/10.5194/amt-5-1259-2012), 2012.



- 1284 Silva, S. J., Ridley, D. A., and Heald, C. L.: Exploring the constraints on simulated aerosol sources and transport
1285 across the North Atlantic with island-based sun photometers. *Earth and Space Science*, 7, e2020EA001392.
1286 <https://doi.org/10.1029/2020EA001392>, 2020.
- 1287 Smirnov, A., Holben, B. N., Eck, T. F., Dubovik, O., and Slutsker, I.: Cloud screening and quality control algorithms
1288 for the AERONET database, *Remote Sens. Environ.*, 73, 337–349, [https://doi.org/10.1016/S0034-4257\(00\)00109-](https://doi.org/10.1016/S0034-4257(00)00109-7)
1289 7, 2000.
- 1290 Solomon, P.A., Dennis Crumpler, James B. Flanagan, R.K.M. Jayanty, Ed E. Rickman, and Charles E. McDade: U.S.
1291 National PM_{2.5} Chemical Speciation Monitoring Networks—CSN and IMPROVE: Description of networks,
1292 *Journal of the Air & Waste Management Association*, 64:12, 1410-1438, DOI: 10.1080/10962247.2014.956904,
1293 2014.
- 1294 Sorooshian, A., B. Anderson, S.E. Bauer, R.A. Braun, B. Cairns, E. Crosbie, H. Dadashazar, G. Diskin, R. Ferrare,
1295 R.C. Flagan, J. Hair, C. Hostetler, H.H. Jonsson, M.M. Kleb, H. Liu, A.B. MacDonald, A. McComiskey, R. Moore,
1296 D. Painemal, L.M. Russell, J.H. Seinfeld, M. Shook, W.L. Smith, K. Thornhill, G. Tselioudis, H. Wang, X. Zeng,
1297 B. Zhang, L. Ziemba, and P. Zuidema: Aerosol–Cloud–Meteorology Interaction Airborne Field Investigations:
1298 Using Lessons Learned from the U.S. West Coast in the Design of ACTIVATE off the U.S. East Coast. *Bull.*
1299 *Amer. Meteor. Soc.*, 100, 1511–1528, <https://doi.org/10.1175/BAMS-D-18-0100.1>, 2019.
- 1300 Sorooshian, A., Corral, A. F., Braun, R. A., Cairns, B., Crosbie, E., Ferrare, R. et al.: Atmospheric Research Over the
1301 Western North Atlantic Ocean Region and North American East Coast: A Review of Past Work and Challenges
1302 Ahead. *J. Geophys. Res-Atmos*, 125, e2019JD031626. <https://doi.org/10.1029/2019JD031626>, 2020.
- 1303 Sorooshian, A., Alexandrov, M. D., Bell, A. D., Bennett, R., Betito, G., Burton, S. P., Buzanowicz, M. E., Cairns, B.,
1304 Chemyakin, E. V., Chen, G., Choi, Y., Collister, B. L., Cook, A. L., Corral, A. F., Crosbie, E. C., van Dienenhoven,
1305 B., DiGangi, J. P., Diskin, G. S., Dmitrovic, S., Edwards, E.-L., Fenn, M. A., Ferrare, R. A., van Gilst, D., Hair, J.
1306 W., Harper, D. B., Hilario, M. R. A., Hostetler, C. A., Jester, N., Jones, M., Kirschler, S., Kleb, M. M., Kusterer,
1307 J. M., Leavor, S., Lee, J. W., Liu, H., McCauley, K., Moore, R. H., Nied, J., Notari, A., Nowak, J. B., Painemal,
1308 D., Phillips, K. E., Robinson, C. E., Scarino, A. J., Schlosser, J. S., Seaman, S. T., Seethala, C., Shingler, T. J.,
1309 Shook, M. A., Sinclair, K. A., Smith Jr., W. L., Spangenberg, D. A., Stamnes, S. A., Thornhill, K. L., Voigt, C.,
1310 Vömel, H., Wasilewski, A. P., Wang, H., Winstead, E. L., Zeider, K., Zeng, X., Zhang, B., Ziemba, L. D., and
1311 Zuidema, P.: Spatially coordinated airborne data and complementary products for aerosol, gas, cloud, and
1312 meteorological studies: the NASA ACTIVATE dataset, *Earth Syst. Sci. Data*, 15, 3419–3472,
1313 <https://doi.org/10.5194/essd-15-3419-2023>, 2023.
- 1314 Stettler, M. E. J., Eastham, S., Barrett, S. R. H.: Air quality and public health impacts of UK airports. Part I: Emissions.
1315 *Atmospheric Environment*, 45(31), 5415–5424. <https://doi.org/10.1016/j.atmosenv.2011.07.012>, 2011.
- 1316 Stohl, A. et al.: Validation of the Lagrangian particle dispersion model FLEXPART against large-scale tracer
1317 experiment data. *Atmospheric Environment*, 32(24), pp.4245-4264, 1998.
- 1318 Streets, D. G., Wu, Y., and Chin, M.: Two-Decadal Aerosol Trends as a Likely Explanation of the Global
1319 Dimming/Brightening Transition. *Geophys. Res. Lett.*, 33, L15806. <https://doi.org/10.1029/2006GL026471>, 2006.



- 1320 Tackett, J. L., Winker, D. M., Getzewich, B. J., Vaughan, M. A., Young, S. A., and Kar, J.: CALIPSO lidar level 3
1321 aerosol profile product: Version 3 algorithm design. *Atmospheric Measurement Techniques*, 11(7), 4129–4152.
1322 <https://doi.org/10.5194/amt-11-4129-2018>, 2018.
- 1323 Tai, A. P. K., Mickley, L. J., and Jacob, D. J.: Correlations between Fine Particulate Matter (PM_{2.5}) and
1324 meteorological variables in the United States: Implications for the sensitivity of PM_{2.5} to climate change.
1325 *Atmospheric Environment*, 44(32), 3976–3984. <https://doi.org/10.1016/j.atmosenv.2010.06.060>, 2010.
- 1326 Tornow, F., Ackerman, A. S., Fridlind, A. M., Cairns, B., Crosbie, E. C., Kirschler, S., Moore, R. H., Painemal, D.,
1327 Robinson, C. E., Seethala, C., Shook, M. A., Voigt, C., Winstead, E. L., Ziemba, L. D., Zuidema, P., and
1328 Sorooshian, A.: Dilution of Boundary Layer Cloud Condensation Nucleus Concentrations by Free Tropospheric
1329 Entrainment During Marine Cold Air Outbreaks, *Geophysical Research Letters*, 49, e2022GL098444,
1330 <https://doi.org/10.1029/2022GL098444>, 2022.
- 1331 Travis, K. R., Jacob, D. J., Fisher, J. A., Kim, P. S., Marais, E. A., Zhu, L., et al.: Why do models overestimate surface
1332 ozone in the Southeast United States? *Atmos. Chem. Phys.*, 16, 13,561–13,577. [https://doi.org/10.5194/acp-16-](https://doi.org/10.5194/acp-16-13561-2016)
1333 [13561-2016](https://doi.org/10.5194/acp-16-13561-2016), 2016.
- 1334 Tucker, G. B., and R. G. Barry: Climate of the North Atlantic Ocean. In *Climates of the Oceans* (H. Van Loon, ed.)
1335 New York: Elsevier, 193 – 262. <http://hdl.handle.net/102.100.100/282631?index=1>, 1984.
- 1336 val Martin, M., Logan, J. A., Kahn, R. A., Leung, F.-Y., Nelson, D. L., and Diner, D. J.: Smoke injection heights from
1337 fires in North America: analysis of 5 years of satellite observations, *Atmos. Chem. Phys.*, 10, 1491–1510,
1338 <https://doi.org/10.5194/acp-10-1491-2010>, 2010.
- 1339 van Donkelaar, A., et al.: Regional Estimates of Chemical Composition of Fine Particulate Matter using a Combined
1340 Geoscience-Statistical Method with Information from Satellites, Models, and Monitors. *Environmental Science &*
1341 *Technology*, 2019, doi:10.1021/acs.est.8b06392, 2019.
- 1342 Wang, Q., D.J. Jacob, J.A. Fisher, J. Mao, E.M. Leibensperger, C.C. Carouge, P. Le Sager, Y. Kondo, J.L. Jimenez,
1343 M.J. Cubison, and S.J. Doherty: Sources of carbonaceous aerosols and deposited black carbon in the Arctic in
1344 winter-spring: implications for radiative forcing, *Atmos. Chem. Phys.*, 11, 12,453-12,473, 2011.
- 1345 Wang, Q., D.J. Jacob, J.R. Spackman, A.E. Perring, J.P. Schwarz, N. Moteki, E.A. Marais, C. Ge, J. Wang, and S.R.H.
1346 Barrett: Global budget and radiative forcing of black carbon aerosol: constraints from pole-to-pole (HIPPO)
1347 observations across the Pacific, *J. Geophys. Res.*, 119, 195-206, 2014.
- 1348 Wesely, M. L.: Parameterization of surface resistance to gaseous dry deposition in regional-scale numerical
1349 models, *Atmos. Environ.*, 23, 1293-1304, 1989.
- 1350 Winker, D. M., Pelon, J., Coakley Jr, J. A., Ackerman, S. A., Charlson, R. J., Colarco, P. R., Flamant, P., Fu, Q., Hoff,
1351 R. M., Kittaka, C., Kubar, T. L., Le Treut, H., McCormick, M. P., Mégie, G., Poole, L., Powell, K., Trepte, C.,
1352 Vaughan, M. A., and Wielicki, B. A.: The CALIPSO mission: A global 3D view of aerosols and clouds, *Bull.*
1353 *Amer. Meteor. Soc.*, 91, 1211–1229, <https://doi.org/10.1175/2010BAMS3009.1>, 2010.
- 1354 Winker, D. M., Tackett, J. L., Getzewich, B. J., Liu, Z., Vaughan, M. A., and Rogers, R. R.: The global 3-D distribution
1355 of tropospheric aerosols as characterized by CALIOP, *Atmos. Chem. Phys.*, 13, 3345–3361,
1356 <https://doi.org/10.5194/acp-13-3345-2013>, 2013.



- 1357 Wu, S., L.J. Mickley, D.J. Jacob, J.A. Logan, R.M. Yantosca, and D. Rind: Why are there large differences between
1358 models in global budgets of tropospheric ozone? *J. Geophys. Res.*, 112, D05302, doi:10.1029/2006JD007801,
1359 2007.
- 1360 Wu, H., X. Xu, T. Luo, Y. Yang, Z. Xiong, and Y. Wang: Variation and comparison of cloud cover in MODIS and
1361 four reanalysis datasets of ERA-interim, ERA5, MERRA-2 and NCEP. *Atmos. Res.*, 281,
1362 106477, <https://doi.org/10.1016/j.atmosres.2022.106477>, 2022.
- 1363 Yang, Y., Wang, H., Smith, S. J., Zhang, R., Lou, S., Yu, H., et al.: Source apportionments of aerosols and their direct
1364 radiative forcing and long-term trends over continental United States. *Earth's Future*, 6, 793– 808.
1365 <https://doi.org/10.1029/2018EF000859>, 2018.
- 1366 Yu, F., A. Nair, and G. Luo: Long term trend of gaseous ammonia in US: Modeling and comparison with observations,
1367 *Journal of Geophysical Research: Atmospheres*, 123, 8315–8325, 2018.
- 1368 Yu, H., M. Chin, D. M. Winker, A. H. Omar, Z. Liu, C. Kittaka, and T. Diehl: Global view of aerosol vertical
1369 distributions from CALIPSO lidar measurements and GOCART simulations: Regional and seasonal variations, *J.*
1370 *Geophys. Res.*, 115, D00H30, doi:10.1029/2009JD013364, 2010.
- 1371 Yu, K., Keller, C. A., Jacob, D. J., Molod, A. M., Eastham, S. D., and Long, M. S.: Errors and improvements in the
1372 use of archived meteorological data for chemical transport modeling: an analysis using GEOS-Chem v11-01 driven
1373 by GEOS-5 meteorology, *Geosci. Model Dev.*, 11, 305–319, <https://doi.org/10.5194/gmd-11-305-2018>, 2018.
- 1374 Zender, C. S., Bian, H., and Newman, D.: Mineral dust entrainment and deposition (DEAD) model: Description and
1375 1990s dust climatology. *Journal of Geophysical Research*, 108(D14), 4416.
1376 <https://doi.org/10.1029/2002JD002775>, 2003.
- 1377 Zhang, L., J. F. Kok, D. K. Henze, Q. Li, and C. Zhao: Improving simulations of fine dust surface concentrations over
1378 the western United States by optimizing the particle size distribution, *Geophys. Res. Lett.*, 40, 3270–
1379 3275, doi:10.1002/grl.50591, 2013.
- 1380 Zhang, B., Liu, H., Crawford, J. H., Chen, G., Fairlie, T. D., Chambers, S., Kang, C.-H., Williams, A. G., Zhang, K.,
1381 Considine, D. B., Sulprizio, M. P., and Yantosca, R. M.: Simulation of radon-222 with the GEOS-Chem global
1382 model: emissions, seasonality, and convective transport, *Atmos. Chem. Phys.*, 21, 1861–1887,
1383 <https://doi.org/10.5194/acp-21-1861-2021>, 2021.
- 1384 Zheng, G., Arthur J. Sedlacek, Allison C. Aiken, Yan Feng, Thomas B. Watson, Shira Raveh-Rubin, Janek Uin, Ernie
1385 R. Lewis, and Jian Wang: Long-range transported North American wildfire aerosols observed in marine boundary
1386 layer of eastern North Atlantic, *Environment International*, 139, 105680,
1387 <https://doi.org/10.1016/j.envint.2020.105680>, 2020.
- 1388 Zhu, L., Val Martin, M., Gatti, L. V., Kahn, R., Hecobian, A., and Fischer, E. V.: Development and implementation
1389 of a new biomass burning emissions injection height scheme (BBEIH v1.0) for the GEOS-Chem model (v9-01-
1390 01), *Geosci. Model Dev.*, 11, 4103–4116, <https://doi.org/10.5194/gmd-11-4103-2018>, 2018.
- 1391 Zhuang, Y., Fu, R., Santer, B. D., Dickinson, R. E., and Hall, A.: Quantifying contributions of natural variability and
1392 anthropogenic forcings on increased fire weather risk over the western United States, *Proceedings of the National*
1393 *Academy of Sciences*, 118(45), e2111875118, doi:10.1073/pnas.2111875118, 2021.



1394

1395

Tables and Figures

1396

1397

1398

1399

Table 1. GEOS-Chem model simulations for Feb.-Mar. and Aug.-Sep. 2020.

Model simulations	Stratiform cloud water content (CWC)*	QFED biomass burning emission injection heights	Emissions
standard	MERRA-2*	PBL	all
fixedCWC	$1.0 \times 10^{-3} \text{ kg m}^{-3}$ *	PBL	all
BB0-5.5km	MERRA-2	0-5.5 km	all
BB2-10km	MERRA-2	2-10 km [†]	all
noanthbf	MERRA-2	PBL	zero anthropogenic and biofuel emissions
nobb	MERRA-2	N/A	zero biomass burning emissions
nobg	MERRA-2	PBL	zero biogenic emissions
nomari	MERRA-2	PBL	zero marine emissions
nodu	MERRA-2	PBL	zero dust emissions

1400

*CWC is used in the model parameterization for aerosol scavenging due to stratiform precipitation. Its value is either taken from MERRA-2 (Luo et al., 2019, 2020) or assumed a fixed constant of $1.0 \times 10^{-3} \text{ kg m}^{-3}$ (Del Genio et al., 1996; Wang et al., 2011).

1401

1402

1403

[†]This simulation is for Aug.-Sep. 2020 only.

1404

1405



1406
1407 **Figures**

1408
1409

1410

1411

1412

1413

1414

1415

1416

1417

1418

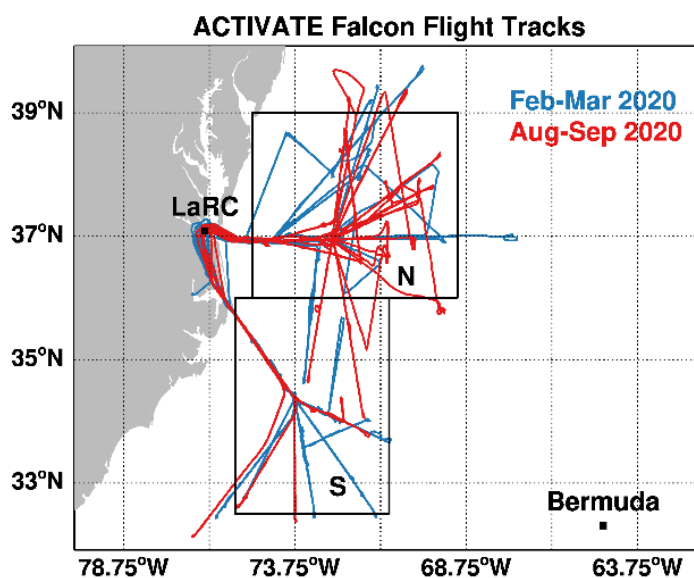
1419

1420

1421

1422

1423



1424 **Figure 1.** Falcon (HU-25) flight tracks during the winter (Feb. 14 - Mar. 12) and summer (Aug. 13 – Sep. 30) campaigns of
1425 ACTIVATE 2020. Almost all flights are based out of NASA Langley Research Center (LaRC), with a few in the winter campaign
1426 based out of the nearby Newport News/Williamsburg International Airport. The aircraft sampling domain is divided at 36°N into
1427 two box regions, the north ("N"; 36-39°N, 69-75°W) and the south ("S"; 32.5-36°N, 71-75.5°W), for data analysis.

1428



1429

1430

1431

1432

1433

1434

1435

1436

1437

1438

1439

1440

1441

1442

1443

1444

1445

1446

1447

1448

1449

1450

1451

1452

1453

1454

1455

1456

1457

1458

1459

1460

1461

1462

1463

1464

1465

1466

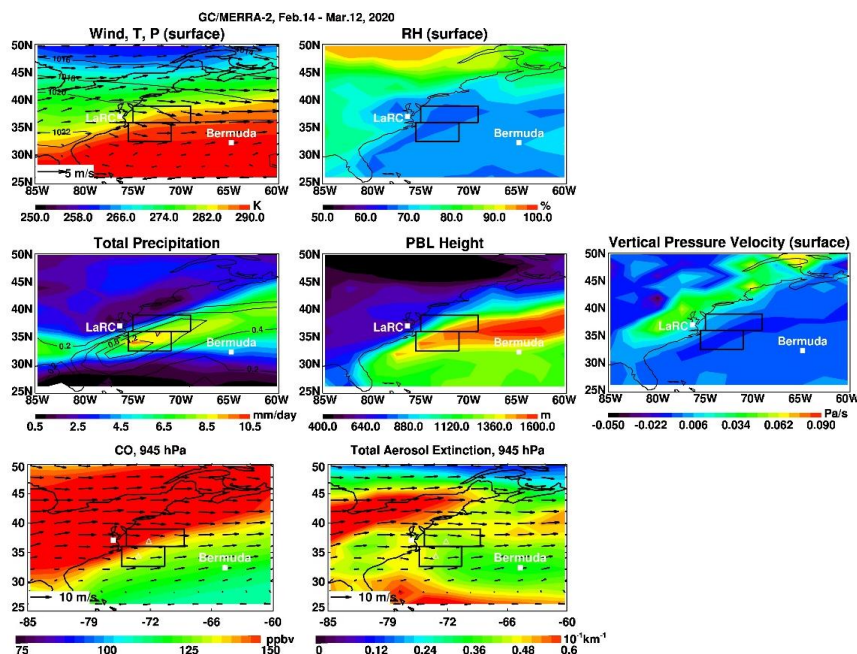


Figure 2a. Mean meteorological conditions from MERRA-2 and near-surface (945 hPa) CO concentrations (ppbv) and aerosol extinctions at 550 nm (km^{-1}) in GEOS-Chem during Feb.-Mar. 2020. **Top row:** Left panel shows horizontal wind (m/s, vectors) and temperature (K, image) at the model bottom layer, as well as sea level pressure (hPa, contours). Right two panels show relative humidity (RH, %) and vertical pressure velocity (ω , Pa/s). **Middle row:** Total precipitation (mm/day, image), convective precipitation (mm/day, contours), and PBL height (m). **Bottom row:** Model simulated CO concentrations and aerosol extinction overlaid with horizontal wind vectors at 945 hPa. The two rectangular boxes denote major flight areas (see “N” and “S” in Fig. 1) of Feb.-Mar. and Aug.-Sep. 2020. The locations of LaRC and Bermuda are marked by white squares.



1467
1468
1469
1470
1471
1472
1473
1474
1475
1476
1477
1478
1479
1480
1481
1482
1483
1484
1485
1486
1487
1488
1489
1490
1491
1492
1493
1494
1495
1496
1497
1498
1499
1500
1501
1502

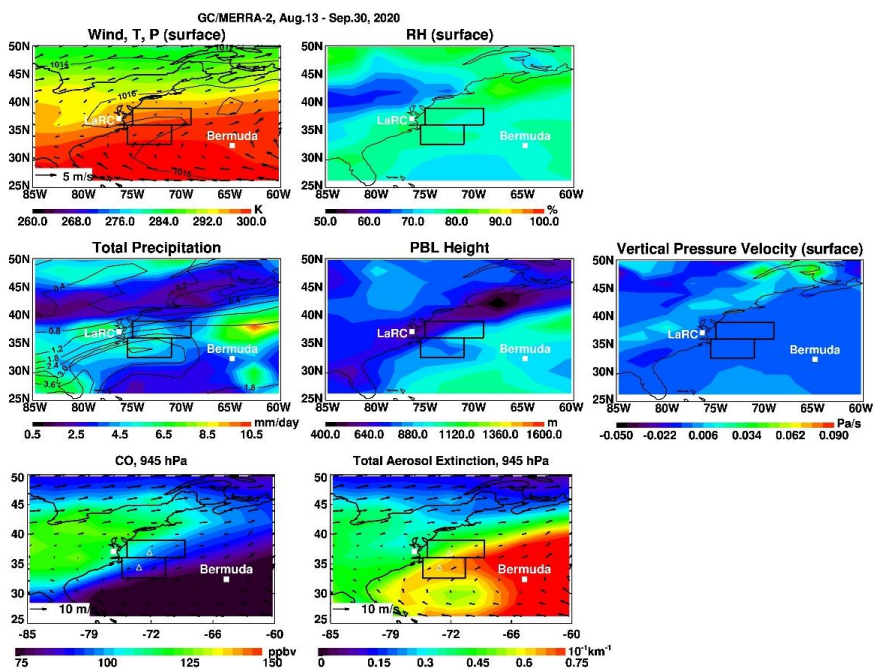


Figure 2b. Same as Fig. 2a, but for Aug.-Sep. 2020 (with different colorbars for temperature and total aerosol extinction).

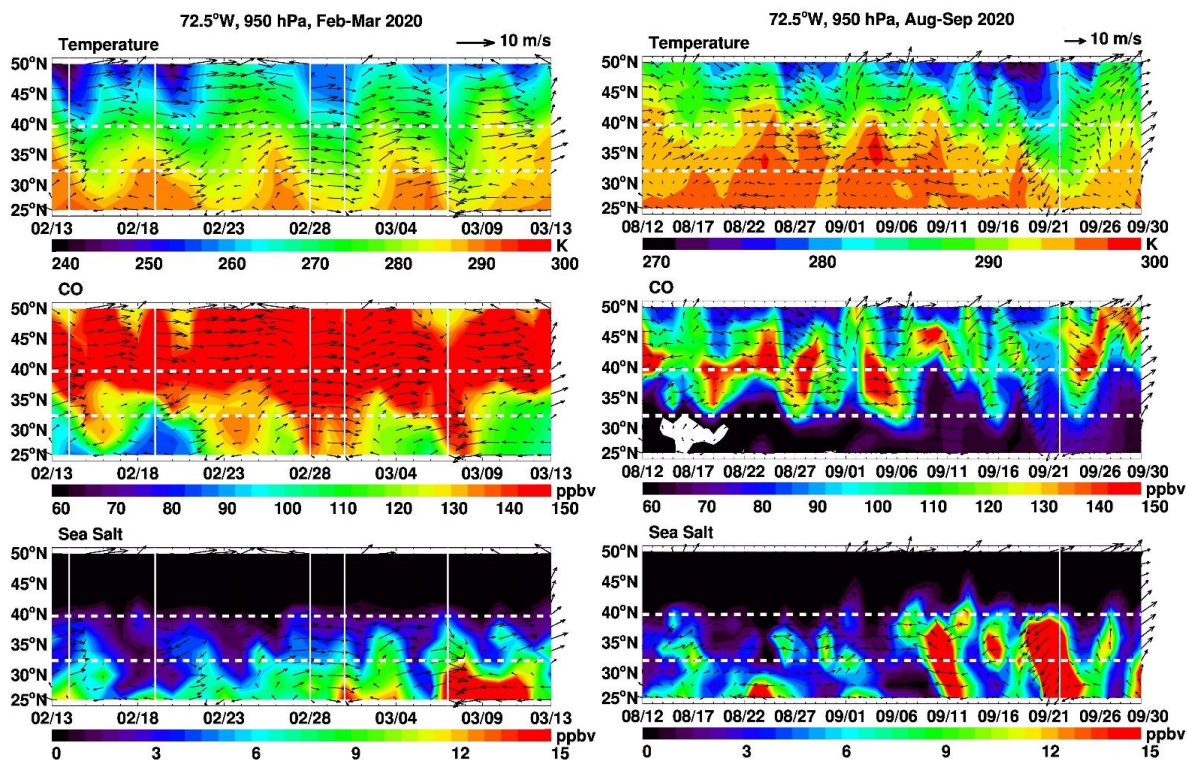
1503
1504



1505

1506

1507



1508

1509 **Figure 3.** Spatiotemporal evolution of boundary-layer outflow to the WNAO. The plots show Hovmöller diagrams of GEOS-Chem

1510 daily mean air temperature (K), horizontal winds (m/s), CO (ppbv), and sea salt mixing ratios (ppbv) at 950 hPa along 72.5°W over

1511 the WNAO during Feb.-Mar. and Aug.-Sep. 2020. Arrows are wind vectors. Two horizontal dotted white lines indicate the latitude

1512 range (32.4-39.8°N) of aircraft measurements. Vertical white lines represent the days of cold front passages as visually identified

1513 by cold air intrusion from north of ~40°N.

1514

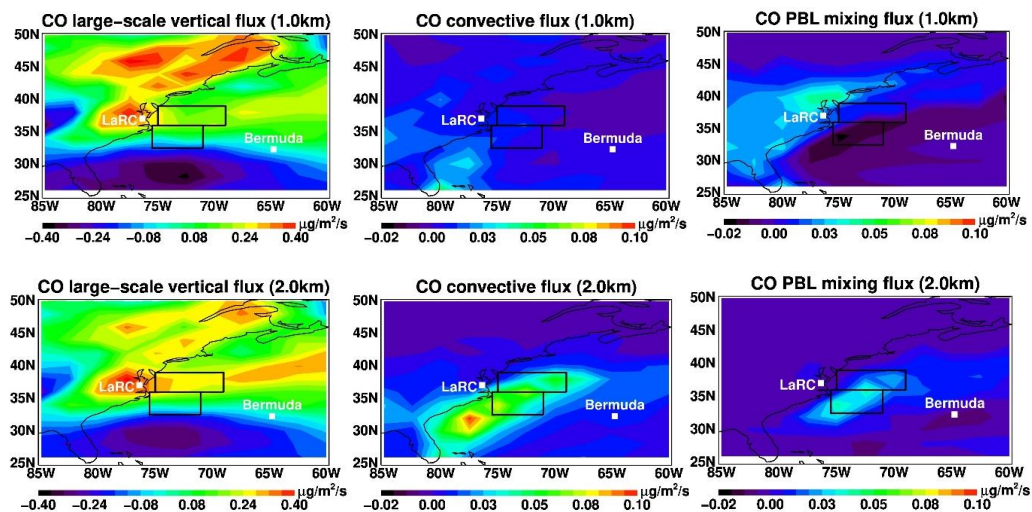
1515



1516

1517

1518



1519

1520

1521

1522

Figure 4a. Model simulated large-scale (resolved) vertical fluxes, convective fluxes, and PBL turbulent mixing fluxes of CO at 1 km (upper row) and 2 km (lower row), averaged over the period of Feb. 14 - Mar. 12, 2020. The two rectangular boxes denote major flight areas (see “N” and “S” in Fig. 1).

1523

1524

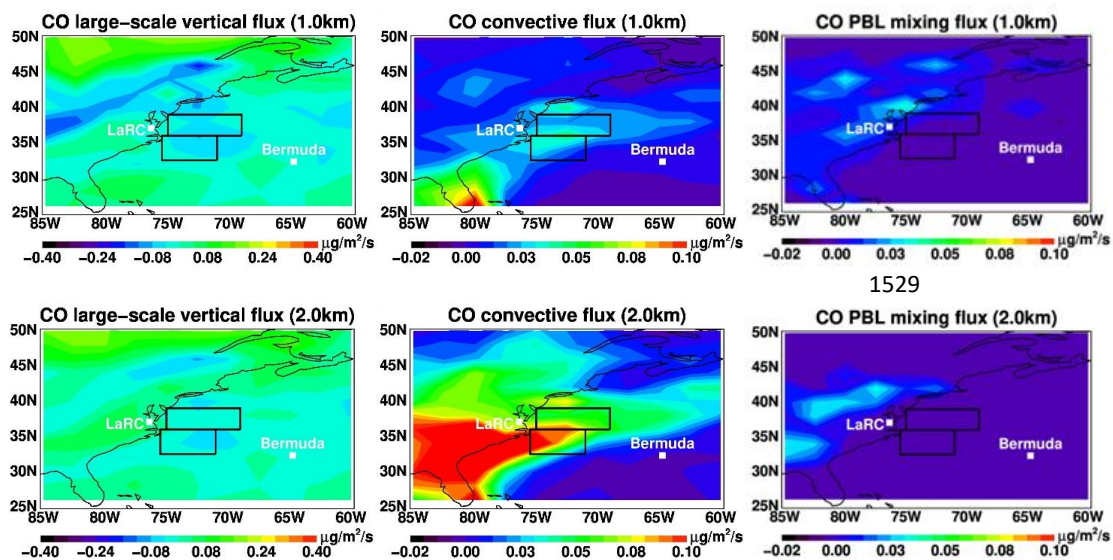


1525

1526

1527

1528



1530

1531 **Figure 4b.** Same as Fig. 4a, but for Aug. 13 - Sep. 30, 2020.

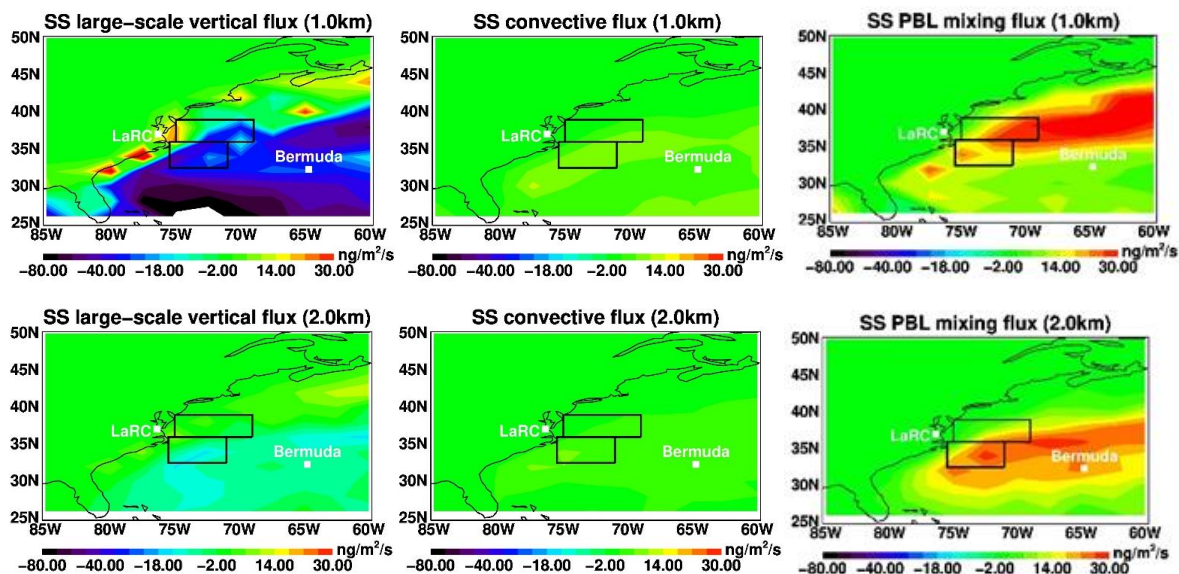
1532

1533



1534

1535



1536

1537 **Figure 4c.** Same as Fig. 4a, but for sea salt during Feb. 14 – Mar. 12, 2020.

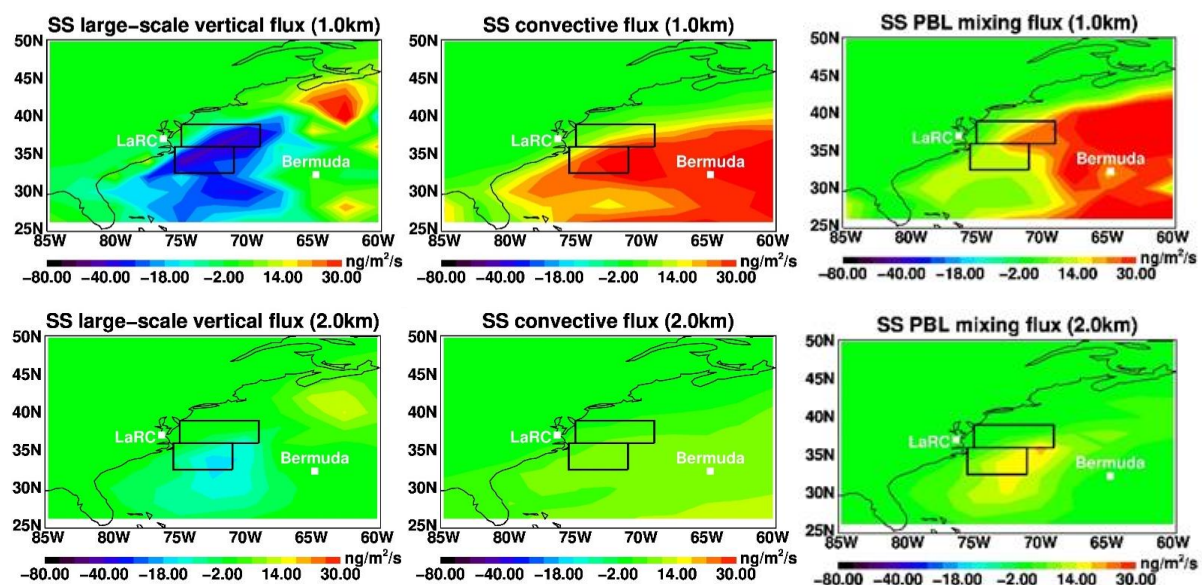
1538



1539

1540

1541



1542

1543 **Figure 4d.** Same as Fig. 4b, but for sea salt during Aug. 13 – Sep. 30, 2020.

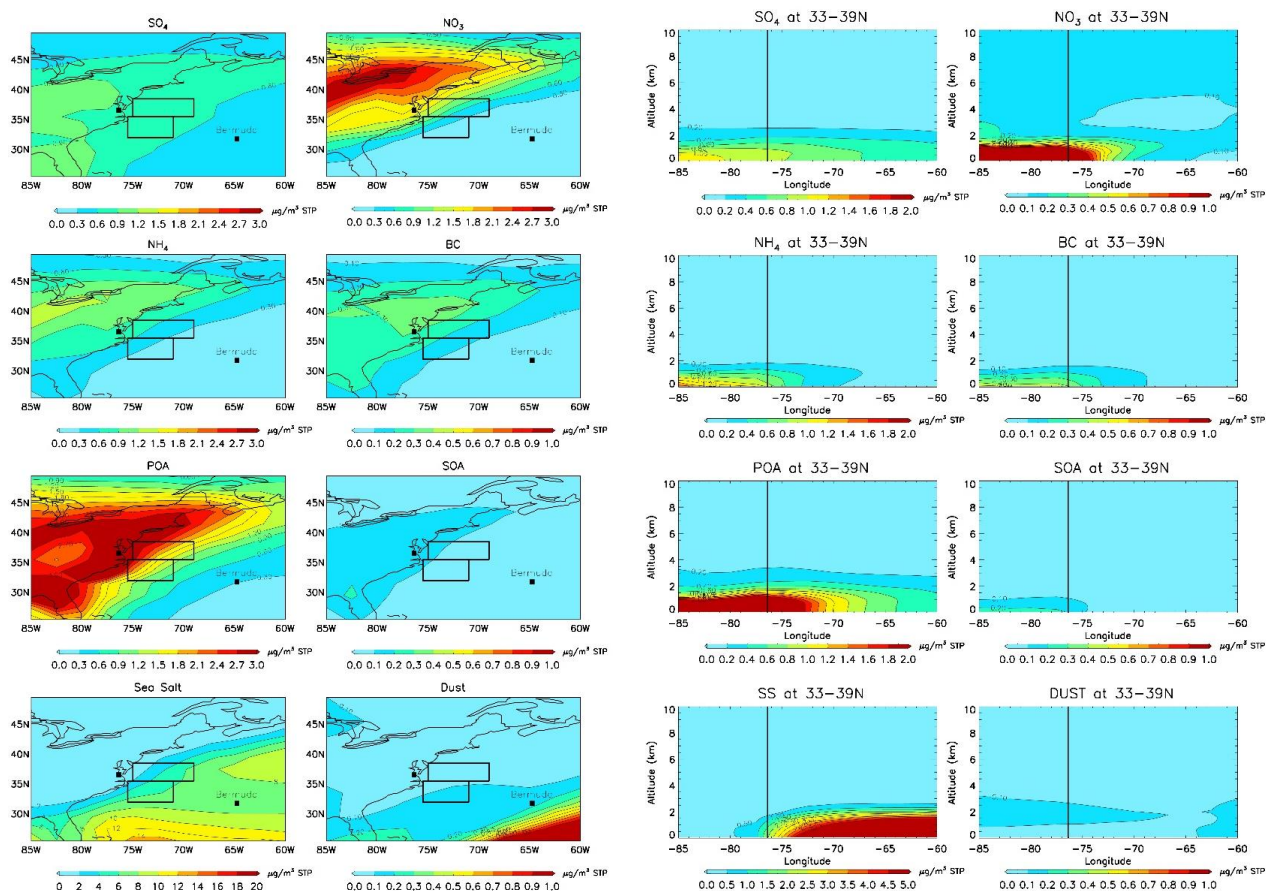
1544



1545

1546

1547



1548

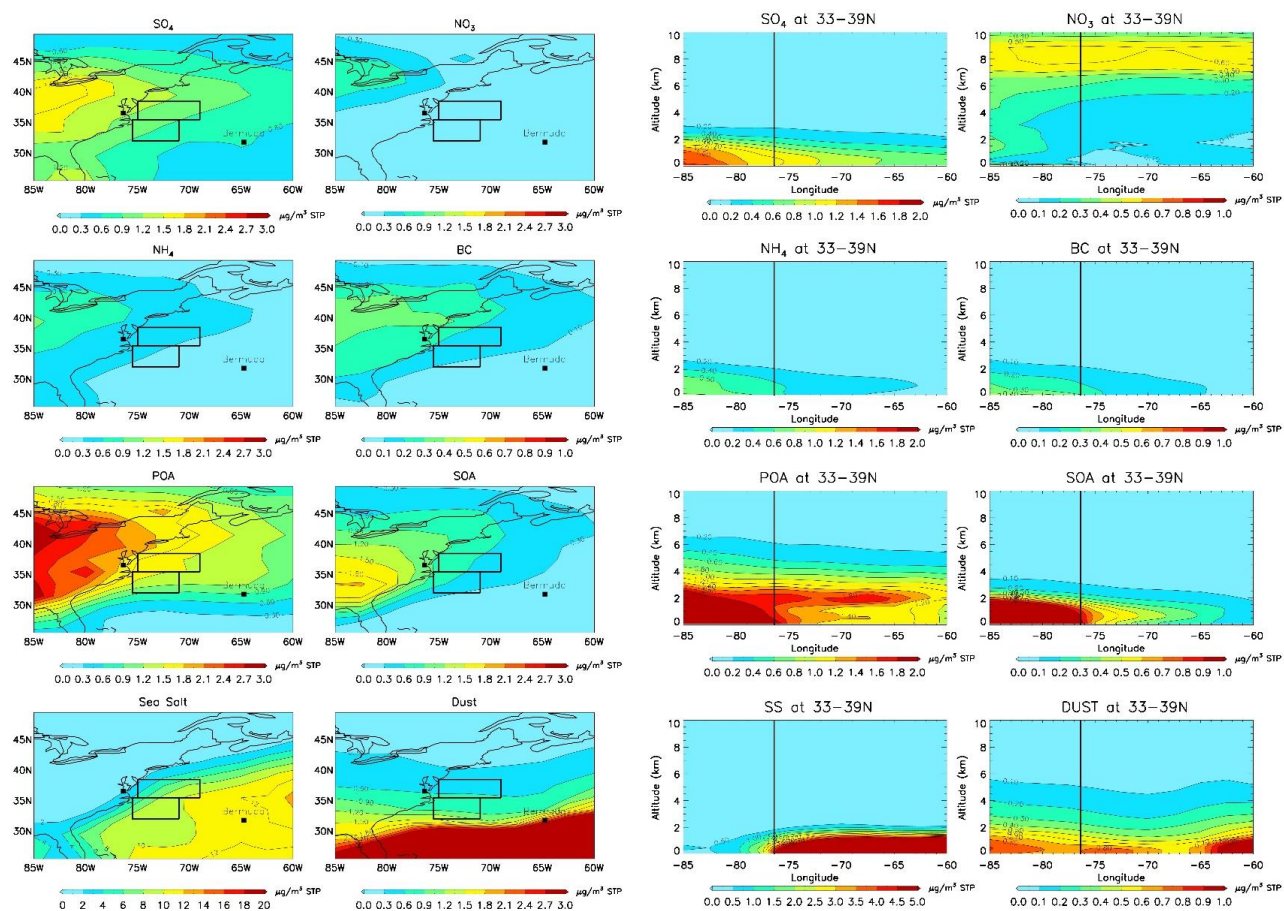
1549 **Figure 5.** Model simulated concentrations of sulfate-nitrate-ammonium (SNA), black carbon (BC), primary organic aerosol (POA),
 1550 secondary organic aerosol (SOA), sea salt, and dust averaged over the period of Feb. 14 - Mar. 12, 2020. Left two columns: map
 1551 plots at 929 hPa; Right two columns: longitude-altitude cross-sections averaged over 33-39°N. Note different color scales among
 1552 panels. Rectangles are the main areas sampled by aircraft during Feb.-Mar. and Aug.-Sep. 2020. The locations of LaRC and
 1553 Bermuda are marked by black squares. The vertical lines in the right columns indicate the longitude (76.4°W) of LaRC.

1554

1555



1556



1557

1558 **Figure 6.** Same as Figure 5, but for Aug. 13 - Sep. 30, 2020.

1559



1560

1561

1562

1563

1564

1565

1566

1567

1568

1569

1570

1571

1572

1573

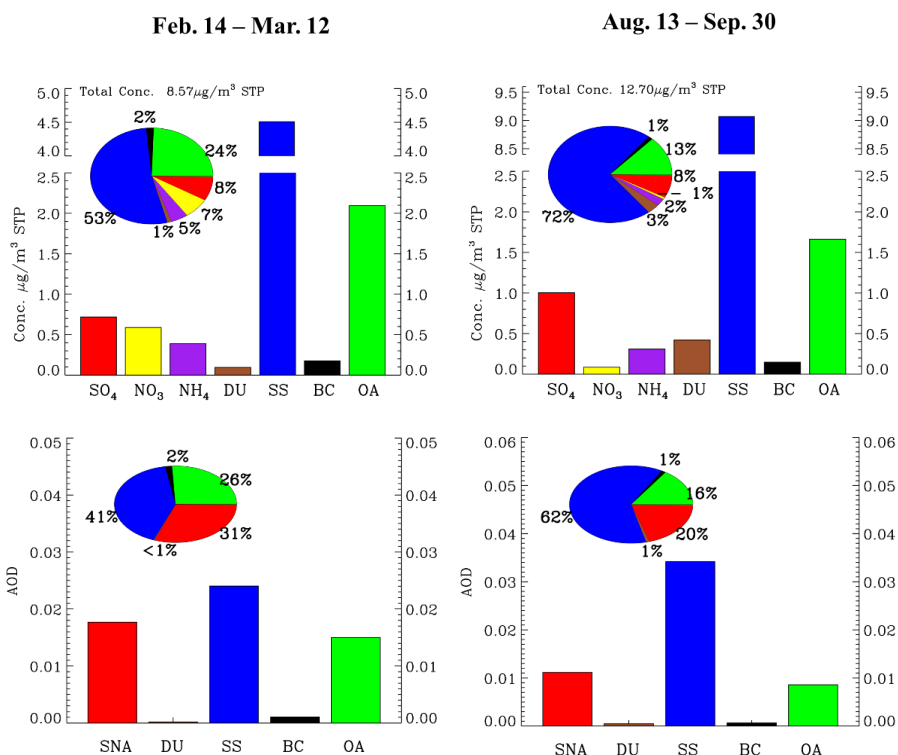
1574

1575

1576

1577

1578



1579 **Figure 7.** Model simulated mass concentrations ($\mu\text{g m}^{-3}$ STP; upper row) and speciated (sulfate, nitrate, ammonium, dust, sea salt,
 1580 black carbon, and organics) AOD in the boundary-layer (lower row) averaged over the flight areas (i.e., “N” and “S” in **Fig. 1**)
 1581 during Feb. 14 - Mar. 12 (left column) and Aug. 13 - Sep. 30 (right column), 2020, respectively. Percentages on the pie chart denote
 1582 the fractions of aerosol species to the total aerosol mass or AOD. Note that the model only calculates a combined AOD for sulfate,
 1583 nitrate, and ammonium (SNA).

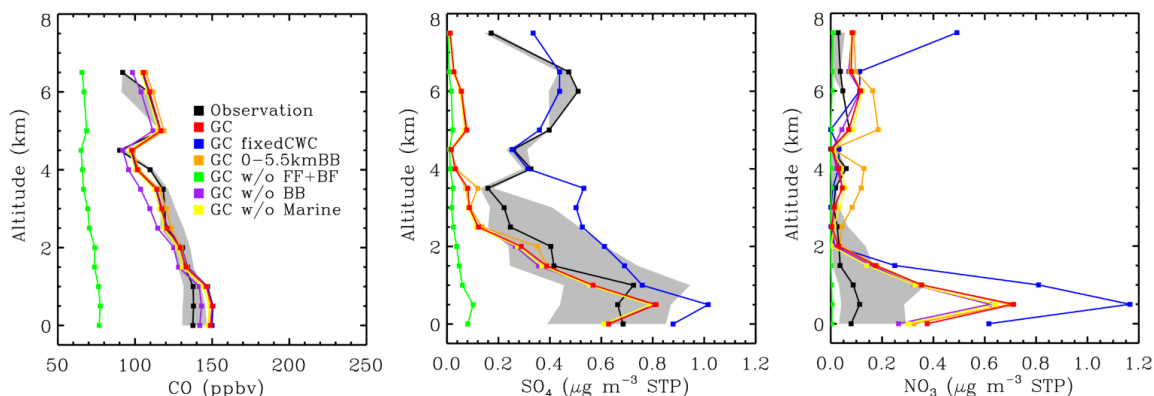
1584

1585



1586

1587



1588

1589

1590

1591

1592

1593

1594

1595

1596

1597

1598

1599

1600

1601

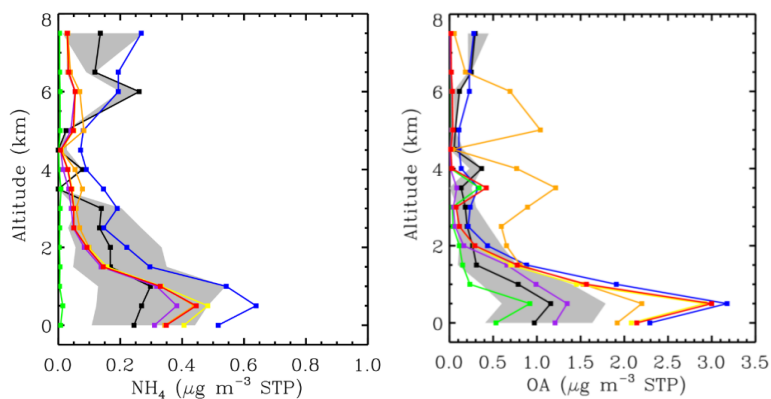
1602

1603

1604

1605

1606



1607

1608

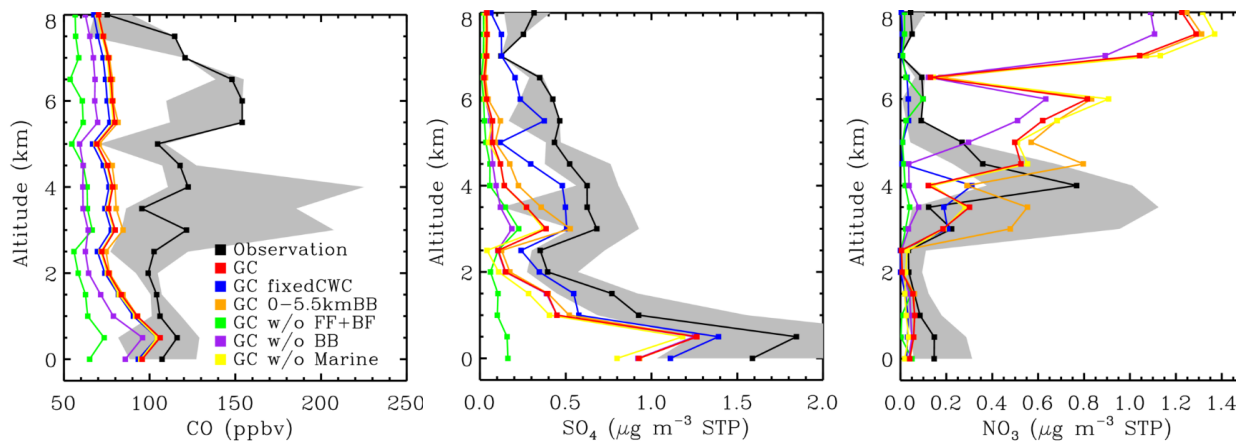
Figure 8. Comparison of model simulated (red) vertical profiles of CO (ppbv), sulfate, nitrate, ammonium, and organic aerosol (OA; $\mu\text{g m}^{-3}$ STP) mixing ratios with Falcon aircraft measurements (black) during Feb.-Mar. 2020. Also shown are model results from simulations (Table 1) with (1) a fixed value for cloud water content used in aerosol scavenging (“fixedCWC”), (2) biomass burning emissions injected to the 0-5.5km altitudes, (3) fossil fuel and biofuel emissions turned off, (4) biomass burning emissions turned off, or (5) marine emissions turned off, respectively. An OA/OC ratio of 2.1 (Philip et al., 2014) is used to convert simulated OC to compare with AMS OA measurements. Hourly model output was sampled at the time and location of aircraft measurements. Values (500m-binned) are medians over all flights. Gray shaded areas indicate the ranges of 25th – 75th percentiles for the observations.



1609

1610

1611



1612

1613

1614

1615

1616

1617

1618

1619

1620

1621

1622

1623

1624

1625

1626

1627

1628

1629

1630

1631

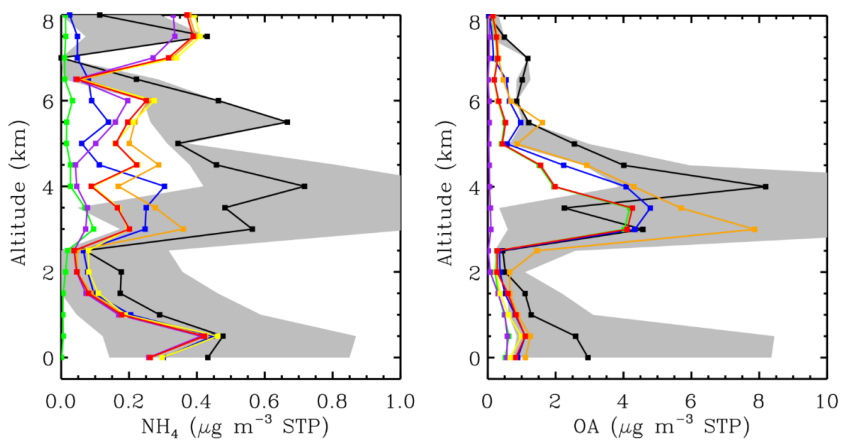


Figure 9. Same as Fig. 8, but for Aug.-Sep. 2020.

1632



1633

1634

1635

1636

1637

1638

1639

1640

1641

1642

1643

1644

1645

1646

1647

1648

1649

1650

1651

1652

1653

1654

1655

1656

1657

1658

1659

1660

1661

1662

1663

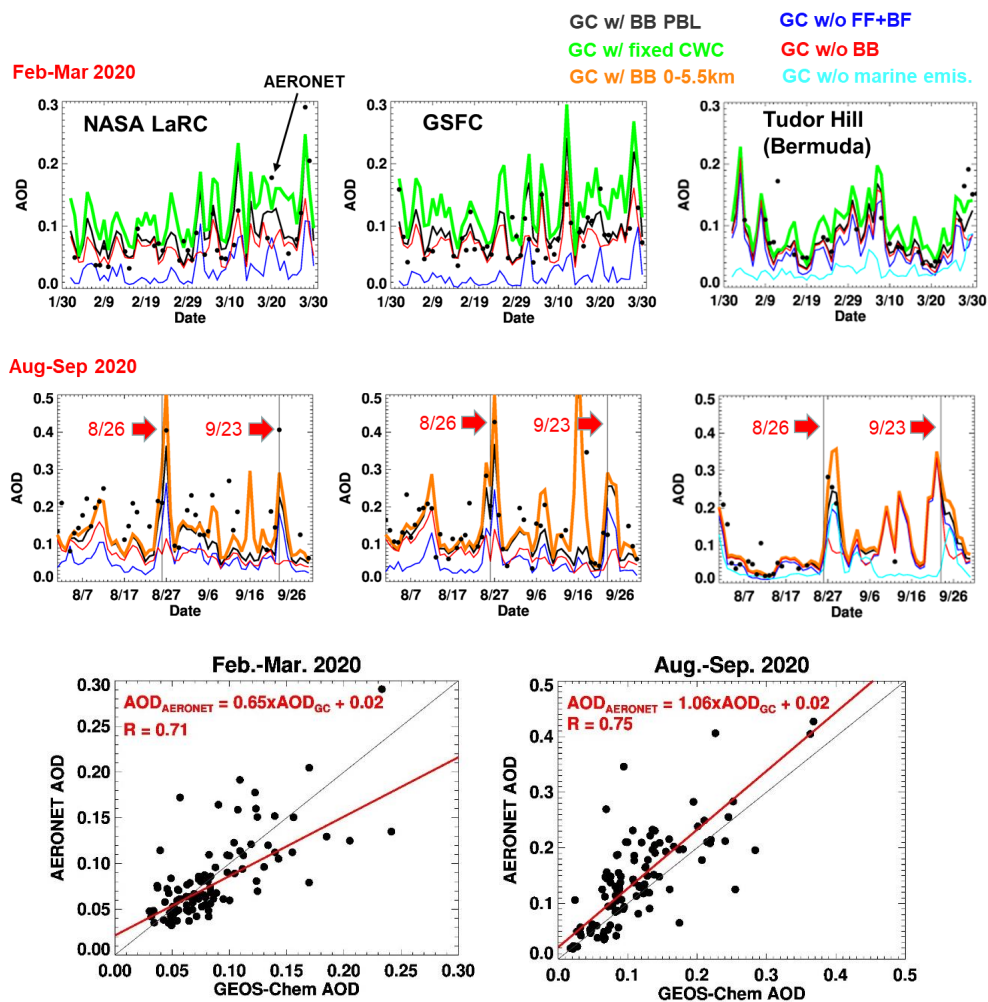


Figure 10. (1) Top and middle rows: Model simulated daily AOD (at 550nm) versus daily AOD measurements from three AERONET sites (NASA LaRC, GSFC, and Tudor Hill) during Feb.-Mar. (top) and Aug.-Sep. (middle) 2020, respectively. Shown for model results are the simulations (Table 1) “standard” (black line), “fixedCWC” (green line), “BB0-5.5km” (orange line), “noanthbf” (blue line), “nobb” (red lines), and “nomari” (cyan lines). (2) Bottom row: Scatterplots of model AODs from the “standard” simulation vs AERONET AODs at the three sites for Feb.-Mar. and Aug.-Sep. 2020, respectively. Red lines are linear regression lines. Grey lines are 1:1 line. Legends show regression line equations and Pearson correlation coefficients (R). For Aug.-Sep. 2020, six very large AERONET AOD values (0.8-1.1), for which the model failed to capture (<0.1), are excluded in the analysis.

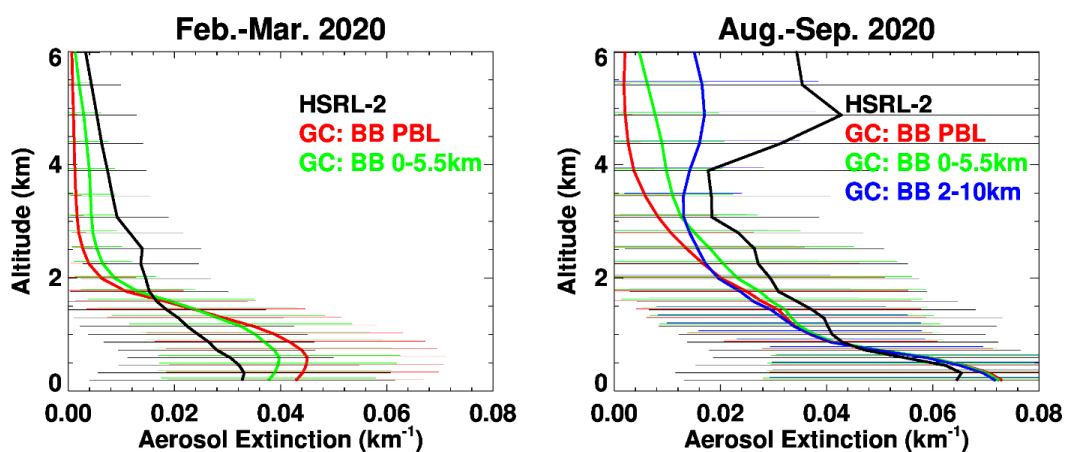


1664

1665

1666

1667



1668

1669

1670

1671

1672

1673

1674

1675

Figure 11. Comparisons of model aerosol extinctions (550nm) with aircraft HSRL-2 lidar measurements (532nm) averaged over all flights during Feb.-Mar. and Aug.-Sep. 2020, respectively. Biomass burning emissions are injected into the planetary boundary layer (“BB PBL”), into the 0-5.5 km altitude interval (“BB0-5.5km”), or into the 2-10 km altitude interval (“BB2-10km”). See Table 1 for the configurations of model simulations. Hourly model output was sampled at the time and location of lidar measurements. Horizontal lines denote +/- standard deviations of observed and simulated aerosol extinctions at model vertical levels.



1676

1677

1678

1679

1680

1681

1682

1683

1684

1685

1686

1687

1688

1689

1690

1691

1692

1693

1694

1695

1696

1697

1698

1699

1700

1701

1702

1703

1704

1705

1706

1707

1708

1709

1710

1711

1712

1713

1714

1715

1716

1717

1718

1719

1720

1721

1722

1723

1724

1725

1726

1727

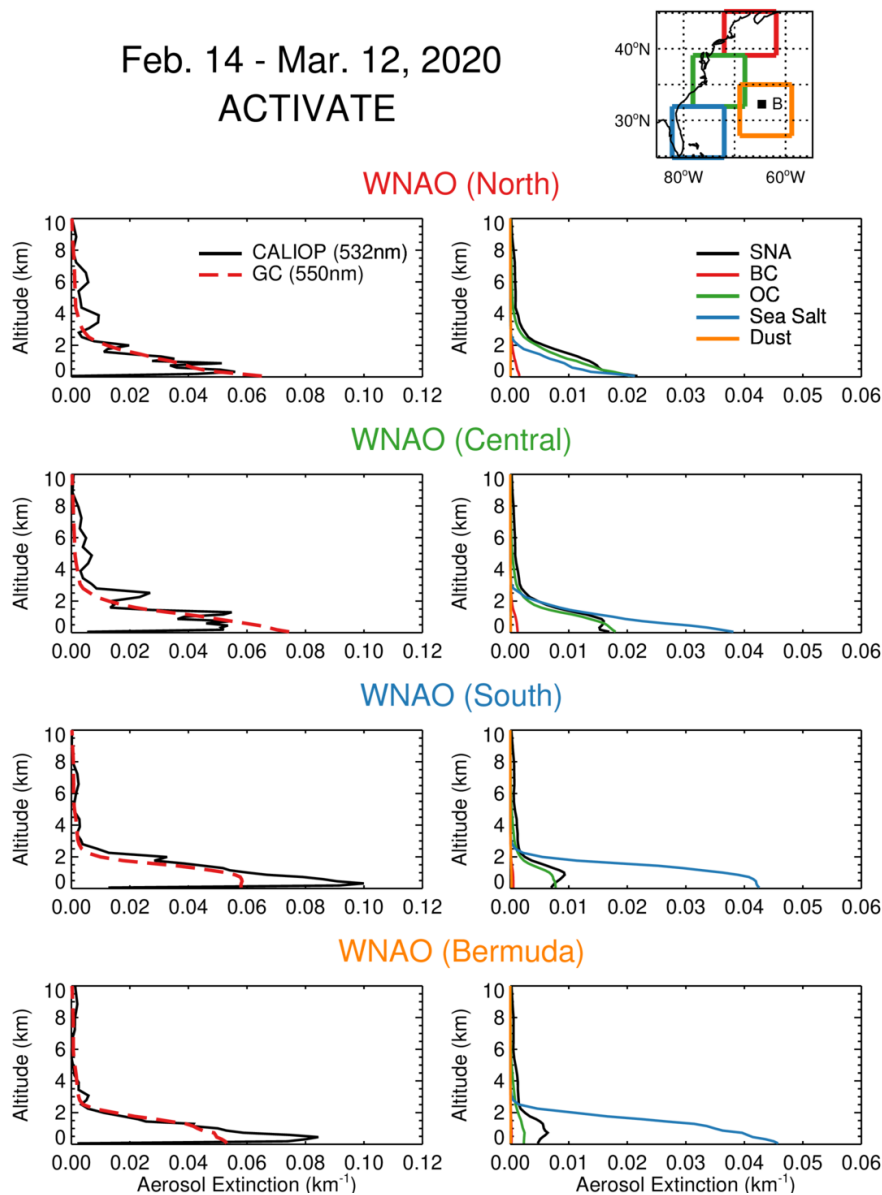


Figure 12a. Left column: Comparison of model results (550 nm) with vertical profiles of CALIOP aerosol extinction (532 nm) averaged over the period of Feb. 14 – Mar. 12, 2020, and for four subdomains of the WNAO, respectively: North (39°–45°N, 72°–62°W), Central (32°–39°N, 78°–68°W), and South (25°–32°N, 82°–72°W), as defined by Corral et al. (2020), and Bermuda (28°–35°N, 69°–59°W). Note that three CALIOP data granules (2020-02-14T06-27-07ZN, 2020-03-03T06-21-54ZN, and 2020-03-04T17-37-24ZD) are excluded from the North WNAO due to cloud contamination. Model results are sampled along the CALIPSO orbit tracks in each box region. Right column: model speciated aerosol extinction profiles corresponding to the total aerosol extinction profile on the left column. SNA = sulfate + nitrate + ammonium.



1728
1729
1730
1731
1732
1733
1734
1735
1736
1737
1738
1739
1740
1741
1742
1743
1744
1745
1746
1747
1748
1749
1750
1751
1752
1753
1754
1755
1756
1757
1758
1759
1760
1761
1762
1763
1764
1765
1766
1767
1768
1769
1770
1771
1772
1773
1774
1775
1776
1777
1778
1779

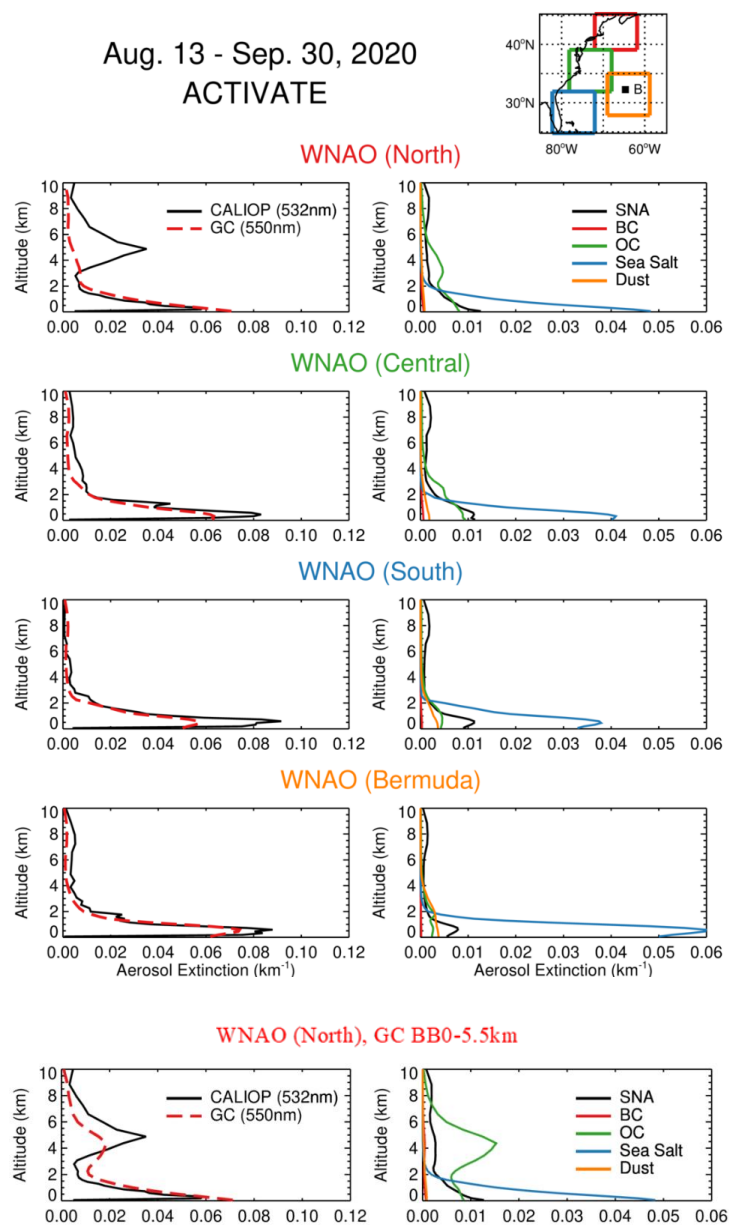


Figure 12b. Same as Fig. 12a, but for the period of Aug. 13 – Sep. 30, 2020. Also shown in the bottom two panels are the results for the North WNAO box region when biomass burning emissions are injected to the 0-5.5 km altitude interval (“BB0-5.5km”, Table 1).



1780
1781
1782
1783
1784
1785
1786
1787
1788
1789
1790
1791
1792
1793
1794
1795
1796
1797
1798
1799
1800
1801
1802
1803
1804
1805
1806
1807
1808
1809
1810
1811
1812
1813
1814
1815
1816
1817
1818
1819
1820
1821
1822
1823
1824
1825
1826
1827
1828
1829

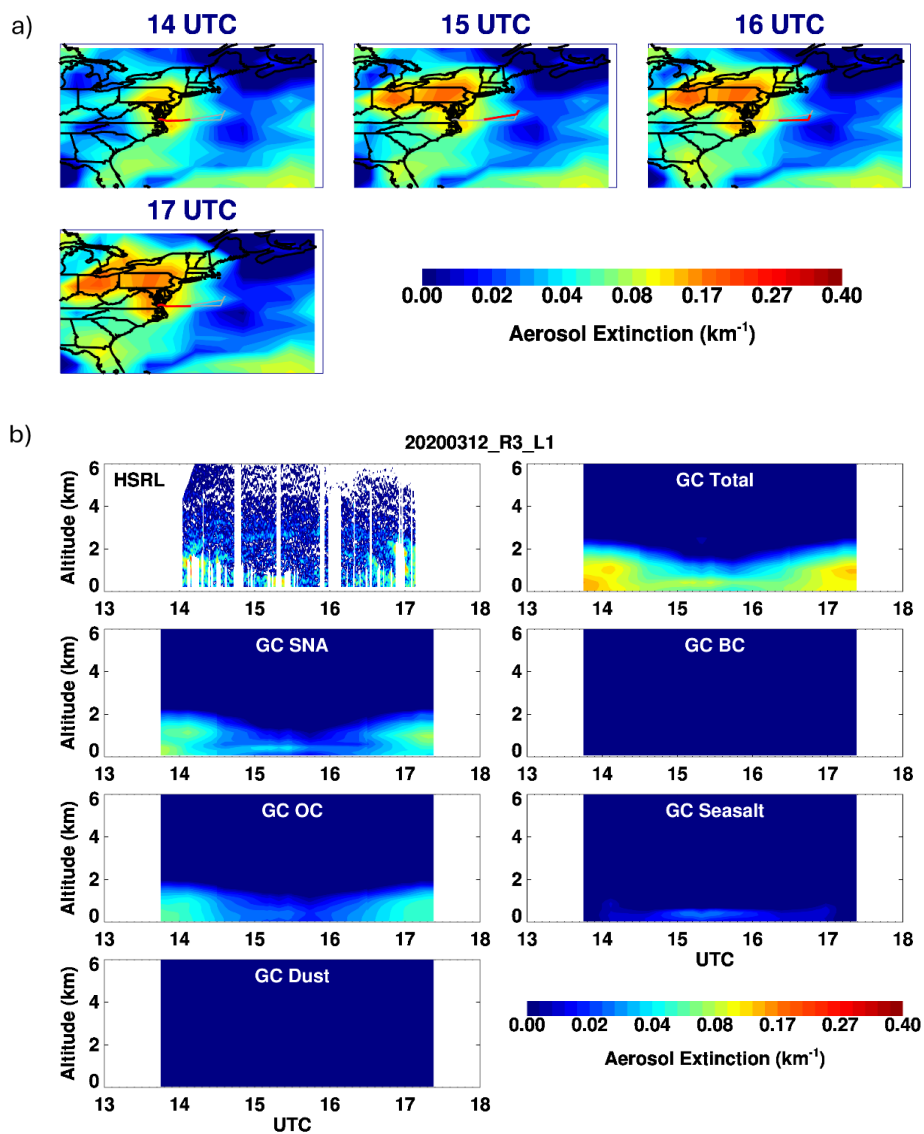


Figure 13. (a) Model simulated hourly total aerosol extinctions at ~1 km altitude over the WNAO during the King Air morning flight (14-17UTC) on March 12, 2020. Gray lines indicate the complete flight track with overlaid red lines denoting the flight tracks for each hour. (b) Time-height cross-section of aerosol extinctions observed by aircraft HSRL-2 lidar (532 nm) compared to that of model aerosol extinctions (550 nm) during the morning flight on Mar. 12, 2020. Curtain plots of model speciated aerosol extinctions along the flight track are also shown. SNA = sulfate + nitrate + ammonium.



1830
1831
1832
1833
1834
1835
1836
1837
1838
1839
1840
1841
1842
1843
1844
1845
1846
1847
1848
1849
1850
1851
1852
1853
1854
1855
1856
1857
1858
1859
1860
1861
1862
1863
1864
1865
1866
1867
1868
1869
1870
1871
1872

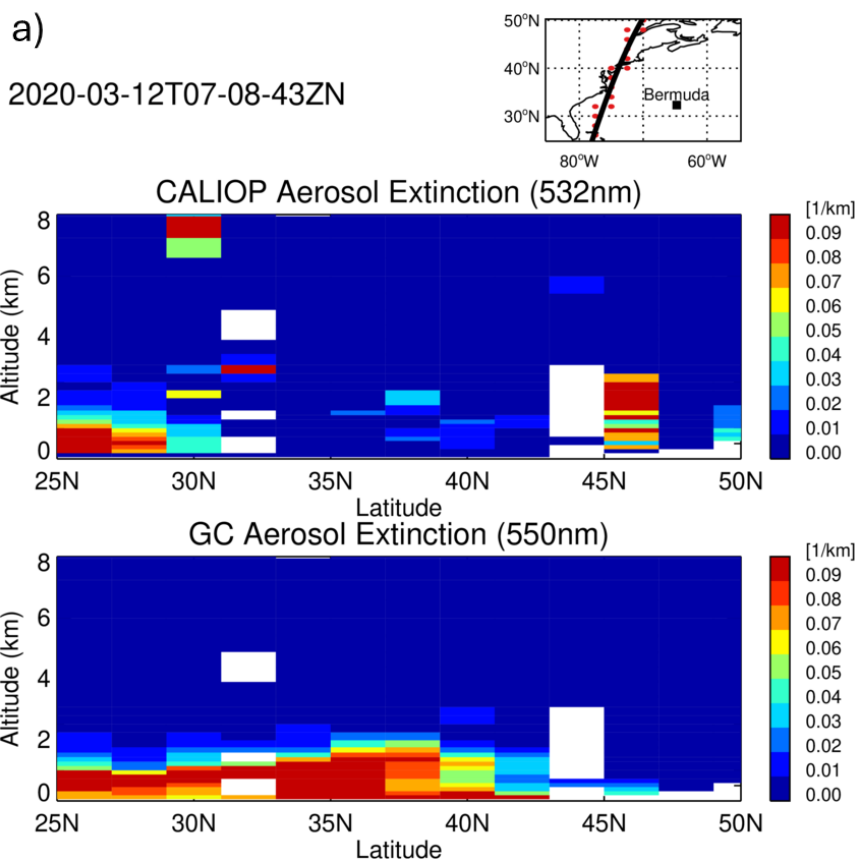
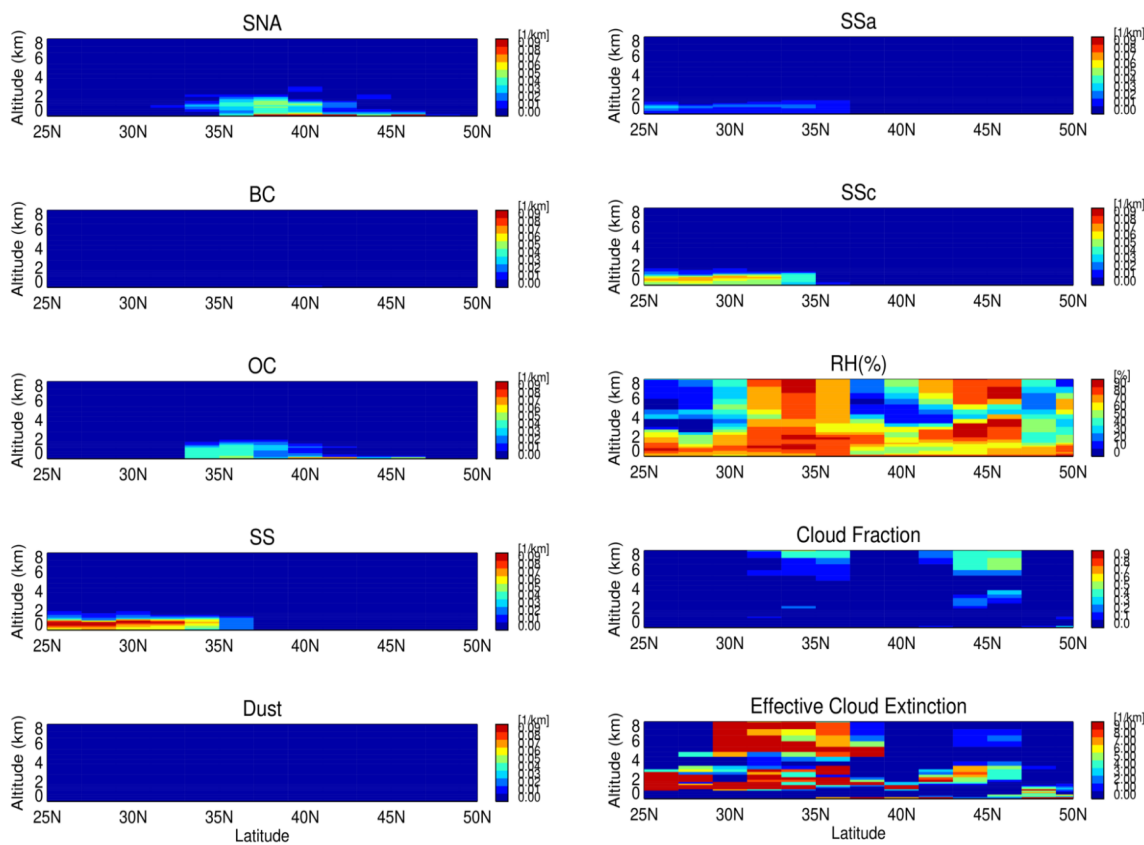


Figure 14. (a) Latitude-height cross-section of aerosol extinctions measured by CALIOP (532 nm) compared to that of model aerosol extinctions (550 nm) over the WNAO at 7:08UTC, Mar. 12, 2020. Model output is sampled at 1:30am LT. (b) Left column: Latitude-height cross-section of speciated aerosol extinctions (550 nm) over the WNAO along the CALIPSO orbit track at 7:08 UTC, Mar. 12, 2020, as simulated by the model. Model output is sampled at 1:30 am LT. Right column: same as left column, but for accumulated sea salt (SSa), coarse-mode sea salt (SSc), MERRA-2 RH(%), MERRA-2 cloud fraction, and MERRA-2 effective cloud extinction.



1873
1874
1875
1876
1877
1878
1879

b)



1880
1881
1882

Figure 14. (cont'd)



1883

1884

1885

1886

1887

1888

1889

1890

1891

1892

1893

1894

1895

1896

1897

1898

1899

1900

1901

1902

1903

1904

1905

1906

1907

1908

1909

1910

1911

1912

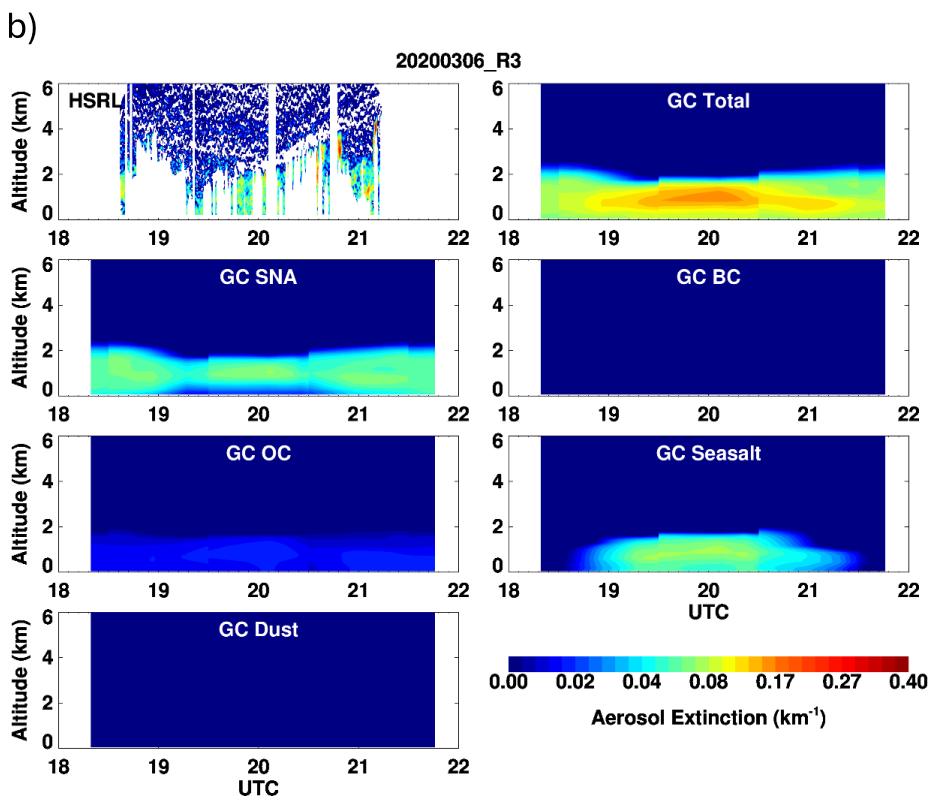
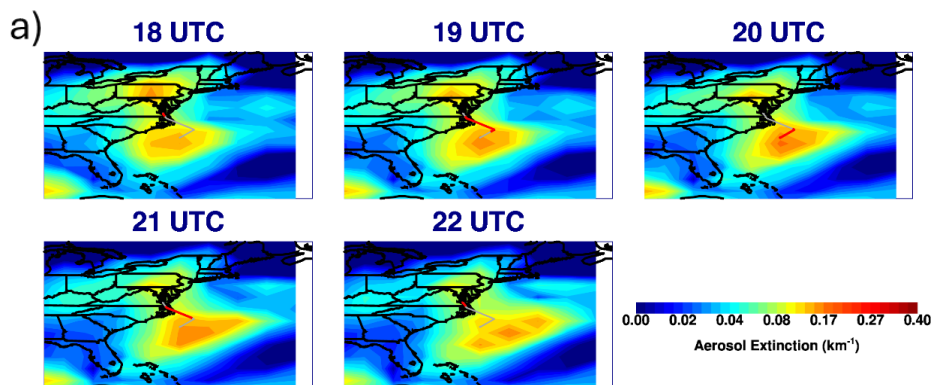


Figure 15. Same as Fig. 14ab but for the flight of Mar. 6, 2020.



1913
1914
1915
1916
1917
1918
1919
1920
1921
1922
1923
1924
1925
1926
1927
1928
1929
1930
1931
1932
1933
1934
1935
1936
1937
1938
1939
1940
1941
1942
1943
1944
1945
1946
1947
1948
1949
1950
1951
1952
1953
1954
1955
1956

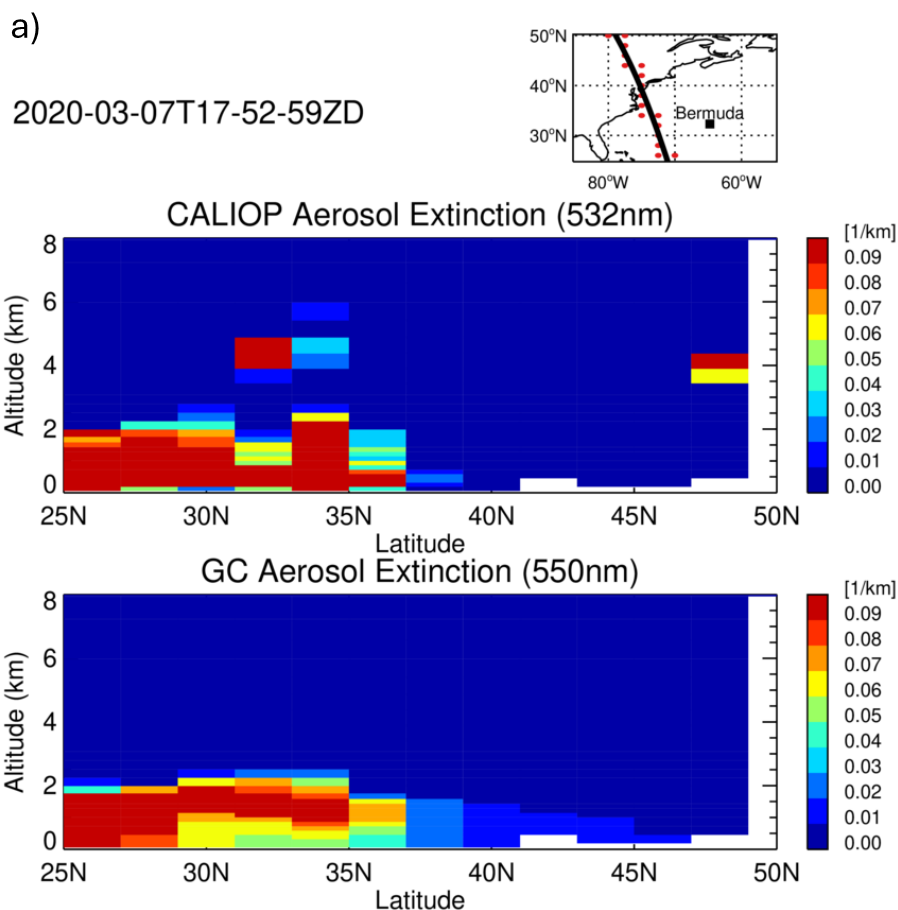
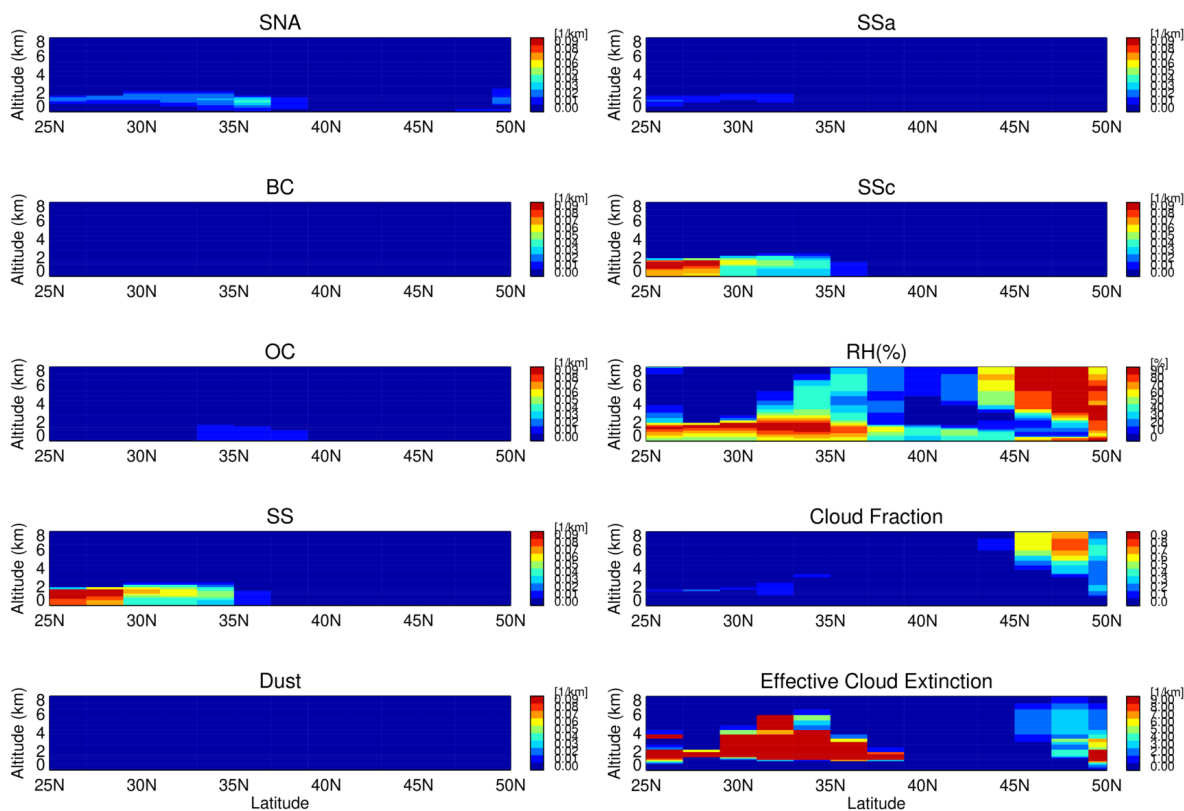


Figure 16. (a) Latitude-height cross-section of aerosol extinctions measured by CALIOP (532 nm) compared to that of model aerosol extinctions (550 nm) over the WNAO at 17:53 UTC, Mar. 7, 2020. Model output is sampled at 1:30 pm LT. (b) Left column: Latitude-height cross-section of speciated aerosol extinctions (550 nm) over the WNAO along the CALIPSO orbit track at 17:53 UTC, Mar. 7, 2020, as simulated by the model. Model output is sampled at 1:30 pm LT. Right column: same as left column, but for accumulated sea salt (SSa), coarse-mode sea salt (SSc), RH, cloud fraction, and effective cloud extinction.



1957
1958
1959
1960
1961
1962

b)



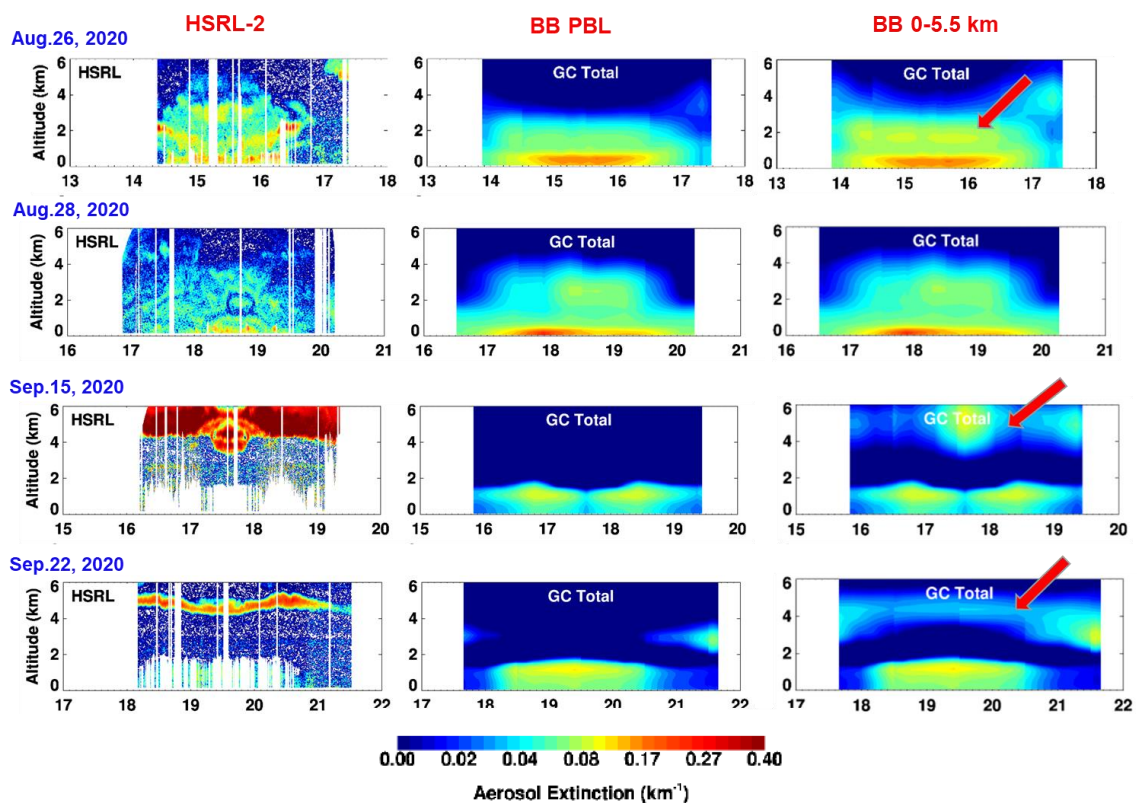
1963 **Figure 16.** (cont'd)
1964



1965

1966

1967



1968

1969

1970

1971

1972

1973

1974

1975

1976

1977

1978

Figure 17. Selected cases where using 0-5.5 km fire emission injection heights improves the model simulations of HSRL-2 aerosol extinction curtains during Aug.-Sep. 2020. The plots compare time-height cross-sections of aircraft HSRL-2 lidar aerosol extinctions (532nm, left column) with those of model aerosol extinctions (550nm, middle and right columns) for the flights of Aug. 26, Aug. 28, Sep. 15, Sep. 22, 2020, respectively. Biomass burning emissions are injected into the planetary boundary layer (“BB PBL”, middle column) or into the 0-5.5km altitude interval (“BB 0-5.5km”, right column). See Table 1 for details on model simulations. Hourly model output was sampled at the time and location of lidar measurements.



1979
1980
1981
1982
1983
1984
1985
1986
1987
1988
1989
1990
1991
1992
1993
1994
1995
1996
1997
1998
1999
2000
2001
2002
2003
2004
2005
2006
2007
2008
2009
2010
2011
2012
2013
2014
2015
2016
2017
2018
2019
2020
2021
2022
2023
2024

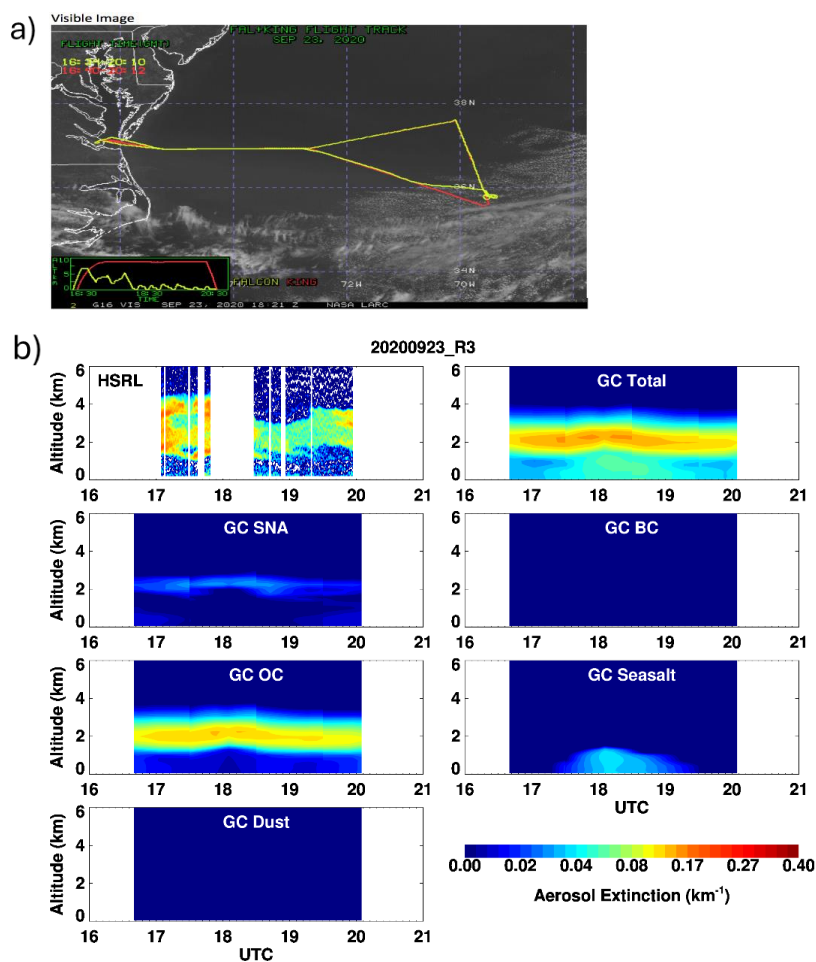
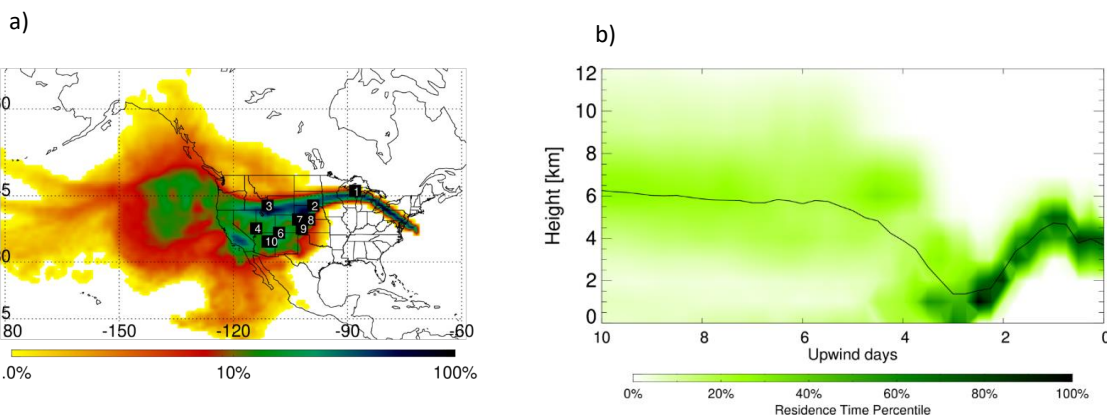


Figure 18. Case study for long-range transport of the western U.S. fire smoke to the WNAO on Sep. 23, 2020. (a) GOES-16 Quicklook Visible Images for 18:21 UTC, Sep. 23, 2020 (NASA Langley SATCORPS group). Superimposed are the King Air (red) and Falcon (yellow) flight tracks. (b) Time-height cross-section of aerosol extinctions observed by King Air HSRL-2 lidar (532 nm) compared to that of model aerosol extinctions (550 nm) for the flight of Sep. 23, 2020. There were no HSRL-2 measurements between 17:48-18:28UTC due to instrument issues. Also shown are curtain plots of model speciated aerosol extinctions along the flight track.

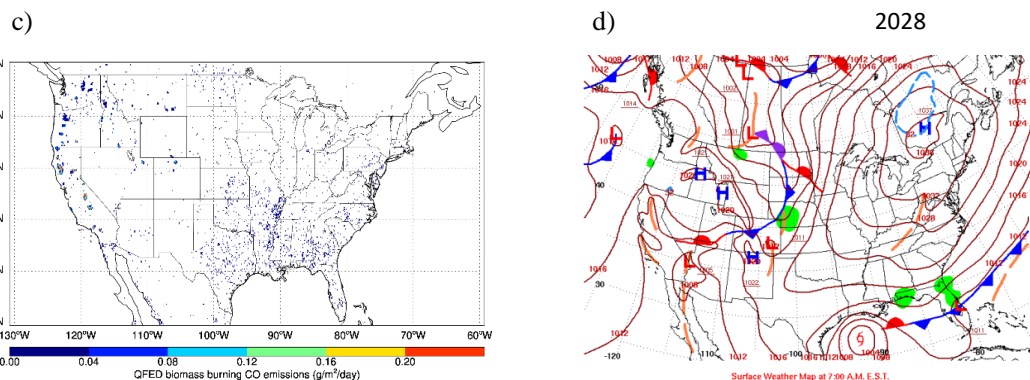


2025

2026



2027



2029

Figure 19. FLEXPART-simulated upwind air parcel residence time for the western U.S. fire smoke observed by HSRL-2 lidar over the WNAO at 17:13UTC, on Sep. 23, 2020. Panel (a) shows the column-integrated air parcel residence time during the entire simulated transport time (20 days). The white labels indicate the approximate locations of the center of the plumes on each upwind day up to the 10th day. Air parcels may pass the same location multiple times during transport and leave high density of residence time at those places. For better case-by-case comparison, residence time is color-coded by logarithmic grades representing its ratio to the location of maximal integrated residence time (100 %) during the transport. Panel (b) shows the vertical distribution of the residence time at given upwind times. The black line indicates the average height of air parcels during transport. (c) Monthly mean QFED biomass burning CO emissions for Sep. 2020. (d) Surface weather map at 7 am EST, Sep. 20, 2020 (https://www.wpc.ncep.noaa.gov/dailywxmap/index_20200920.html).

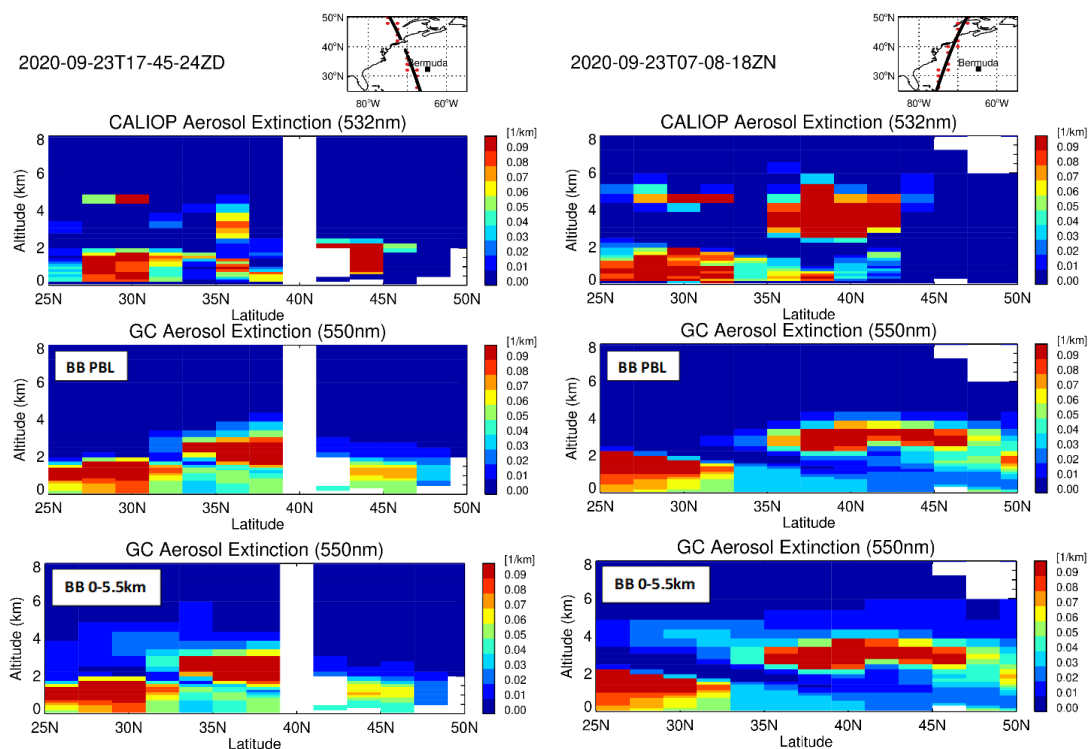
2039

2040



2041

2042



2043

2044 **Figure 20.** Case study for the long-range transport of western U.S. fire smoke to the WNAO during Aug.-Sep. 2020. Latitude-
 2045 height cross-section of aerosol extinctions measured by CALIOP (532 nm, top panel) compared to that of model aerosol extinctions
 2046 (550 nm, middle and bottom panels) over the WNAO at 17:45 UTC (13:45 LT, left column) and 7:08 UTC (3:08 LT, right column),
 2047 Sep. 23, 2020. Model output is sampled at 1:30 pm and 1:30 am LT, respectively. Biomass burning emissions are injected into the
 2048 planetary boundary layer (“BB PBL”, middle panel) or into the 0-5.5 km altitude interval (“BB 0-5.5km”, bottom panel). See Table
 2049 1 for details on model simulations. The top right map shows the corresponding model grid-points (red dots) along the CALIPSO
 2050 orbit track.

2051

2052



2053
2054
2055
2056
2057
2058
2059
2060
2061
2062
2063
2064
2065
2066
2067
2068
2069
2070
2071
2072
2073
2074
2075
2076
2077
2078
2079
2080
2081
2082
2083
2084
2085
2086
2087
2088
2089
2090
2091
2092
2093
2094
2095
2096
2097
2098
2099
2100
2101
2102
2103

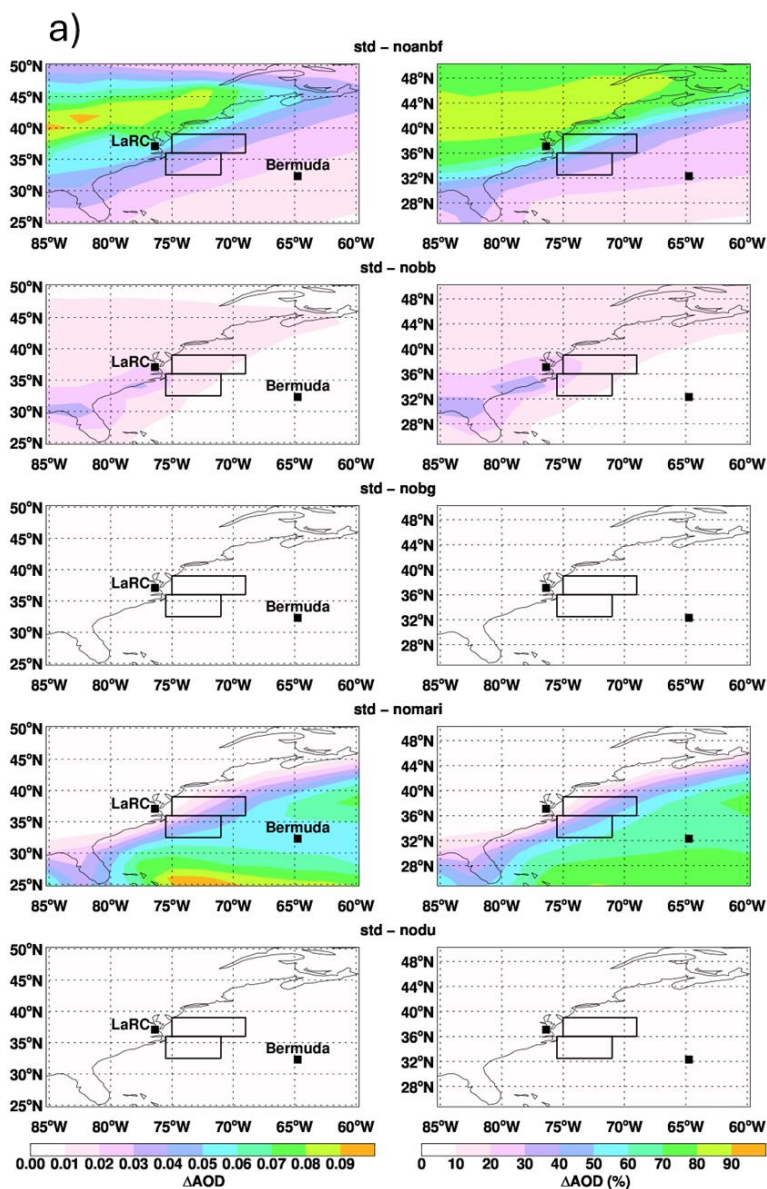


Figure 21. (a) Absolute changes (left column) and percentage changes (right column) in average AODs for the period of Feb.-Mar. 2020 when anthropogenic/biofuel emissions, biomass burning emissions, biogenic emissions, marine emissions, and dust emissions are respectively turned off in the model. The locations of LaRC and Bermuda are marked. (b) same as (a), but for the period of Aug.-Sep. 2020. The two rectangular boxes denote major flight areas (see “N” and “S” in Fig. 1) of Feb.-Mar. and Aug.-Sep. 2020.



2104
2105
2106
2107
2108
2109
2110
2111
2112
2113
2114
2115
2116
2117
2118
2119
2120
2121
2122
2123
2124
2125
2126
2127
2128
2129
2130
2131
2132
2133
2134
2135
2136
2137
2138
2139
2140
2141
2142
2143
2144
2145
2146
2147
2148
2149
2150
2151
2152

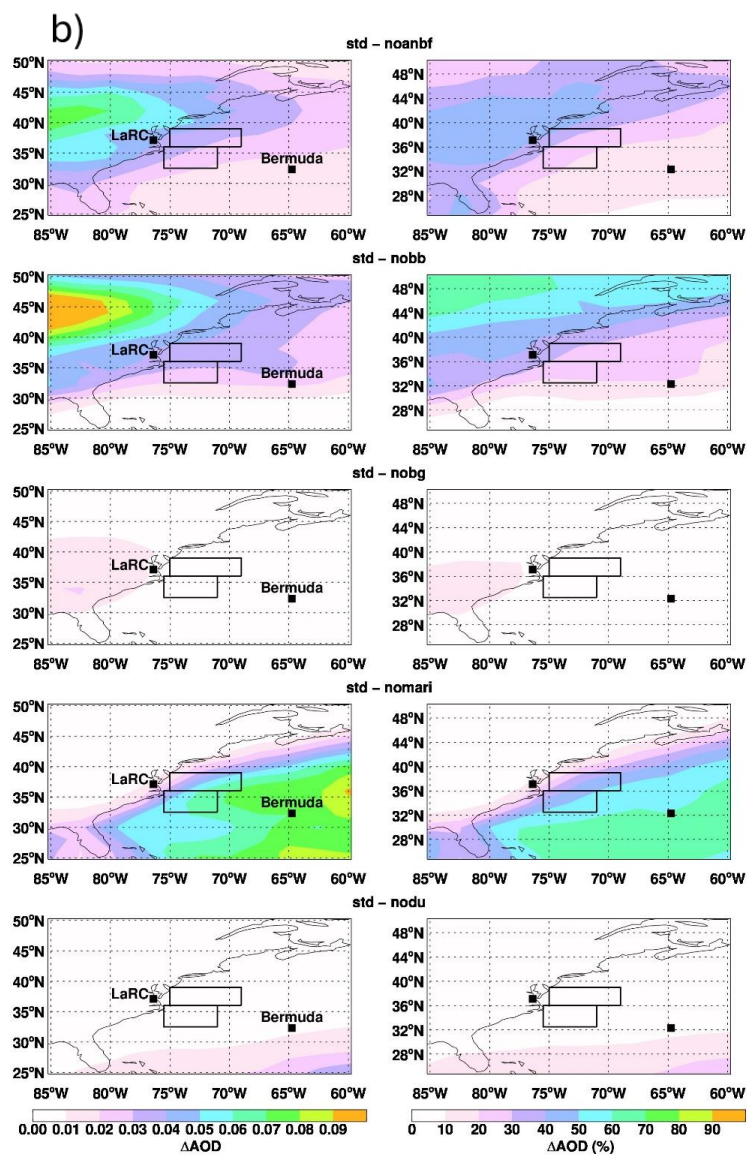


Figure 21. (cont'd)